Journal of Advanced Materials and Processing

Islamic Azad University - Najafabad Branch

Journal of Advanced Materials and Processing

Vol.10, No.2, Spring 2022.

ISSN: 2322-388X

E-ISSN: 2345-4601

Publisher: Najafabad Branch, Islamic Azad University, Iron and Steel Association of Iran

Production manager: Mohsen Ghasemi

Executive assistant: Leily Rezaei, Seyedeh Razieh Anvari

Address: Journal of Advanced Materials and Processing

Department of Materials Engineering, Najafabad Branch, Islamic Azad University, Najafabad, Isfahan, Iran

P.O. Box: 517

Tel:+98-31-42292512 **Fax:**+98-31-42291008

Website: www.jmatpro.iaun.iau.ir

Email:jmatpro@iaun.ac.ir

Table of Content

JMATPRO	Journal of Advanced Materials and Processing 10 (2): 3-10, Spring 2022 http://jmatpro.iaun.iau.ir 20.1001.1.2322388.2022.10.2.1.6

Research Paper

Investigation of Microstructure and Mechanical Properties of Ni-Cu-P Coatings Deposited by the Electroless Method

Danial Davoodi[1], Amir Hossein Emami[1,*], Sayed Mahmoud Monir Vaghefi[2], Mahdi Omidi[1], Hamid Reza Bakhsheshi-Rad[1]

1. Advanced Materials Research Center, Department of Materials Engineering, Najafabad Branch, Islamic Azad University, Najafabad, Iran.
2. Department of Materials Engineering, Isfahan University of Technology, Isfahan 84156-83111, Iran.

ARTICLE INFO

Article history:

Received 21 February 2022
Accepted 30 March 2022
Available online 1 April 2022

Keywords:
Electroless Ni-Cu-P
Microhardness
L80 steel
TEM
Heat treatment

ABSTRACT

In the current study, the effect of colloidal copper nanoparticles on the deposition rate and hardness of Ni-Cu-P coating deposited by electroless method on L80 steel substrate was investigated. Copper particle size, microstructure, chemical composition, and hardness of the coating before and after heat treatment at different temperatures were examined by transmission electron microscopy (TEM), X-ray diffraction (XRD), scanning electron microscopy (SEM) equipped with energy dispersive X-ray (EDS) analysis, and microhardness. The microstructure study by XRD showed that the Ni-Cu-P coating has an amorphous structure. The heat treatment at 400 °C transformed the structure from amorphous to crystalline and formed Ni_{α}, Ni_3P, and $Ni_{3.8}Cu$ phases. The amount of copper nanoparticles in the coating 4.58 wt% was measured. The deposition rate of the Ni-Cu-P coating was 11 µm/h. Furthermore, the hardness of the coating increased from 738HV to 1300HV by performing heat treatment.

Citation: Davoodi, D.; Emami, A.H.; Monir Vaghefi, S.M.; Omidi, M.; Bakhsheshi-Rad, H.R. (2022). Investigation of Microstructure and Mechanical Properties of Ni-Cu-P Coatings Deposited by the Electroless Method, Journal of Advanced Materials and Processing, 10 (2), 3-10. Dor: 20.1001.1.2322388.2022.10.2.1.6

* **Corresponding Author**
E-mail Address: Dr.s.a.h.emami@gmail.com

1. Introduction

L80 steels, due to the desired mechanical properties and low price, are widely used as casing and tubing of pipes in gas and oil wells according to API5CT standards. However, these steels do not have good corrosion resistance [1–3].

Today electroless Ni-P coatings are widely used to increase the corrosion resistance of ferrous and non-ferrous metals. Excellent corrosion resistance, good wear behavior, and high hardness have led to the increasing use of electroless Ni-P coatings, especially in the oil and gas industry [4–6]. Over the years, researchers have been trying to optimize the properties of coatings parameters such as temperature, pH, concentration, and chemical composition of electroless baths and the rate of deposition. Furthermore, compositing these coatings with metal and ceramic particles upgrades the mechanical and chemical properties of the coatings [7–9].

Recently, studies have been performed on electroless Ni-P coatings composite reinforced with MoS_2, ZrO_2, SiC, Al_2O_3, PTFE, Ti, and Mo [10–15]. Unlike electrical coating methods, electroless coating methods have a lower deposition rate, increasing coating time and costs [2,16]. In electroless baths, different crystallographic structures from amorphous to crystalline states can be obtained by changing the two parameters of temperature and pH. Also, in electroless baths with acidic pH, the deposition rate can be increased to some extent by increasing pH and temperature simultaneously. On the other hand, failure to control these two parameters can lead to the decomposition of the electroless bath. Therefore, by changing the chemical composition and using other chemical factors such as deposition rate accelerators, in addition to increasing the deposition rate, other parameters such as hardness and corrosion resistance are also increased [17].

Tabatabai et al. [18] investigated the effect of different amounts of sodium sulfate (Na_2SO_4) in an electroless acid-coated bath on the deposition rate and corrosion behavior. The results showed that the deposition rate in the bath without Na_2SO_4 was 10 µm/h, while at an optimal concentration of 1 g/LNa_2SO_4, the deposition rate reached 14 µm/h. On the other hand, the corrosion current density decreases from 3.3 µA/m^2 in the bath without Na_2SO_4 to 1.3 µA/m^2 in the bath with 1 g Na_2SO_4, due to the reduction of cavities and defects in the coating and surface passivation. Kundu et al. [19] reported that the addition of tungsten sulfate in Ni-P electrolysis solution significantly increased the hardness due to the formation of a solid solution between W and Ni elements in the electroless Ni-P-W coating before heat treatment and also the transformed of the structure from amorphous to crystalline after heat treatment at 400 °C. However, the effect of colloidal copper nanoparticles on the deposition rate and hardness of Ni-Cu-P coating deposited by electroless method on L80 steel substrate was not investigated so far. Therefore, in the present study, an attempt was made to create a Ni-Cu-P composite coating by adding colloidal copper nanoparticles. Then the effect of these nanoparticles on the deposition rate as well as the microstructure was investigated. The effect of heat treatment at different temperatures on phase transformations and micro-hardness of the coating was also studied.

Table 1. Chemical compositions of the L80 alloy

Fe	C	Mn	Ni	Cu	P	S	Si
Bal.	0.430	1.900	0.250	0.350	0.030	0.030	0.450

2. Materials and method

2.1. Sample preparation

L80 steel Type 1 (according to API5CT standard) was used as a substrate; Table 1 shows the chemical composition of the alloy. Discs with a diameter of 30 mm and a thickness of 10 mm were prepared for coating. To remove the surface roughness and oxide layers of the samples, sandpaper No. 80 to 1500 was used for ground and polishing. To remove grease and organic contaminants, the samples were immersed in a degreasing solution for 20 min. The degreasing solution composition [4] is brought in Table 2. After that, the samples were washed twice with distilled water and then immersed in 20 wt% HCl solution for 60 s to remove oxide layers and activate the surface. Then the samples were rinsed twice with distilled water and immediately dipped in the electroless plating solution.

Table 2. Chemical composition of degreasing

Chemical composition of degreaser	30 g/L sodium hydroxide, 30 g/L sodium carbonate and 30 g/L sodium phosphate
T (℃)	60
pH	11
t (min)	20

2.2. Preparation of electroless solutions

Nickel sulfate and sodium hypophosphite were used as a source of nickel ions along with a reducing agent and a source of phosphorus, respectively, to make Ni-Cu-P, Ni-P electrolysis solutions. To make a solution containing copper nanoparticles, copper colloidal nanoparticles with 60-70 nm particle size was used. Water solvent and SLS surfactant were utilized in colloidal copper solution with a concentration of 4000 ppm copper nanoparticles. Details of the chemical composition of Ni-Cu-P and Ni-P electroless solutions are given in Table 3. All samples were coated at a temperature of 85±3 °C and a constant pH=4.7±0.2.

Table 3. Chemical compositions of the Ni-P and Ni-Cu-P bath

Bath	$NiSO_4 \cdot 6H_2O$	$Na_2PO_2H_2$	$CH_3COONa.3H_2O$	$C_3H_6O_3$	$Pb(C_2H3O_2)_2$	NH_3	Nano colloid Cu
Electroless Ni-P	32 g/L	30 g/L	38 g/L	28 g/L	1 ppm/ L	5 g/L	-
Electroless Ni-Cu-P	32 g/L	30 g/L	38 g/L	28 g/L	1 ppm/L	5 g/L	0.2,0.3, 0.4 g/L

2.3. Heat treatment

In accordance with ASTM B733 standard for this type of substrate, after coating to improve adhesion and hydrogenation, as well as to transform the initial structure to a crystalline structure, after heat treatment at a temperature of 200 °C for 180 min the samples were exposed to 400 °C for 60 min. The heating rate was 20 °C/min [16].

2.4. Microstructural study of coatings

To identify the copper particle size, a Philips transmission electron microscope (TEM model CM120) was used. To study the type and composition of the phase formed in the coating process and also to study the effect of heat treatment of the samples under phase analysis by Philips XRD (model PW30-40) was used. The diffraction pattern was obtained in the range 2θ=10-90° and step size = 0.05. The voltage used in the device was 30 kW and the applied current was 30 mA. All analyzes used Cu-Kα single radiation with a wavelength of 1.5405 Å. X'Pert High Score software was used to identify the phases. To investigate the chemical composition of the coating, a Cam-Scan field emission microscope equipped (FESEM, model MV2300) equipped with energy dispersive X-ray (EDS) analysis was used.

2.5. Micro-hardness of the coating

A micro-hardness tester made by Beuhler company under the load of 25 g was considered. To obtain a more accurate result from each sample, three points from the top of the coating were considered to take the hardness, and the average hardness number was reported on the micro-Vickers scale.

Table 4. Stability of solution in different amounts of copper nanoparticles

Amount of Cu (mg/l)	Stability condition
-	Stable
0.2	Stable
0.3	Stable
0.4	After 10 min decomposition
0.5	Decomposition immediately

3. Results and discussion

Table 4 shows the stability of electroless Ni-Cu-P solution in different amounts of copper nanoparticles at the same temperature and pH. Electroless baths depend highly on parameters such as temperature, pH, and concentration of bath components [10–13]. If these parameters are not optimal and not controlled, the deposition process will not take place, or the solution will decompose due to a lack of control of free metal ions [16]. When the amount of foreign particles such as copper nanoparticles for compositing exceeds an optimal value, the solution decomposes due to excessive formation of free nickel metal ions and lack of control of these ions by complexing agents. It was found that adding more than 300 mg/L of copper nanoparticles to the solution will lead to solution decomposition. Therefore, 300 mg/L of copper nanoparticles was considered the optimal concentration in all electroless Ni-Cu-P coating samples.

Figure 1 shows a TEM micrograph of colloidal copper particles used in the electroless bath. As it is shown, the size of copper particles is in the range of 60-70 nm and confirms that the nanoparticles copper is a colloidal solution. The presence of nanoparticles increases the strength of the coating through the Orowan mechanism.

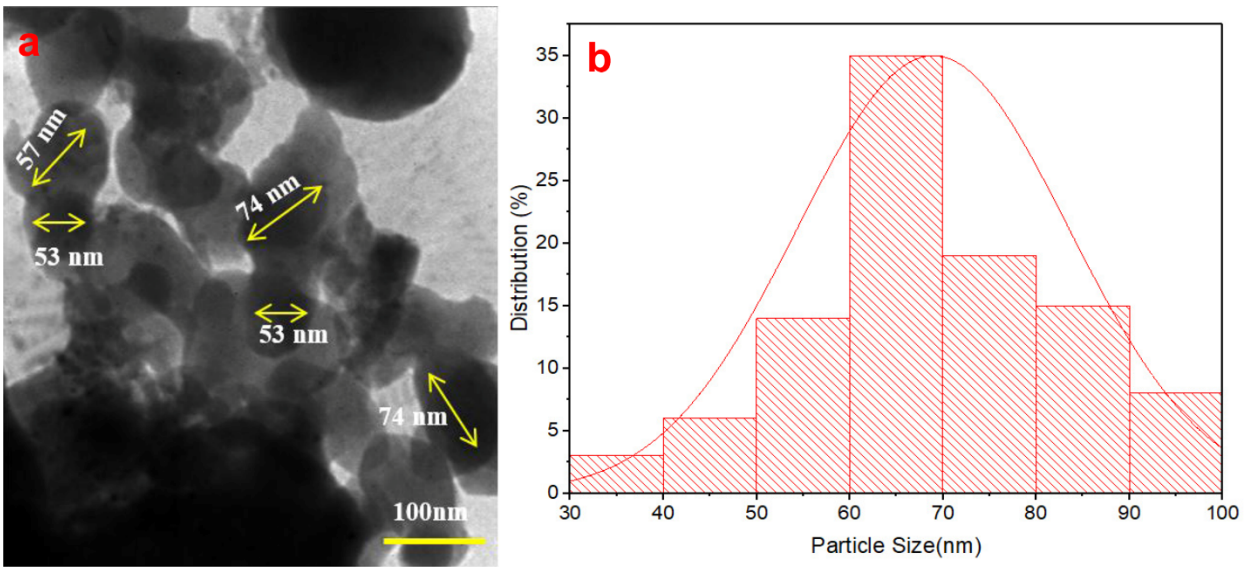

Fig. 1. (a) TEM micrograph of the colloidal copper nanoparticle, and (b) histogram of particle size.

Figure 2 SEM micrographs of the cross-section of Ni-Cup-P and Ni-P electroless coatings deposited at the same conditions (temperature, pH, and stirring speed) for 90 min. According to the obtained thicknesses, the deposition rate in electroless Ni-P and electroless Ni-Cup-P baths is 9.8 and 11 µm/h, respectively. An increase in the deposition rate of a bath containing copper nanoparticles in the bath is related to the copper nanoparticles as an external surface with self-catalytic properties and a high active surface. It should be noted that electroless reactions are catalytic in that the reaction energy is supplied at high temperatures (60 °C ≤ T ≤ 95 °C) [17]. In electroless baths, the surface of the sample and any external agents, including nanoparticles, the wall of the plating chamber, and the elements in the solution play the role of catalyst, and nickel ions tend to deposit on these surfaces [7,8]. In this case, nickel ions approach the surface of these catalysts, and with the reduction conditions created by sodium hypophosphite, nickel ions are reduced to metal. Therefore, in the Ni-Cu-P electroless bath, copper metal nanoparticles, which have a high surface-to-volume ratio, act as a catalyst, resulting in a higher deposition rate than the Ni-P electroless solution. According to Figure 2, it can be seen that in the interface, complete adhesion has been established between the coating and the substrate without any pores. It is evident that a dense coating has been obtained, which increased the corrosion resistance.

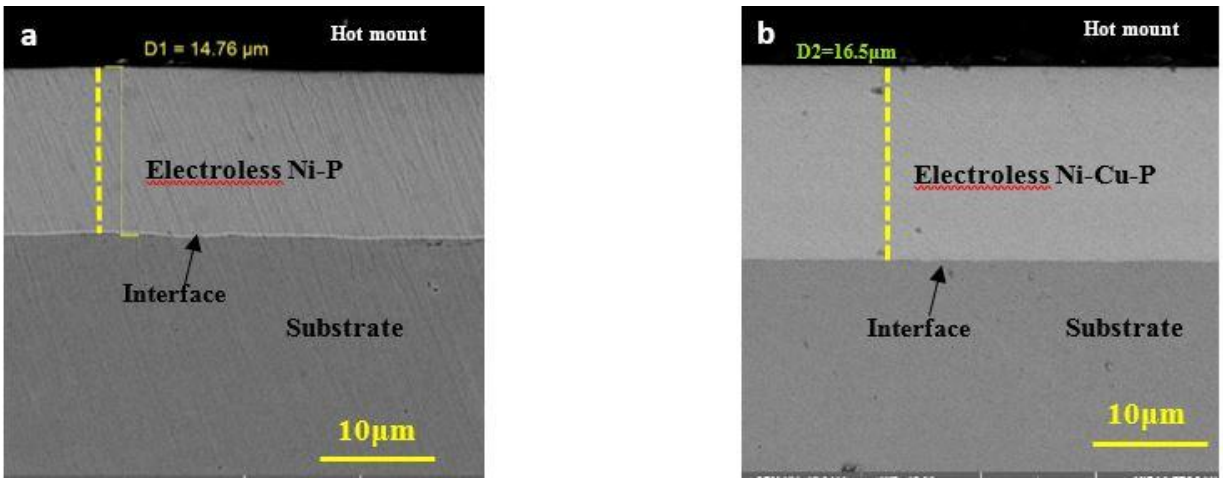

Fig. 2. FESEM micrographs of the cross section of the coating deposition for 90 min: (a) Electroless Ni-P, and (b) Electroless Ni-Cu-P coating.

Figure 3 shows the EDS analysis of electroless Ni-P and electroless Ni-Cu-P coatings. According to the presented chemical composition, the amount of P in both coatings is higher than 10%, and these types are in the category of high phosphorus. On the other hand, the percentage of phosphorus in Ni-Cu-P electroless coating is higher than in Ni-P electroless coating, which shows that the presence of copper nanoparticles, in addition to increasing the deposition rate, could also increase the percentage of phosphorus in the coating. This increase in phosphorus in the Ni-Cu-P coating indicates that the

presence of copper particles causes sodium hypophosphite, which has a reducing and supplying role of phosphorus, to a greater extent in the reduction reaction of nickel ions than in the Ni-P coating. Also, considering that about 300 mg/L of copper nanoparticles were added to the electroless solution as colloidal particles, 4.58wt% or 3.86 at% of these adsorbed particles were detected. Figure 4 EDS map analysis of the electroless Ni-Cu-P coating. As can be seen, the Ni, P, and Cu elements were detected, and uniform distribution of the Ni, P, and Cu elements was achieved. The uniform distribution of copper nanoparticles in the coating can be an advantage of using colloidal copper nanoparticles instead of nanoparticles. In such a way that the copper nanoparticles are uniformly distributed in the solvent containing the surfactant and there is no possibility of its sedimentation by stirring the solution.

(a)

Element	Wt%	At%
Ni	82.85	74.64
Cu	4.85	3.86
P	12.57	21.5

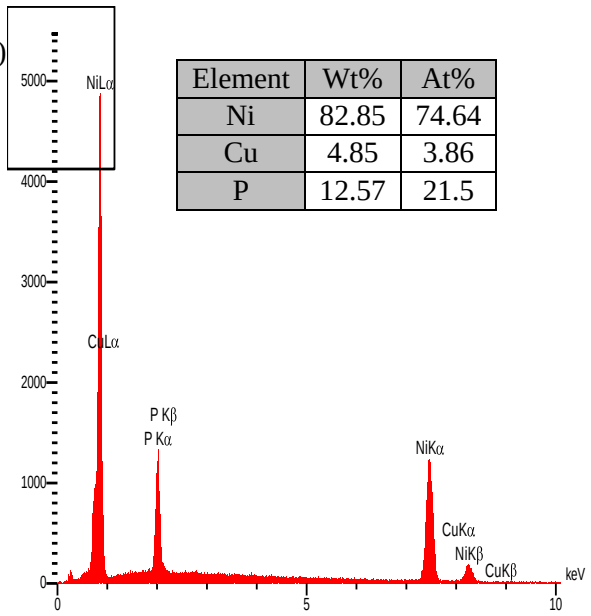

(b)

Element	Wt%	At%
Ni	88.48	80.37
P	11.52	19.63

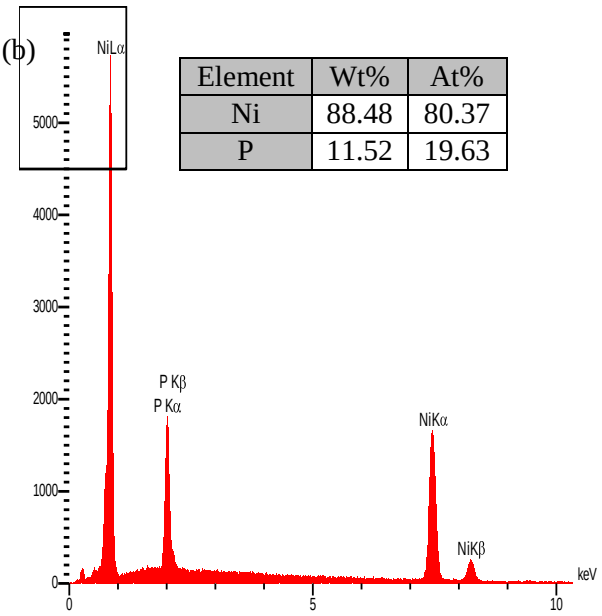

Fig. 3. EDS analysis of the coating: (a) Electroless Ni-P, and (b) Electroless Ni-Cu-P coating

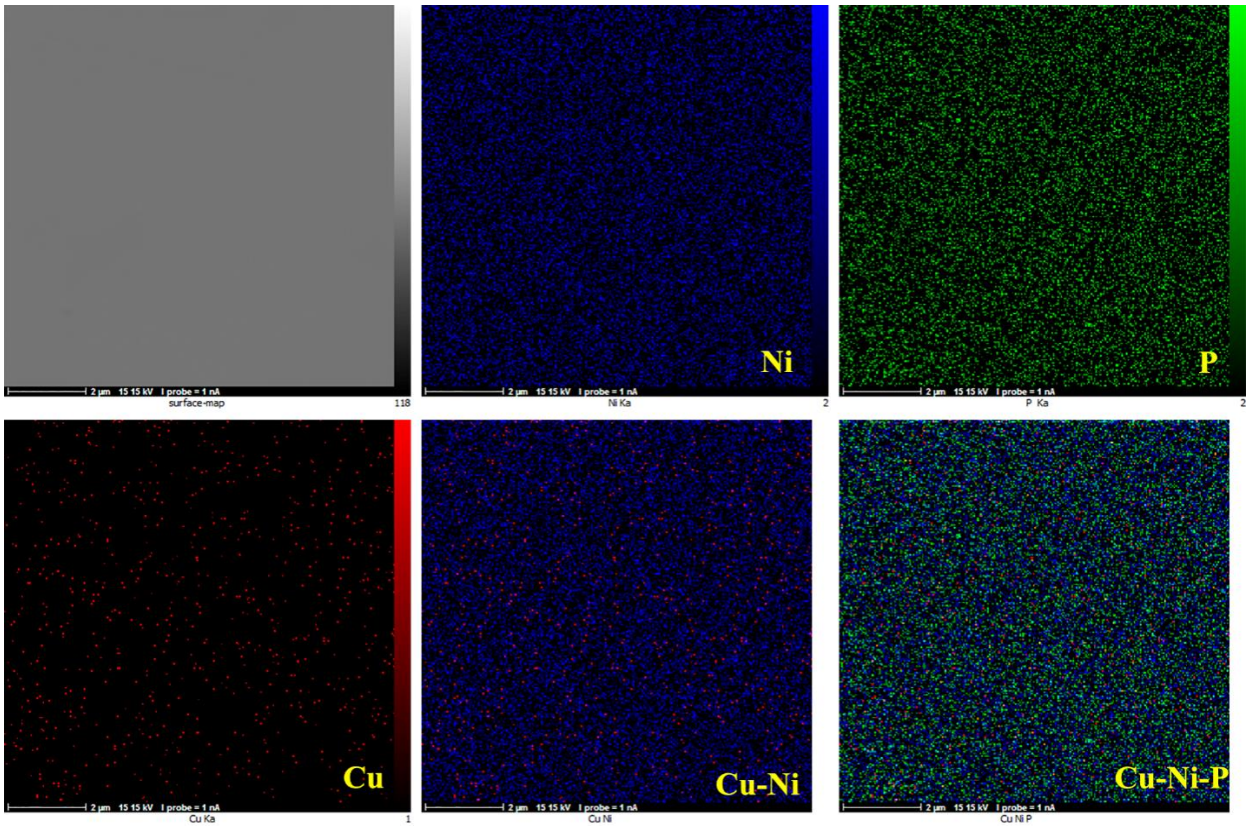

Fig. 4. Elemental map analysis of the Ni-Cu-P coating.

Figure 5 shows the XRD patterns of the electroless Ni-P and Ni-Cu-P coatings before and after heat treatment at 300 °C for 3 h and 400 °C for 1 h. According to the XRD patterns of the samples before heat treatment, both coatings have an amorphous structure, and the presence of copper in the Ni-Cu-P coating has no effect on the crystal microstructure. It is reported that the structural change in the electroless process depends only on the pH and temperature of the electroless bath [16]. On the other hand, heat treatment in both coatings has caused the microstructure to transform to a crystalline state. In this case, the supersaturated amorphous solution in Ni-P coating is transformed to the Ni_{α} and nickel phosphate (Ni_3P) equilibrium phases and in Ni-Cu-P coating transformed to the Ni_{α}, Ni_3P, and $Ni_{3.8}Cu$ phases.

Figure 6 shows the micro-hardness of the electroless Ni-P and Ni-Cu-P coatings after different heat treatments. It can be seen that the micro-hardness of the coatings after heat treatment at 400 °C for Ni-P and Ni-Cu-P coatings was approximately 87% and 73% increase, respectively, compared to before heat treatment. Also, in Ni-Cu-P coating, the presence of copper nanoparticles has increased the hardness. Increased hardness of coatings due to the transformation of the microstructure from amorphous to crystalline during heat treatment and the grain boundaries formation [16, 20]. Furthermore, the presence of Ni_3P phase in Ni-P coating and Ni_3P and $Ni_{3.8}Cu$ phases in Ni-Cu-P coating.

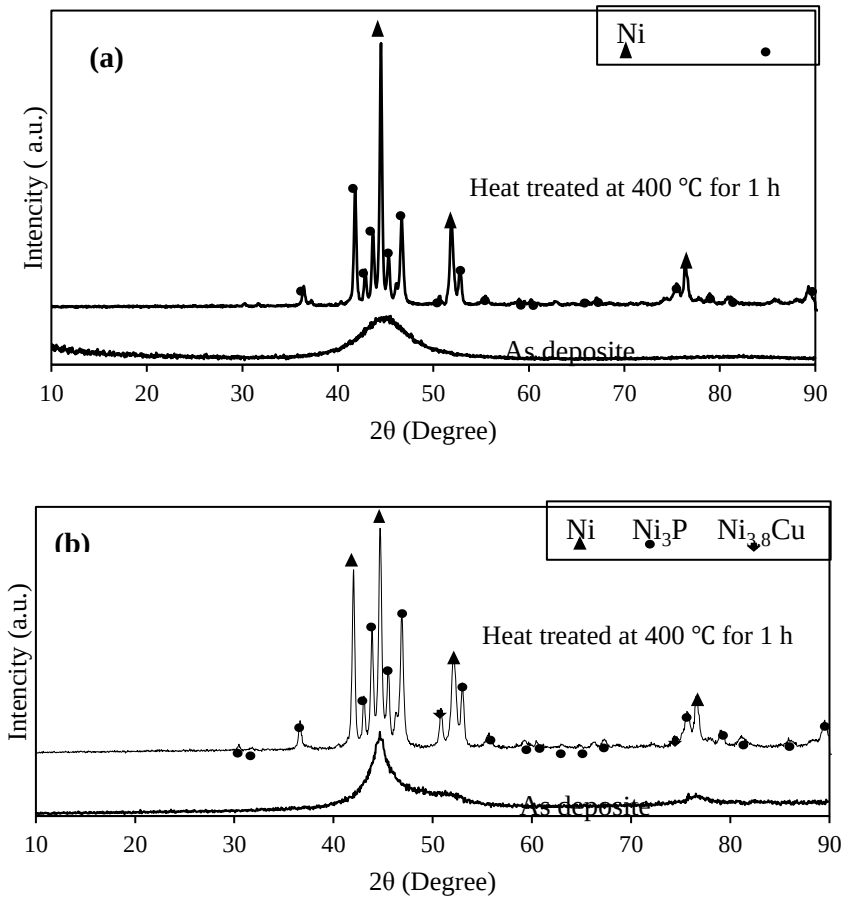

Fig. 5. XRD patterns of the samples before and after heat treatment: (a) Ni-P, and (b) Ni-Cu-P sample.

4. Conclusions

The deposition rate of Ni-Cu-P and Ni-P coatings was applied by the electroless method in an acidic pH bath at 85 °C on an L80 steel substrate was investigated. Experimental results showed that heat treatment at 400 °C and transforming the structure from amorphous to crystalline in both coatings leads to the formation of Ni_{α}, Ni_3P, and $Ni_{3.8}Cu$ phases. Also, colloidal copper nanoparticles in electroless solution, in addition to forming the $Ni_{3.8}Cu$ phase, increase the deposition rate from 10 to 11 µm/h. On the other hand, the presence of copper nanoparticles in the coating before and after heat treatment leads to a significant increase in hardness in the Ni-Cu-P coating compared to the Ni-P coating.

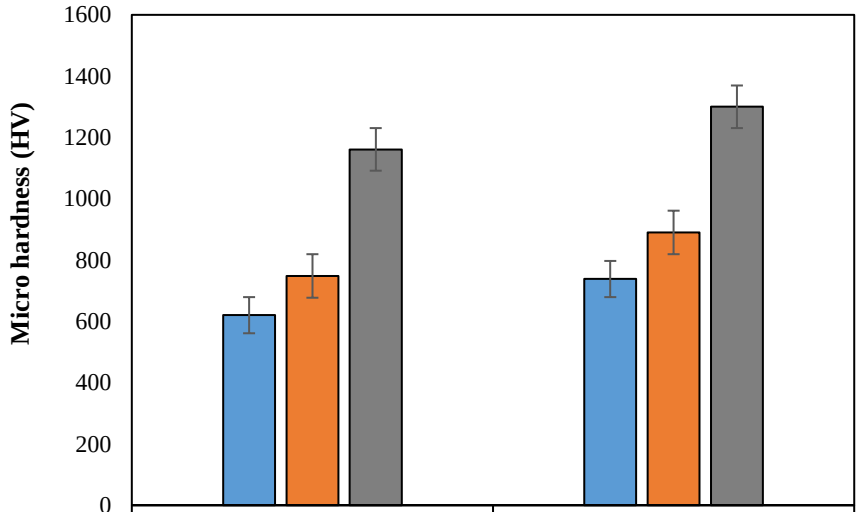

	Electroless Ni-P	Electroless Ni-Cu-P
without Heat treatment	620	738
Heat treatment at 200C	748	890
Heat treatment at 400C	1161	1300

Fig. 6. Micro-hardness of the Ni-P and Ni-Cu-P coating before and after heat treatment.

References

[1] Petroleum and natural gas industries—Steel pipes for use as casing or tubing for wells, Specification for Casing and Tubing API Specification 5CT Eighth Edition, ISO 11960. (2005).

[2] Robert Heidersbach, Metallurgy and Corrosion Control in Oil and Gas Production, John Wiley Sons, Inc. (n.d.), 2018.

[3] F. Bigdeli, M. Javidi, M. Pakshir, A. Khezrloo, M. Tayebi, Risk assessment of the corrosion resistance performances for epoxy coatings under drilling environments using AHP method, Int. J. Press. Vessel. Pip. 193 (2021) 104470.

[4] C. Sun, J. Li, S. Shuang, H. Zeng, J.-L. Luo, Effect of defect on corrosion behavior of electroless Ni-P coating in CO_2-saturated NaCl solution, Corros. Sci. 134 (2018) 23–37.

[5] masoud soltani, A. Shafyei, K. Zarrin naghsh, R. Aliramezani, Effect of Ni-P electroless coating and heat treatment on tribological and corrosion properties of copper substrate, J. Adv. Mater. Process. 6 (2018) 3–13.

[6] D. Davoodi, R. Miri, A.H. Emami, M. Tayebi, S. Salahshour, The effect of NiO catalyst on reduction, synthesis and binder content of TiC-Ni nanocomposite, Int. J. Refract. Met. Hard Mater. 88 (2020) 105175.

[7] J. Sudagar, J. Lian, W. Sha, Electroless nickel, alloy, composite and nano coatings – A critical review, J. Alloys Compd. 571 (2013) 183–204.

[8] A. Chami, B. Nasiri Tabrizi, Effect of heating rate on morphological features of oxidized electroless nickel–boron coatings, J. Adv. Mater. Process. 3 (2015) 61–70.

[9] S.R. Anvari, S.M. Monirvaghefi, M.H. Enayati, Fabrication and characterization of nanostructured functionally graded Ni-P electroless coating, J. Adv. Mater. Process. 4 (2016) 19–29.

[10] I.R. Mafi, C. Dehghanian, Comparison of the coating properties and corrosion rates in electroless Ni–P/PTFE composites prepared by different types of surfactants, Appl. Surf. Sci. 257 (2011) 8653–8658.

[11] A. Arumugam, P. Lakshmanan, S. Palani, K. Parthiban, Wear behavior of Ni-P and Al_2O_3 electroless nano coating on aluminium alloy, Mater. Today Proc. 46 (2021) 1066–1070.

[12] M. Khodaei, A.M. Gholizadeh, SiC nanoparticles incorporation in electroless NiP-Graphene oxide nanocomposite coatings, Ceram. Int. 47 (2021) 25287–25295.

[13] C. Wang, Z. Farhat, G. Jarjoura, M.K. Hassan, A.M. Abdullah, Indentation and bending behavior of electroless Ni-P-Ti composite coatings on pipeline steel, Surf. Coatings Technol. 334 (2018) 243–252.

[14] J. Li, C. Sun, M. Roostaei, M. Mahmoudi, V. Fattahpour, H. Zeng, J.-L. Luo, Characterization and corrosion behavior of electroless Ni-Mo-P/Ni-P composite coating in $CO_2/H_2S/Cl^-$ brine: Effects of Mo addition and heat treatment, Surf. Coatings Technol. 403 (2020) 126416.

[15] S. Du, Z. Li, Z. He, H. Ding, X. Wang, Y. Zhang, Effect of temperature on the friction and wear behavior of electroless Ni–P–MoS2–CaF2 self-lubricating composite coatings, Tribol. Int. 128 (2018) 197–203.

[16] I. Rose, C. Whittington, Nickel Plating

Handbook, Belgium, 2014.
[17] M. Czagany, P. Baumli, Effect of pH on the characteristics of electroless Ni-P coatings, J. Min. Metall. Sect. B Metall. 53 (2017) 20.
[18] F. Tabatabaei, K. Raeissi, A. Saatchi, M. Ürgen, Effect of sodium sulfate on the characteristics and corrosion behavior of high phosphorus Ni–P electroless coatings, Mater. Corros. 65 (2014) 926–930.
[19] S. Kundu, S.K. Das, P. Sahoo, Friction and wear behavior of electroless Ni-P-W coating exposed to elevated temperature, Surfaces and Interfaces. 14 (2019) 192–207.
[20] S. Elahinejad, H. Sharifi, M. Tayebi, A. Rajaee, The influence of nickel coating on the interface of pressureless infiltrated with vibration Al-SiC composites, Mater. Res. Express. 4 (2017) 116506.

JMATPRO	Journal of Advanced Materials and Processing 10 (2): 11-18, Spring 2022 http://jmatpro.iaun.ac.ir 20.1001.1.2322388.2022.10.2.2.7

Research Paper

Thermal Stability and Dynamic Magnetic Properties of NiO/Fe Multilayered Thin Films Prepared by Oblique-Angle Sputtering Technique

Khalil Gheisari[1*], C.K. Ong[2]

1. Department of Materials Science and Engineering, Faculty of Engineering, Shahid Chamran University of Ahvaz, Ahvaz, Iran

2. Center for Superconducting and Magnetic Materials, Department of Physics, National University of Singapore, Singapore

ARTICLE INFO

Article history:

Received 5 February 2022
Accepted 18 March 2022
Available online 1 April 2022

Keywords:
Thin films
Sputtering
Magnetic anisotropy
NiO/Fe Film
Ferromagnetic resonance frequency

ABSTRACT

In this work, the bilayer NiO/Fe thin films compared with single-layer Fe film were deposited on Si (100) substrate using the sputtering technique at deposition angles of 0° and 31.5°. Structure, the static magnetic properties, and the temperature dependence of the dynamic magnetic properties in the range from 300 K to 420 K have been investigated. The results show that the nanocrystalline BCC phase of Fe with the average crystallite size of 11-12 nm and (110) preferred orientation is formed during the deposition process. The resonance frequency is found to rise from 1.03 GHz to 1.13 GHz by employing the NiO sublayer for the typically deposited Fe film. Moreover, the resonance frequency increases for the NiO/Fe films from 1.13 GHz to 1.67 GHz as the deposition angle increases from 0° and 31.5° as a result of the increase in the magnetic anisotropy from 16 Oe to 45 Oe. The permeability values decrease for both as-deposited films with increasing temperature; however, the higher values of the permeability are observed for the film obtained at a deposition angle of 31.5°.

Citation: Gheisari, Kh.; Ong, C.K. (2022). Thermal Stability and Dynamic Magnetic Properties of NiO/Fe Multilayered Thin Films Prepared by Oblique-Angle Sputtering Technique, Journal of Advanced Materials and Processing, 10 (2), 11-18. Dor: 20.1001.1.2322388.2022.10.2.2.7

[*] **Corresponding Author**
E-mail Address: khalil.gheisari@yahoo.com

1. Introduction

Nanocrystalline Fe thin films due to their high saturation magnetization can be a good candidate for use in microwave applications such as wireless communication devices, electromagnetic noise absorbers, magnetic recording media, inductive devices, etc. [1-3]. Nevertheless, the application of the as-deposited Fe thin films is rather restricted because of their poor dynamic magnetic properties; hence, several attempts have been made to improve their high-frequency magnetic properties, including using oblique deposition [4], inserting antiferromagnetic underlayer (AF) [5], composition modification [6], and so on. Oblique deposition is an effective and simple technique to modify dynamic magnetic properties [7]. During the oblique deposition process, when an external magnetic field is applied in the substrate plane parallel to the easy axis direction, a high in-plane uniaxial magnetic anisotropy is induced, leading to an increment in the ferromagnetic-resonance frequency (f_{FMR}). Therefore, the as-deposited magnetic thin film can keep the high permeability in the gigahertz frequency range, which is desirable for high-frequency applications [1, 8, 9]. Up to now, several antiferromagnet sublayers such as MnIr [5, 10] and NiO [11] have been used to grow magnetic thin films by sputtering oblique deposition techniques to achieve the desired performance for high-frequency applications. However, there are few works in the literature focusing on the improvement of high-frequency magnetic via simultaneous use of inserting AF sublayer and oblique deposition. The present work aims to prepare Fe thin film using NiO AF sublayer through the oblique-angle sputtering. Regarding the literature in this area, no attempts have been made to optimize the resonance frequency of Fe thin films by the simultaneous use of inserting NiO sublayer and oblique deposition.

2. Material and methods

The bilayer NiO (~25 nm)/Fe (~100 nm) thin films were deposited on 10 × 5 × 0.5 mm^3 Si (100) substrate at deposition angles of 0° and 31.5° using an 80 W radio-frequency magnetron sputtering. The base pressure of the sputtering chamber and the Ar working pressure were maintained around 10^{-7} Torr and 10^{-3} Torr, respectively. During deposition, a magnetic field of 200 Oe was applied in the substrate plane parallel to the easy axis direction. To compare the effect of the NiO sublayer, the regular deposited single-layer Fe thin film was prepared under similar conditions.

The phase analysis was carried out via X-ray diffraction (XRD, Philips Analytical X-ray Diffractometer with Cu Ka radiation). The static magnetic properties of the as-deposited film were measured using an M–H loop tracer. The high-frequency magnetic properties of the as-deposited film were obtained using a vector network analyzer (Agilent N5230A) in the temperature range of 330-420 K and the frequency range of 0.1 to 10 GHz.

3. Results and discussion

Fig. 1 shows the XRD patterns of the bilayer Fe thin films with the employment of the NiO sublayer at the deposition angles of 0° and 31.5°, as well as the regular deposited single-layer Fe thin film. In all cases, the isolated diffraction peak observed at around 2θ ≈44.3° (JCPDS card no. 01-085-1410) shows that the BCC phase of Fe has been growing during the deposition process. The observed diffraction line has been matched with the (110) characteristic line of Fe. On the other hand, the other characteristic diffraction lines of the BCC phase have not appeared indicating that a crystalline anisotropy (directionality dependence of properties) has been developed. It means that the magnetic easy axis lies along a particular direction [12].

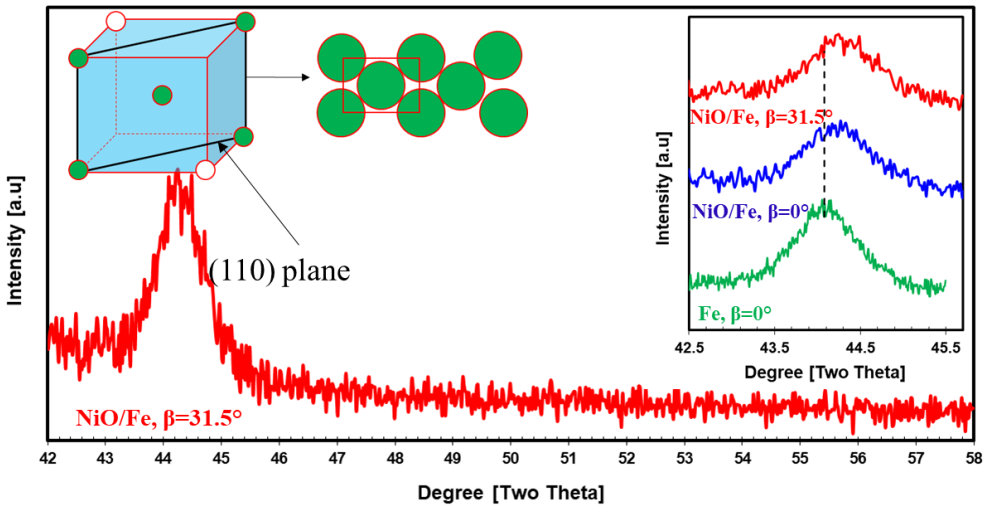

Fig. 1. X-ray diffraction patterns of the Fe film at deposited at oblique angles of 0° as well as the bilayer NiO/Fe films deposited at oblique angles of 0° and 31.5°.

As it can be seen, the characteristic diffraction peaks of the NiO sublayer cannot be observed in the bilayer NiO/Fe films, probably owing to restricted penetration of the primary X-ray beam, very thin NiO sublayer, and low degree of crystallinity in the NiO sublayer. Likewise, in some of the published papers, the characteristic diffraction lines of the underlayers were not observed in the corresponding XRD patterns. For example, Zhong et al. [1] fabricated FeCo thin film with the employment of Co underlayer using an oblique deposition. In contrast to the achievement of excellent microwave performance by Zhong et al. [1] via both oblique deposition and Co underlayer, the individual diffraction lines of the Co underlayer were not observed.

However, the direct effect of the magnetic thin film appears on the XRD pattern and magnetic properties of the obtained films. In comparison to the single-layer Fe film, a slight peak shift of (110) diffraction line towards higher diffraction angles can be observed for the normally deposited NiO/Fe film, indicating a contraction in the lattice spacing. This lattice spacing shrinking may be ascribed to the compressive residual stress developed inside the Fe film due to the employment of the sublayer [13]. The residual stress development in sputter-deposited thin films has been reported previously in magnetic film [14]. Concerning literature data, thin-film residual stresses are formed as a result of the dissimilar thermal-expansion coefficients of the substrate, underlayer, and magnetic film [13].

As reported in the literature, a gradual shift in the diffraction angle may be observed with increasing deposition angle [4]. Nonetheless, the diffraction angle is not changed significantly with the oblique angle, indicating that a shrinking or expansion of the interplanar spacing has not occurred for the bilayer NiO/Fe films when the deposition angle increases from 0° to 31.5°. Accordingly, a BCC phase with the lattice parameter of 2.889 nm in both films grows during the deposition process. Moreover, a significant (110) diffraction line broadening is observed owing to the reduction of crystallite size to the nanometer level.

Based on Scherer's equation, the average value of crystallite size lies in the range of 11-12 nm, showing a good agreement with those reported for the as-deposited soft magnetic films [15, 16]. As a result, a nanocrystalline BCC phase of Fe with the preferred orientation is obtained in both cases. Hysteresis loops of the as-deposited films along the hard axis and easy axis are displayed in Figure 2. The coercivity along hard (H_{ch}) and easy (H_{ce}) axes, as well as the uniaxial anisotropy field (H_k), were extracted from hysteresis loops and tabulated in Table 1.

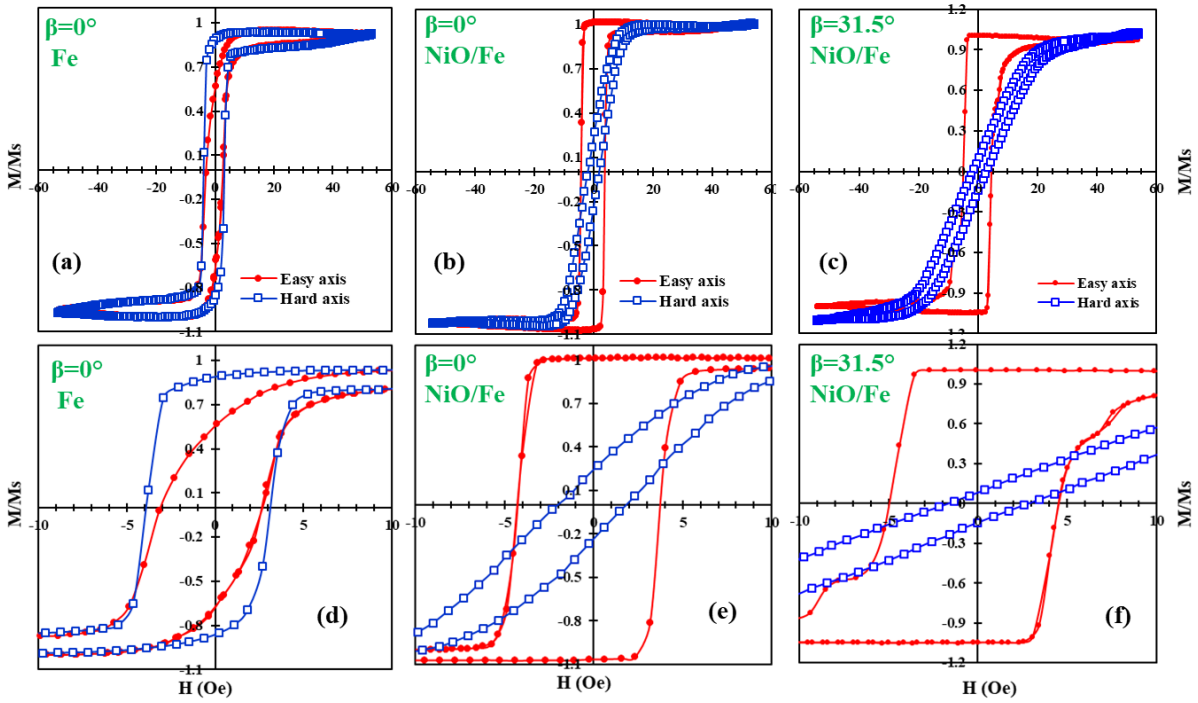

Fig. 2. (a, b, c) M/Ms–H loops along easy and hard axes of the Fe film and the bilayer NiO/Fe films deposited at various oblique angles. (d, e, f) A magnified view of M/Ms–H loops extracted from (a, b).

Table 1. Coercivity along hard axis H_{ch} and easy axis H_{ce}, anisotropy field H_k, and resonance frequency f_{FMR} for the as-deposited films.

Sample	β(°)	H_{ce}(Oe)	H_{ch}(Oe)	H_k(Oe)	f_{FMR}(GHz)
Fe	0	2.9	3.5	9	1.03
NiO/Fe	0	4.0	1.9	16	1.13
NiO/Fe	31.5	4.7	2.2	45	1.67

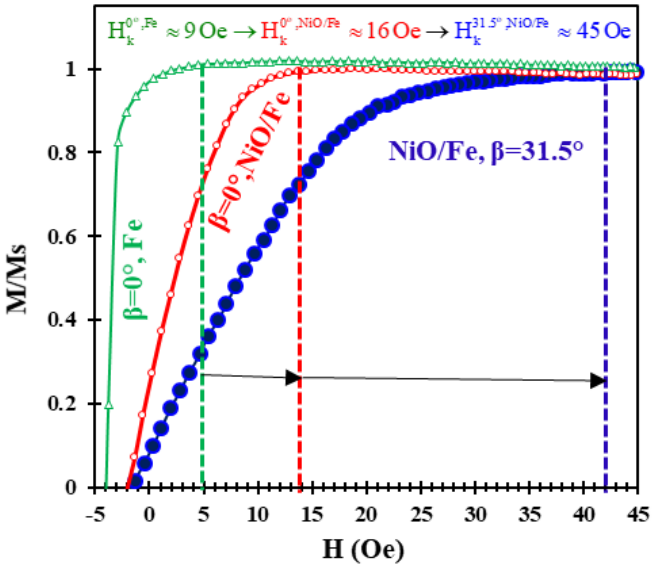

Fig. 3. Estimation of the static uniaxial anisotropy field H_k from hard axis M/Ms–H loops for the Fe film and the bilayer NiO/Fe films deposited at the various oblique angles.

As shown, in contrast to the hard M-H loop of the Fe film that exhibits a square shape, the slanted ones are observed for those obtained in NiO/Fe films, indicating that the NiO sublayer results in an in-plane anisotropy during the deposition process of Fe films on the NiO layer. It is worth noting that a square M-H loop along the hard axis was also detected for the 15 nm Fe film deposited on the Si wafer (100) by Belusky et al. [17]. However, the magnetic properties are improved by of NiO underlayer as a result of the induced in-plane anisotropy. In-plane magnetic anisotropy can be ascribed to the formation of the columnar microstructure in the oblique-angle deposition [4]. Furthermore, this figure also shows that a more slanted hard M-H loop is detected for NiO/Fe film at the deposition angle of 31.5°, representing that the anisotropy field qualitatively rises with an oblique angle.

The static uniaxial anisotropy field H_k can be measured quantitatively from the saturation field along the hard axis [18], as shown in Fig. 3. Accordingly, the anisotropy field increases from 9 Oe to 16 Oe when the Fe film normally deposited on the NiO sublayer. Further improvement is achieved for NiO/Fe films in such a way that H_k risers from 16 Oe to 45 Oe as the deposition angle increases from 0° to 31.5°. Enhancement of the H_k with the deposition angle has been reported previously [1, 2, 4, 5, 7, 10, 19].

It is worthwhile to state that in-plane magnetic anisotropy is generated owing to the formation of the columnar microstructure in such a way that the tilt angle of the columnar grains toward the deposition incidence increases as the deposition angle increases [10], increasing the anisotropy field. This magnetic anisotropy causes not only by the magnetocrystalline anisotropy of the tilted columnar grains but also by the shape anisotropy of the elongated columnar morphology [20]. However, the low values of the coercivity (1.9-4.7 Oe) exhibit good soft magnetic properties of the as-deposited film. The low values of coercivity can be attributed to the nanocrystalline structure of as-deposited films. Based on Herzer's random anisotropy model, in the nanocrystalline structure, when crystallite size *D* is smaller than the magnetic exchange length, the coercivity values are controlled by the D^6-power law. Consequently, with decreasing the crystallite size, the coercivity value decreases considerably. On the other hand, since the crystallite sizes of the as-deposited films here (11-12 nm) are lower than the magnetic exchange length of Fe (~15 nm) [21], low coercivity values are obtained. The dynamic magnetic properties containing the real and imaginary components of permeability (μ', μ'') are displayed in Fig. 4. The typical behavior of the permeability spectra, including rapidly rising with frequency followed by a sudden drop, can be

observed in all ad-deposited films. However, the ferromagnetic-resonance frequency (f_{FMR}), which shows a sharp peak, increases with deposition angle. It should be mentioned that f_{FMR} is well-known as the most important parameter of dynamic magnetic properties. After that, the magnetic permeability approaches the order of unity and restricts the applicable range of microwave devices [9].

The increase of the f_{FMR} results from the increase of H_k. Concerning Kittel's equation, the f_{FMR} is proportional to the square root of the H_k [10]; consequently, the increase of H_k positively affects the value of f_{FMR}, as shown in Fig. 4. Employment of NiO sublayer for normally deposited Fe film leads to a slight increase of f_{FMR} from 1.03 GHz to 1.13 GHz. However, simultaneous use of both oblique deposition and NiO underlayer as an appealing approach to fabricate magnetic thin films rises f_{FMR} to 1.67 GHz. Similar findings through a similar approach have been reported for FeCo thin films to obtain high resonance frequency [1].

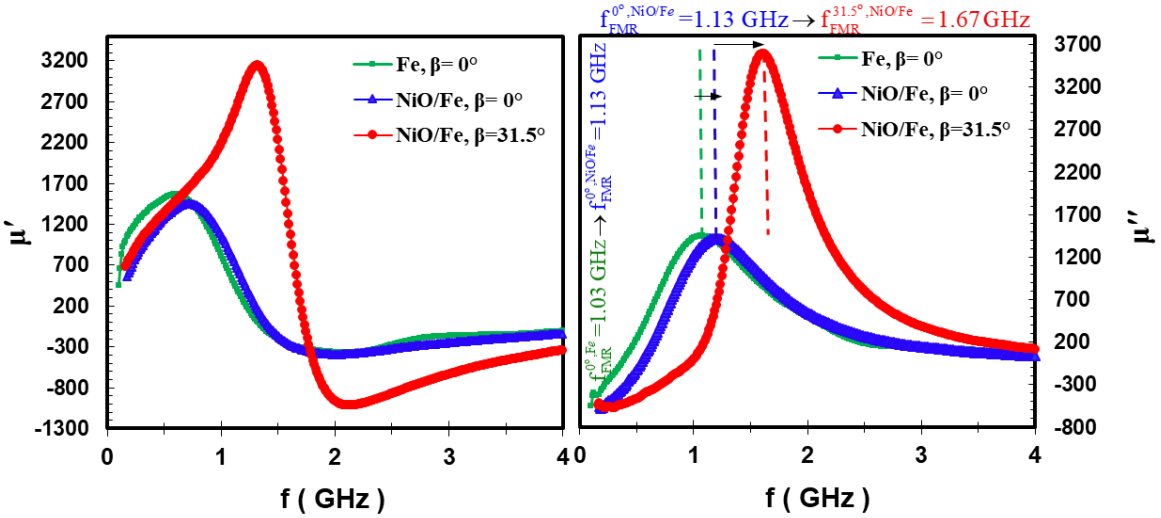

Fig. 4. Permeability spectra of the Fe film and the bilayer NiO/Fe films deposited at the various oblique angles.

The permeability spectra of the as-deposited thin films obtained at room temperature are shown as a function of the external magnetic fields (H_{ex}) in Fig. 5. As expected, the f_{FMR} shifts to a higher frequency with rising the H_{ex}. With increasing H_{ex} from 0 to 150 Oe, f_{FMR} increases from 1.13 to 5.45 GHz and from 1.67 to 5.58 GHz for the film deposited at β=0° and β=31.5°, respectively. This finding shows that a f_{FMR} indicates a directional dependent on H_{ex} which is consistent with the results found in the literature [22]. Furthermore, with increasing the H_{ex}, the initial permeability decreases, which in turn, leads to an increase in the resonance frequency. This behavior shows the permeability spectra follow well Snoek's law [4].

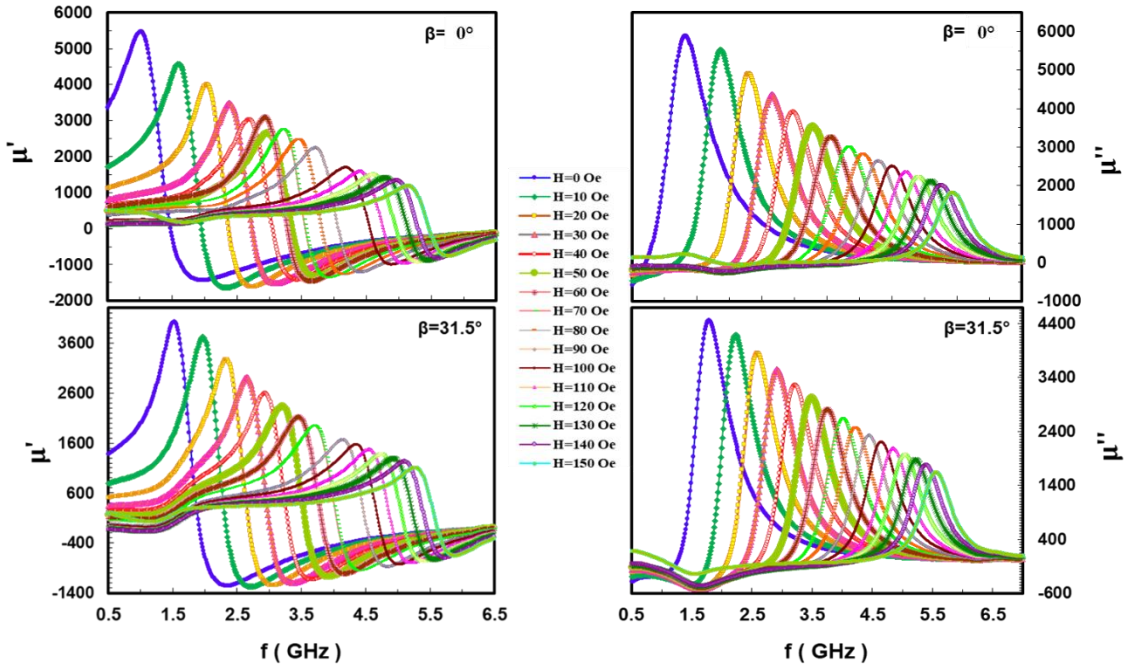

Fig. 5. Permeability spectra as a function of the external magnetic fields for the bilayer NiO/Fe films deposited at oblique angles of 0° and 31.5°.

The permeability spectra as a function of the working temperature measured in the range of 300-420 K are shown in Fig. 6. The value of both components of permeability decrease with the increase in temperature. The downward trend of the permeability with temperature results from the decrease of the saturation magnetization with temperature [23]. In fact, because of the exacerbation of thermal perturbation of magnetization at higher temperatures, the saturation magnetization decreases, and hence, the magnetic permeability starts to decrease. However, both films display good thermal stability up to 330 K. Although, the magnetic permeability destroys sharply at the higher temperature. Generally, the film deposited at oblique angles of 31.5° shows a higher magnitude of permeability even at a higher temperature.

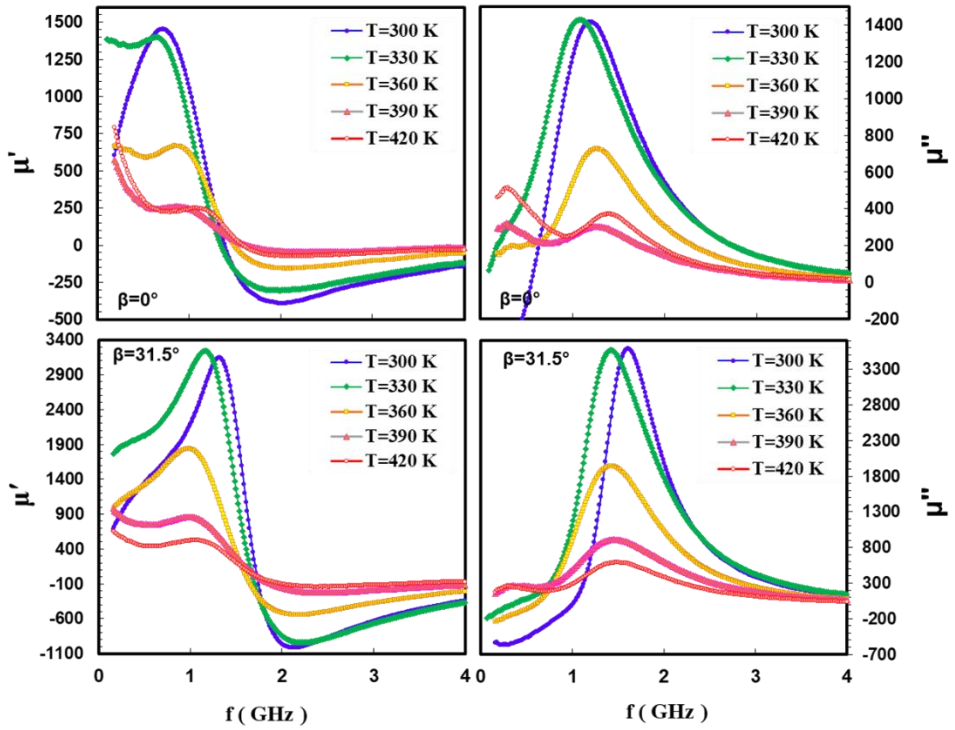

Fig. 6. Permeability spectra as a function of temperature for the bilayer NiO/Fe films deposited at oblique angles of 0° and 31.5°.

4. Conclusions

In this work, the bilayer sputtered NiO/Fe thin films were deposited on Si (100) substrate at deposition angles of 0° and 31.5°. To compare the effect of the NiO sublayer, the regular deposited single-layer Fe thin film was also fabricated under similar conditions. It is found that the NiO underlayer plays an important role in the magnetic properties of the nanocrystalline Fe thin film in such a way that the anisotropy field rises from 9 Oe to 16 Oe and the ferromagnetic resonance frequency rises from 1.03 GHz to 1.13 GHz by the employment of the NiO sublayer for the normally deposited film. Moreover, in NiO/Fe films, with an increasing deposition angle from 0° to 31.5°, the anisotropy field increases abruptly from 16 Oe to 45 Oe; consequently, the resonance frequency increases from 1.13 GHz to 1.67 GHz. Due to the decrease of saturation magnetization with temperature, the permeability values decrease with temperature; however, the film obtained at a deposition angle of 31.5° exhibits higher values of permeability at all temperatures.

Acknowledgments

This work was supported by the Shahid Chamran University of Ahvaz (Grant No. SCU.EM1400.222) and the National University of Singapore.

References

[1] X. Zhong, N.N. Phuoc, Y. Liu, C. Ong, Employment of Co underlayer and oblique deposition to obtain high resonance frequency and excellent thermal stability in FeCo thin films, Journal of magnetism and magnetic materials, 365 (2014) 8-13.

[2] X. Zhu, Z .Wang, Y. Zhang, L. Xi, J. Wang, Q. Liu, Tunable resonance frequency of FeNi films by oblique sputtering, Journal of magnetism and magnetic materials, 324 (2012) 2899-2901.

[3] L. Phua, N. Phuoc, C. Ong, Effect of Ni concentration on microstructure, magnetic and microwave properties of electrodeposited NiCoFe films, Journal of alloys and compounds, 543 (2012) 1-6.

[4] K. Gheisari, C. Ong, Magnetic properties and thermal stability of nanocrystalline Fe films prepared by oblique sputtering deposition method, Physica B: Condensed Matter, 595 (2020) 412365.

[5] K. Gheisari, C. Ong, Enhancing High-Frequency Properties of Nanocrystalline Sputtered Fe Thin Films by Using MnIr Underlayer and Oblique Deposition, Journal of Superconductivity and Novel Magnetism, 3-5- 1 (2021) 4.

[6] L. Phua, N. Phuoc, C. Ong, Investigation of the microstructure, magnetic and microwave properties of electrodeposited NixFe1− x (x= 0.2–0.76) films, Journal of alloys and compounds, 520 (2012) 132-139.

[7] X. Zhong, N.N. Phuoc, G. Chai, Y. Liu, C. Ong, Thermal stability and dynamic magnetic properties of FeSiAl films fabricated by oblique deposition, Journal of alloys and compounds, 610 (2014) 126-131.

[8] Y. Fukuma, Z. Lu, H. Fujiwara, G. Mankey, W. Butler, S. Matsunuma, Strong uniaxial magnetic anisotropy in CoFe films on obliquely sputtered Ru underlayer, in, American Institute of Physics, 2009.

[9] N.N. Phuoc, C. Ong, FeCoHfN thin films fabricated by co-sputtering with high resonance frequency, Journal of alloys and compounds, 509 (2.٤٠١٣-٤٠١٠ (٠١١

[10] N.N. Phuoc, G. Chai, C. Ong, Enhancing exchange bias and tailoring microwave properties of FeCo/MnIr multilayers by oblique deposition, Journal of Applied Physics, 112 (2012) 113908.

[11] B.K. Kuanr, R. Camley, Z. Celinski, Exchange bias of NiO/NiFe: Linewidth broadening and anomalous spin-wave damping, Journal of applied physics, 93 (2003) 7723-7725.

[12] S. Husain, V. Barwal, N.K. Gupta, S. Hait, S. Chaudhary, Tunable magnetic anisotropy in obliquely sputtered Co60Fe40 thin films on Si (100), Physica B: Condensed Matter, 570 (2019) 1-5.

[13] C. Hsu, S. Chen, W. Liao, F. Yuan, W. Chang, J. Tsai, Effect of Pt underlayer on the coercivity of FePt sputtered film, Journal of alloys and compounds, 449 (2008) 52-55.

[14] X. Liu, H. Kanda, A. Morisako, The effect of underlayers on FeCo thin films, in: Journal of Physics: Conference Series, IOP Publishing, 2011, pp. 012037.

[15] G. Chai, N.N. Phuoc, C. Ong, Optimizing high-frequency properties of stripe domain ferrite doped CoFe thin films by means of a Ta buffer layer, Journal of Physics D: Applied Physics, 46 (2013) 415001.

[16] Z. Liu, C. Ong, Microstructure and thickness dependent magnetic properties of nanogranular Co–Zn–O thin films for microwave applications, Journal of alloys and compounds, 509 (2011) 10075-10079.

[17] M. Belusky, S. Lepadatu, J. Naylor, M. Vopson, Study of roughness effect in Fe and Co thin films prepared by plasma magnetron sputtering, Physica B: Condensed Matter, 574 (2019) 411666.

[18] M. Zölfl, S. Kreuzer, D. Weiss, G. Bayreuther, Epitaxial nanomagnets with intrinsic uniaxial in-plane magnetic anisotropy, Journal of Applied Physics, 87 (2000) 7016-7018.

[19] X. Zhong, N.N. Phuoc, W.T. Soh, C. Ong, L. Peng, L. Li, Tailoring the magnetic properties and thermal stability of FeSiAl-Al2O3 thin films fabricated by hybrid oblique gradient-composition

sputtering, Journal of Magnetism and Magnetic Materials, 429 (2017) 52-59.
[20] F. Tang, D.-L. Liu, D.-X. Ye, Y.-P. Zhao, T.-M. Lu, G.-C. Wang, A. Vijayaraghavan, Magnetic properties of Co nanocolumns fabricated by oblique-angle deposition, Journal of applied physics, 93 (2003) 4194-4200.
[21] J. Ma, X. Ni, J. Huang, J. Li, Effects of Dipolar Interaction on Magnetic Properties of Fe x (SiO2) 1− x Nanocomposites, Journal of nanoscience and nanotechnology, 10 (2010) 791-797.
[22] N. N. Jiang, Y. Yang, Y. X. Zhang, J. P. Zhou, P. Liu, C.-Y. Deng, Influence of zinc concentration on structure, complex permittivity and permeability of Ni–Zn ferrites at high frequency, Journal of Magnetism and Magnetic Materials, 401 (2016) 370-377.
[23] N. Borhan, K. Gheisari, Structural and magnetic properties of nanocrystalline lithium–zinc ferrite synthesized by microwave-induced glycine–nitrate process, Journal of Superconductivity and Novel Magnetism, 27 (2014) 1483-1490.

JMATPRO	Journal of Advanced Materials and Processing 10 (2): 19-28, Spring 2022 http://jmatpro.iaun.ac.ir 20.1001.1.2322388.2022.10.2.3.8

Research Paper

Mechanical Behavior of the Copper Matrix Composite Reinforced by Steel Particles

Vahid Norouzifard[1*], Ashkan Nazari Siahpoush[2], Amir Talebi[3]

1. Department of Mechanical Engineering, Jundi-shapur University of Technology, Dezful, Iran

2. Department of Materials and Metallurgy Engineering, Islamic Azad University-Dezful baranch, Dezful, Iran

3. Faculty of Materials & Manufacturing Technologies, Malek Ashtar University of Technology, Tehran, Iran

ARTICLE INFO

Article history:

Received 19 October 2021
Accepted 23 December 2021
Available online 1 April 2022

Keywords:
Composite
Copper
steel particles
microstructure
fatigue test

ABSTRACT

In this study, the microstructure, tensile, and fatigue behavior of the copper matrix composites reinforced by steel particles are investigated. The composite grades containing 2.5, 5.2, and 7.4 wt% steel particles up to 90 µm in size are manufactured by the casting method. The microstructure of the composite samples is studied by scanning electron microscopy. The tensile and fatigue test samples are prepared and tested based on the ASTM standard. Adding 2.5 wt% steel particles to the copper matrix increases the yield strength, tensile strength, and elongation of the pure copper by about 48, 21, and 4.8%, respectively. The fatigue test results show that reinforcing the pure copper with 2.5 wt% steel particles improves the fatigue life of the pure copper by 67, 31, and 86 percent in 60, 80, and 100 MPa amplitude stresses, respectively. On the other hand, further increasing the reinforcement particle content to 5.2 and 7.4 wt% causes unusual fatigue behavior and adversely affects the mechanical strength of the composite. Therefore, the fatigue life of the composite samples reinforced by more than 5.2 wt% steel particles is not a function of the stress level and does not increase with the decrease of the stress.

Citation: Norouzifard, V.; Nazari Siahpoush, A.; Talebi, A. (2022). Mechanical Behavior of the Copper Matrix Composite Reinforced by Steel Particles, Journal of Advanced Materials and Processing, 10 (2), 19-28. Dor: 20.1001.1.2322388.2022.10.2.3.8

[*] **Corresponding Author**
E-mail Address: vnorouzi@jsu.ac.ir

1. Introduction

Pure copper is known as an essential material in several industries, such as electronics, mechanics, etc., because of its high electrical and thermal conductivity. Demand for high conductive and high strength materials have been increased in the electronic industries in recent years. Due to the low mechanical strength of pure copper, efforts to strengthen the copper have been conducted to get a proper composition of conductivity and high strength. To improve the mechanical properties of pure copper, several methods can be applied, such as; alloying, aging, and reinforcing. Alloying dramatically decreases the copper's electrical conductivity. Thus, alloying cannot be an efficient method to enhance the components made from pure copper in the electronic industry. Since the solid solution strengthening mechanism decreases the conductivity of the copper alloys, aging and precipitation hardening methods have become more popular for copper alloys. The aging process increases the strength of the copper alloy and keeps its conductivity relatively [1]. Reinforcing the pure copper by adding a harder material and producing a copper matrix composite is another way to enhance the mechanical properties of the pure copper without any serious adverse effect on the copper's electrical conductivity [2].

In this regard, a lot of research has been done to strengthen pure copper with various reinforcements. Ceramic particles such as SiC [3] and alumina [4] were the first materials used as reinforcement in copper matrix composites. But, due to the low wettability and adhesion of the ceramic particles with the copper matrix, the mechanical properties of the produced composite were not improved considerably rather to the pure copper properties. In some cases, reinforcing the copper with ceramic particles adversely affects the mechanical strength of the matrix [5]. Thus, to improve the mechanical strength of the copper composites reinforced by ceramic particles, additional processes have been used, such as the implantation of the metal coatings on the particles' surface. However, utilizing such coatings needs expensive and complicated processing technology [6, 7]. In recent years, carbon-based reinforcements such as carbon nanotubes [8] and graphene nano-plates [9-12] also have been considered to produce copper matrix composites. Mass production of relatively large components from the copper composites reinforced by carbon-based particles is difficult and expensive due to the production method of the composite, which is powder metallurgy.

The metallic reinforcements can be a good choice to improve the pure copper mechanical properties because of the following reasons; 1) the wettability of the metal particles in the copper melt is more than other ceramics or carbon-based materials, 2) the metal powders are more available and cheaper, and 3) finally the composites mass production is possible using the conventional production methods such as casting. Recently, Alaneme et al. [5] investigated the applicability and performance of mechanical strengthening of metallic reinforcements in metal matrix composites. Based on Alaneme et al. [5] review, there is considerable research in the open literature on which the metallic reinforcement used in aluminum and magnesium matrices. Sparse literature, however, exists on the use of metallic reinforcements for copper matrix. The available research about copper matrix composites reinforced by metallic particles is discussed by several studied.

Alaneme and Odoni [13] reinforced the pure copper using steel machining chips and investigated the mechanical properties, wear, and corrosion behavior of the produced composite. According to Alaneme and Odoni's [13] results, the steel particles as reinforcement improves pure copper's mechanical strength without any significant decrease in its toughness. Cardinal et al. [14] used Ta particles as reinforcement for a Cu-Zr-Al bulk metallic glass matrix. The composites having 5 to 50% of Ta particles in volume fraction were produced by the spark plasma sintering consolidation method. The mechanical tests showed that increasing the Ta particles increases the ductility and plasticity of the composite and decreases the yield stress. Hence, the authors, based on their investigations, concluded that the composite grade reinforced by 30% Ta particles in volume fraction was optimal for a good combination of hardness and ductility. Chen et al. [15] investigated the use of AlCoNiCrFe high entropy alloy (HEA) synthesized by mechanical alloying as reinforcement for a Cu matrix. The copper matrix composites reinforced by 10 to 20 wt% of the synthesized HEA were produced by powder metallurgy. The compression test results showed that the mechanical strength increases by increasing the reinforcement content. However, the ductility decreased by increasing the reinforcement's weight percent, and the unreinforced sample had the best ductility of all the samples tested. The best combination of ductility and strength belonged to the composite grade with 10 wt% of HEA reinforcements.

As above-mentioned literature review shows that there are a few studies that investigated the use of metallic particles as reinforcement to strengthen copper. Therefore, the present research makes an effort to fill this gap in the literature. In this study, following our previous research on the investigation of the properties of the copper matrix composites reinforced by steel particles [16], the tensile and fatigue behavior of the copper matrix composites reinforced by 2.5, 5.2, and 7.4 wt% steel particles

with spherical shape and maximum size of 90 μm are investigated. The steel particles were produced from machining chips. Disc mill and ball mill machines were used to change the machining chips' shape and size. The mechanical tests and sample preparation were done based on the ASTM standard. The fracture surface and microstructure of the fabricated composite are studied using optical microscopy and scanning electron microscopy, respectively.

2. Materials and experiments

2.1. Materials

The composite samples in this research were composed of pure copper, 99.9 %, as the matrix, and AISI 430 stainless steel as reinforcement particles. The chemical composition of the steel particles is listed in Table 1. The chemical composition of the steel and the copper were measured by emission spectrometry.

Table 1. Chemical composition of the reinforcement particles.

Element	Sn	Pb	W	V	Ni	Cr	S	P	C	Fe
Content (wt%)	0.00075	0.0024	0.0016	0.23	0.0041	15.34	0.0214	0.015	0.085	Base

2.2. Powder and composite fabrication

As the steel particles and composite samples fabrication are described in [16], in this paper, the procedure is presented briefly. The steel machining chips were produced by turning the steel bars into a lathe machine. Then, a disc mill (RS 200) machine manufactured by Retsch Company was used to convert the refined steel chips to steel particles. The disc mill machine product was converted to steel particles with a maximum size of up to about 90 μm by a planetary ball mill machine (PM 400 by Retsch Company). Finally, the refined particles by a ball mill machine were fed to Retsch AS200 shaker's sieves with a mesh size of 90 μm to control the size of the particles.

The copper matrix composite samples were fabricated by casting method using a coreless induction furnace and a gas gun. 22 mm in diameter copper bars were charged in the furnace and kept for about 20 minutes to ensure to be melted completely. The steel particles were carried into the copper melt by hot argon gas using the gas gun. To produce the composite grades containing 2.5, 5.2, and 7.4 wt% of steel reinforcements, 52, 117, and 173 grams of steel powder were injected into 2080, 2125, and 2162 grams of copper melt, respectively. Pure copper samples also were cast by the same manufacturing process as the composites. The melt was poured into the casing molds cavity with the dimension of 60*140*12 mm. The molds were made of low-carbon steel and preheated at a temperature of 300 ^{o}C. To homogenize the microstructure of the samples, solidified composite samples were put for 1 h in a heat treatment furnace at a temperature of 850 ^{o}C.

2.3. Characterization

Mira 3-XMU field emission scanning electron microscope (FE-SEM) was used to investigate the microstructure of the produced composite and pure copper samples. The fatigue test was performed on a fatigue test machine manufactured by Schenck Trebel company based on the ASTM E466 standard [17]. The tensile properties of the composites were also assessed by a Schenck-Trebel testing machine at room temperature and a strain rate of 3×10^{-3} s^{-1} based on the ASTM E8/E8M standard [18]. The fatigue test fracture surface of the prepared composite specimens was also studied using an RZ-BD Meiji stereo microscope. Figure 1 shows the specification and dimensions of the tensile and fatigue tests' samples.

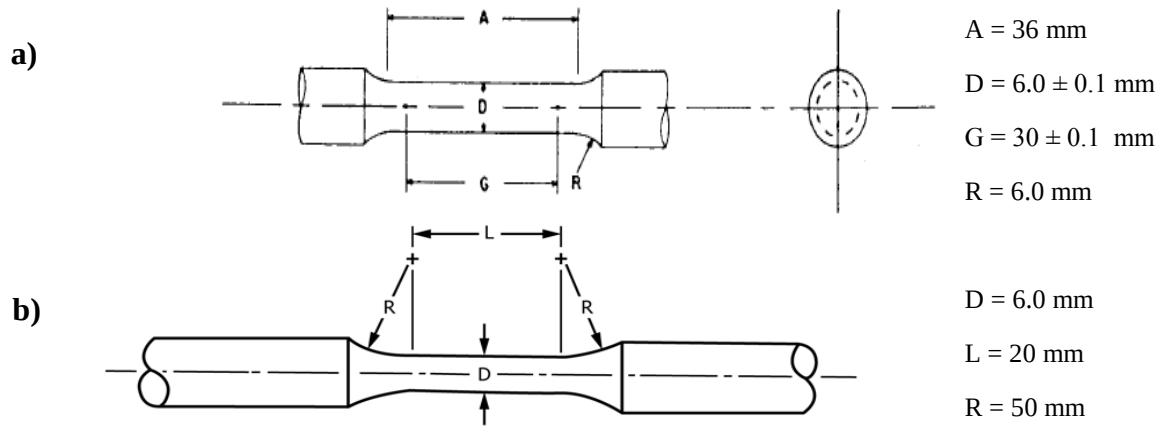

Fig. 1. Specification and dimensions of a) the tensile test and b) the fatigue test samples.

3. Results and discussion

3.1. Microstructure of the composite

Figure 2a shows the SEM micrograph of the microstructure of the composite grade containing 2.5 wt% steel particles. In the present SEM micrographs, the dark and light areas refer to the matrix and reinforcement particles, respectively. Figure 2b shows the composite microstructure in 20000x magnification, and very few small particles can hardly be seen due to the low content of the reinforcements in the composite.

Figures 2b shows the SEM micrograph of the copper matrix composite reinforced by 5.2 wt% steel particles with a magnification of 20000x. In Figure 2b, more particles are seen than in Figure 2a because of the more particle content. The microstructure of the composite grade reinforced by 7.4 wt% steel particles is also shown in Figure 2c. Unlike the previous figures, the steel particles can be seen easily in large numbers. Comparing Figures 2a, b, and c also shows the reinforcement particle content increasing in the composite grades.

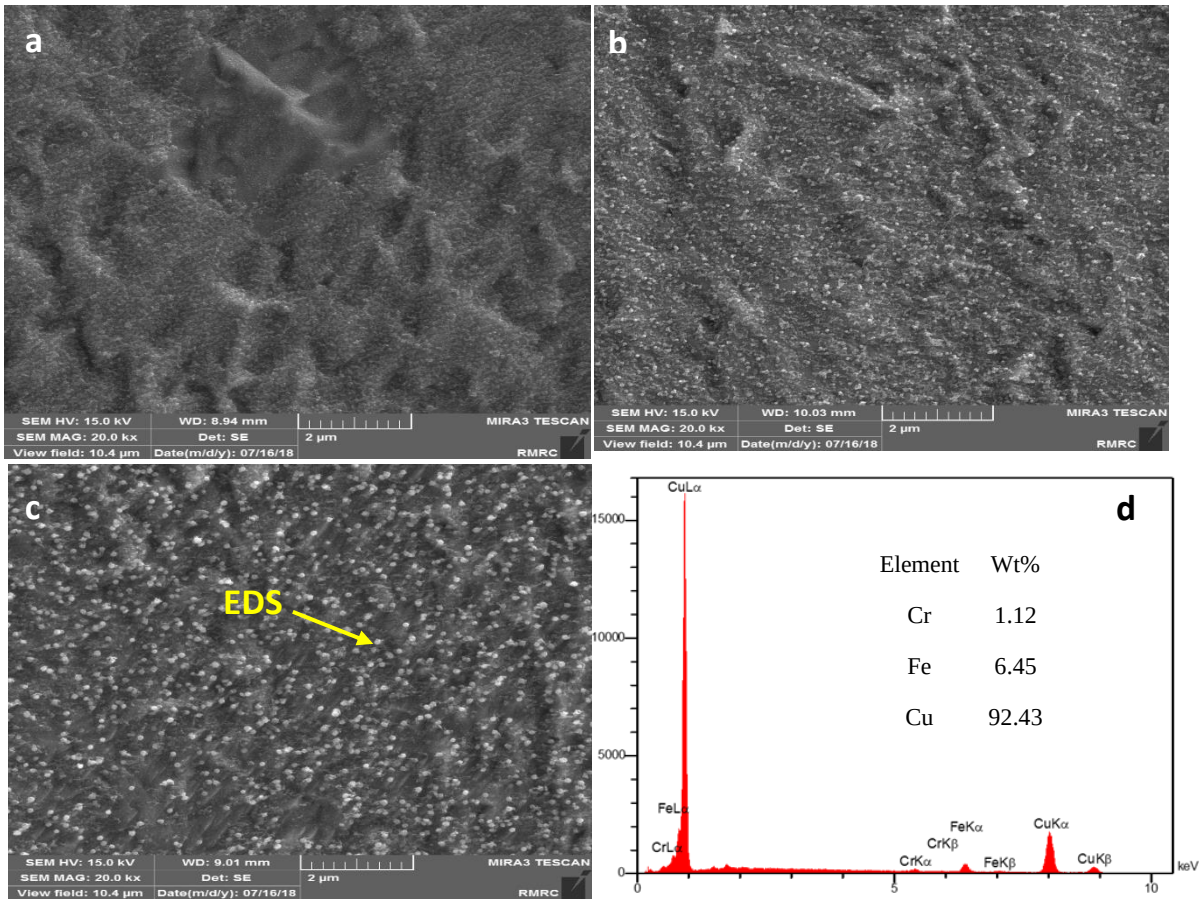

Fig. 2. SEM micrograph of copper matrix composite reinforced by a) 2.5, b) 5.2, and c) 7.4 wt% steel particles by a magnification of 20000x, and d) EDS analysis results for the composite grade reinforced by 7.4 wt% particles (region shown in c).

Figure 2d shows the EDS analysis of the region shown by an arrow in Figure 2c. The EDS graph shows Copper (Cu), iron (Fe), and chromium (Cr) peaks. These elements are the dominant elements of the matrix and reinforcement materials and agree with the steel particles' chemical composition listed in Table 1. Also, the absence of the oxygen peak in the EDS analysis results reveals that oxidation did not occur in the composite matrix and the steel particles during the manufacturing procedure.

Figure 3 shows the X-ray diffraction (XRD) analysis result of the composite grade reinforced with 7.4 wt% of steel particles. The XRD pattern only shows the profile of the copper and the steel particles' profiles are not visible due to the low volume fraction and dispersion of the particles. Similar XRD results are available in the literature that the reinforcement particles are not detected in metal matrix composite due to the low particle content. For example, Bagheri [19] investigated the copper matrix/TiC particles composite, and all TiC peaks have not been detected in the XRD results of the composites reinforced with lower than 20 vol% of TiC particles.

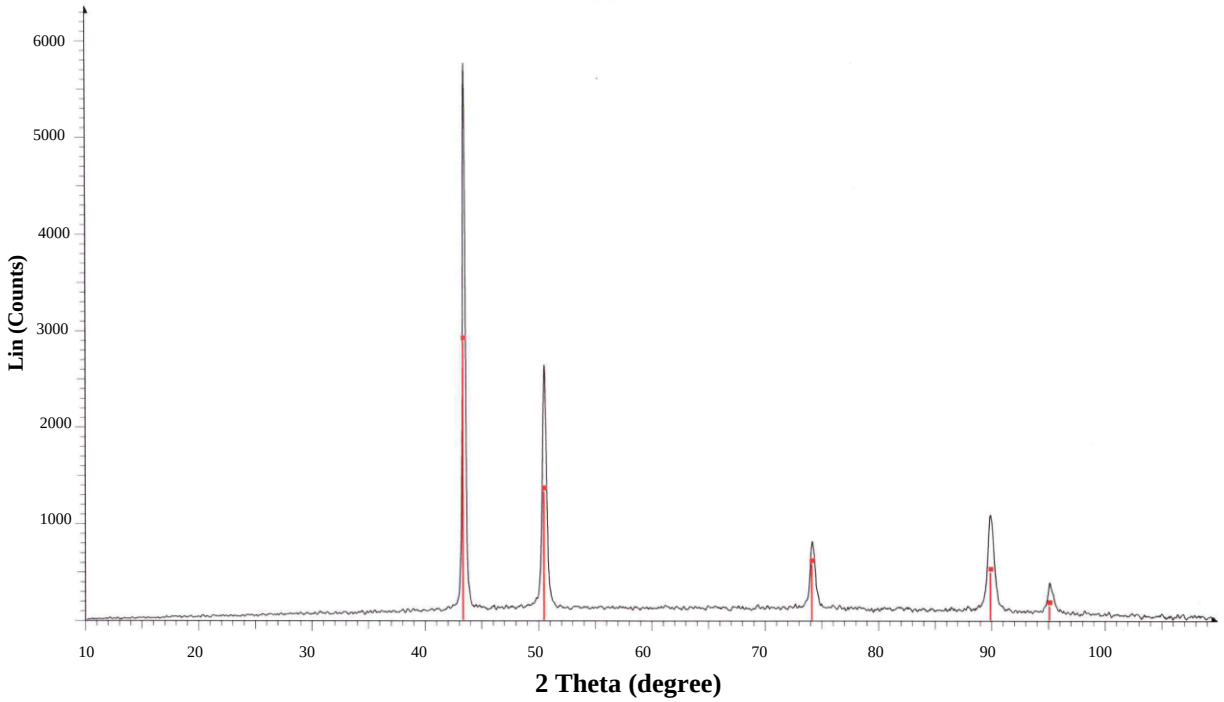

Fig. 3. XRD profile of the copper matrix composite with 7.4 wt% of steel particles

3.2. Tensile and fatigue properties

The tensile properties and fatigue test results in the reversing stresses of 60, 80, and 100 MPa for the composites and the pure copper samples are summarized in Table 2. According to the fatigue test results, the composite grade with 2.5 wt% steel particles has maximum fatigue life at 60 and 100 MPa loading, but at 80 MPa, the composite reinforced by 5.2 wt% has the longest life. The stress-strain diagrams of the composite grades and pure copper samples are shown in Figure 4. The composite grade with 2.5 wt% steel particles has the highest yield and tensile strength among the composite grades and pure copper samples. Based on the tensile test results, adding 2.5 wt% steel particles to pure copper enhances copper's yield and tensile strength by about 48 and 21%, respectively. However, the elongation of the composite grades increases gradually by increasing the steel particles content.

Several strengthening mechanisms describe the reinforcement particles' contribution to the composite strength enhancement, such as the Orowan mechanism, coefficient of thermal expansion mismatch, and load-bearing effect [16]. Distance between particles and difference between the reinforcement particles and matrix thermal expansion coefficients and particles' size, shape, and volume fraction are the main parameters that affect the strengthening of the composite. Therefore, when the particles' volume fraction increases, the distance between the particles decreases. Increasing the volume fraction and decreasing the particles' distance positively affect the mechanical strength of the composite. But, increasing the particle content increases the possibility of the particles' agglomeration in the matrix. When the reinforcement content passes a critical value, the particles' agglomeration adversely affects the matrix/reinforcement bonding, and also the unreinforced matrix regions increase. Therefore, the yield and tensile strengths of the composite deteriorate when the reinforcement volume fraction or weight percent passes the critical value. Thus, the low mechanical strength of the composite grades with 5.2 and 7.4 wt% steel particles in comparison with the composite reinforced with 2.5 wt% particles can be justified accordingly. Increasing the composite samples' elongation by increasing the particle content can be explained as follows. When in the copper matrix, a crack meets reinforcement particles, either the particle should be split, or the crack should turn around the particle to pass. But fracture can occur in brittle reinforcements like ceramic particles. Therefore, it seems that in the present composites, the steel particles prevent crack propagation in the matrix. Thus, the ductility of the composite grades increases continuously by increasing the reinforcement particle content.

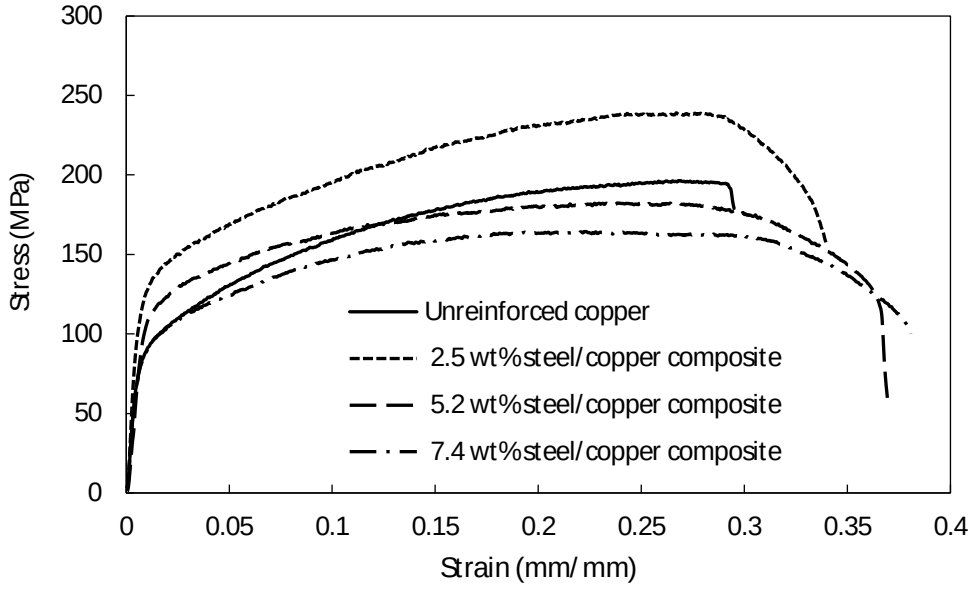

Fig. 4. Stress-strain diagrams of the composite grades reinforced by 2.5, 5.2, and 7.4 wt% steel particles and unreinforced pure copper.

Table 2. The tensile properties and fatigue test results in the reversing stresses of 60, 80, and 100 MPa.

Sample composition	Fatigue life at 100 MPa (cycles)	Fatigue life at 80 MPa (cycles)	Fatigue life at 60 MPa (cycles)	Yield strength (MPa)	Tensile strength (MPa)	Elongation (%)
Pure copper	102600	436050	8071200	81	198	31.5
Copper- 2.5 wt% steel particles	171000	572850	15065100	120	238	33
Copper- 5.2 wt% steel particles	116850	3437100	3659400	110	185	34
Copper- 7.4 wt% steel particles	142500	632700	615600	83	163	35.5

Figure 5 shows the stress-fatigue life (S-N) diagrams of the pure copper and the copper-2.5 wt% steel particles composite. Both diagrams shown in Figure 5 are similar to the nonferrous metals fatigue diagrams in which the curve slope changes and decreases when the fatigue life passes one million cycles. The stress ranges corresponding to one million cycles are 75 and 77 MPa for the pure copper and the composite grade reinforced by 2.5 wt% particles, respectively. The mentioned stress ranges are about 37 and 32 percent of the pure copper and the composite tensile strength.

Figure 6 shows the stress-fatigue life (S-N) diagrams of the pure copper and the copper composites containing 5.2 and 7.4 wt% steel particles. Comparing figures 5 and 6 shows that the copper matrix composites with high content of steel particles present unconventional fatigue behavior. As seen in Figure 6, the fatigue life of the composites reinforced by 5.2 and 7.4 wt% remains at the same level when the stress range decreases from 80 to 60 MPa. While, the fatigue life of the pure copper and the copper-2.5 wt% steel particles composite increases by decreasing the stress range from 80 to 60 MPa, like most pure metals and alloys.

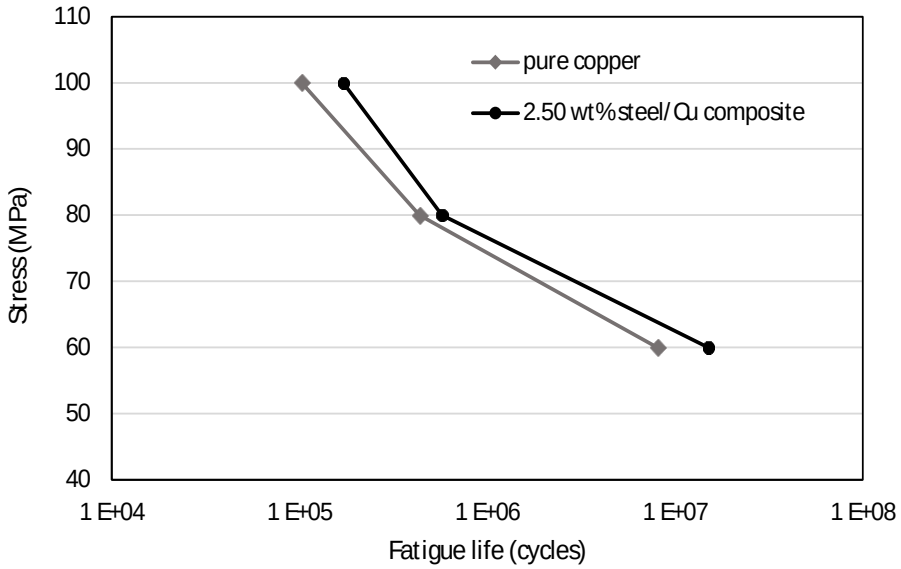

Fig. 5. Strength versus fatigue life diagrams of the pure copper and copper-2.5 wt% steel particles.

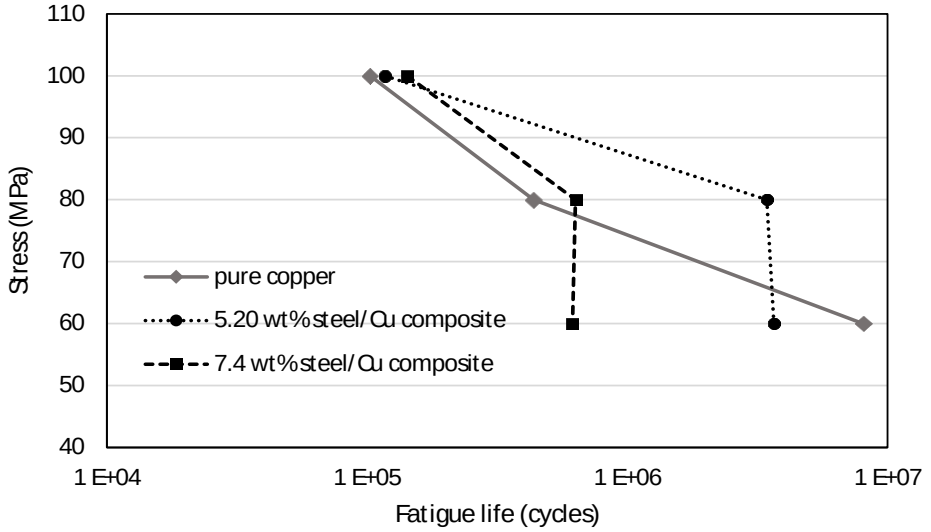

Fig. 6. Strength versus fatigue life diagrams of the pure copper and the composite grades with 5.2 and 7.4 wt% steel particles.

Fatigue failure has three stages; crack initiation, crack growth, and final ultimate failure. Decreasing the stress range increases the stress cycles required for crack initiation and growth. Therefore, the fatigue life increases by decreasing the stress level in the pure copper and the copper-2.5 wt% steel composite. On the other hand, when the content of the reinforcing particles in the composite increases, as mentioned, the possibility of the steel particles' agglomeration increases. The agglomeration of the reinforcement particles weakens the matrix/reinforcement bonding, enhances the possibility of microcracks creation in the composite structure, and adversely affects the composite yield and tensile strengths, as seen in the tensile test results listed in Table 2. Therefore, to explain the abnormal fatigue behavior of the present composites reinforced by 5.2 and 7.4 wt% steel particles, two reasons can be mentioned; 1) decreasing the loading cycles required to fatigue crack nucleation and crack growth due to the existence of the micro-cracks in the composite structure, and 2) the low mechanical strength of the composite.

3.3. Fatigue samples fractography

Figure 7 shows the fatigue fracture surfaces of the pure copper and the produced composites. According to Figure 7, the fatigue fracture surfaces have two recognizable zones the first one is light and glossy, and the last is rough and dark. The first and second zones represent the crack initiation and crack growth zone and the final fracture zone, respectively. In the fracture surface of the pure copper sample, the rough surface that refers to the final fracture is small than the rest of the total surface, which is for the crack initiation and growth zone, as shown in Figure 7a.

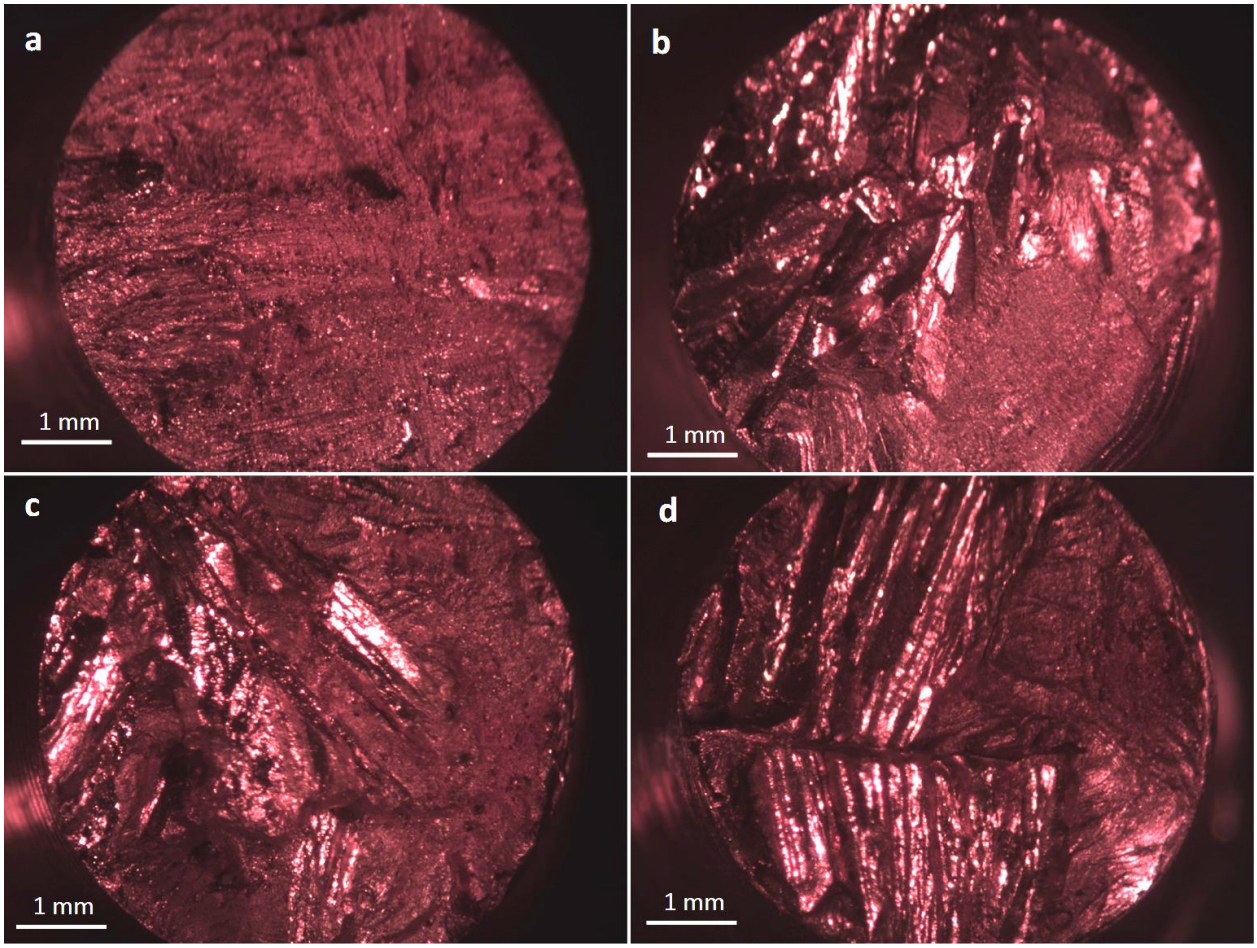

Fig. 7. The fatigue failure surface of (a) the pure copper and the composite grade reinforced with (b) 2.5, (b) 5.2, and (c) 7.4 wt% steel particles.

Figure 7b shows the fracture surface of the composite grade with 2.5 wt% steel particles. As seen, the crack growth zone is glossier than the pure copper fracture surface. The gloss of the fracture surface can be related to the shear plastic deformation of the crack tip in the crack proportion area. It means that adding the steel particles to the pure copper blocks the crack growth pass and causes more shear plastic deformation in the crack growth area. The irregular patterns in the crack growth zone of the copper-2.5 wt% steel particles fracture surface also reveal the fact that the steel particles changed the crack pass.

The fracture surface of the composite grade reinforced by 5.2 wt% steel particles is shown in Figure 7c. The glossy surface is also seen at this grade, but several dimples are also seen at the fracture surface. Dimples can be the result of the steel particles' agglomeration. In the particles' agglomeration regions, the agglomerated particles compose a hardcore that is surrounded by the soft unreinforced matrix material. Therefore, during the fatigue loading, a microcrack can be created in the core, but the soft and ductile matrix surrounds it, and its propagation pass is blocked. As a result, the matrix experiences shear stresses, and its final fracture develops a dimple [20, 21]. In addition, dimples are also seen in the final fracture area.

Figure 7d shows the fracture surface of the composite grade reinforced by 7.4 wt% steel particles. Wavy patterns in the glossy region can relate to the crack edge plastic strain and the growth of cyclic crack fatigue [22, 23]. In the composite grade with 7.4 wt% steel particles, unlike the other grades, the glossy region patterns are parallel lines with large distances that reveals faster crack growth in this region.

4. Conclusions

This paper investigates the microstructure, tensile properties, and fatigue behavior of the copper matrix composite reinforced by the processed steel particles from steel machining chips and achieves the following conclusion.

1. The SEM micrographs of the produced composites microstructure and the EDS analysis results confirm the steel particles' presence and absence of oxidation.
2. Adding 2.5 wt% steel particles as the reinforcement to the copper matrix increases the yield strength, tensile strength, and elongation of the pure copper by about 48, 21, and 5%, respectively. Increasing the steel particle content in the matrix to 5.2 and 7.4 wt% decreases the yield and tensile

strengths of the composite. The elongation, however, increases continuously by increasing the reinforcement particles' weight percent.

3. The fatigue test results show that by adding 2.5 wt% steel particles to the pure copper, the fatigue life of the pure copper increases by 67, 31, and 86 percent in 60, 80, and 100 MPa amplitude stresses, respectively. Further increasing reinforcement particle content to 7.4 wt% causes unconventional fatigue behavior in the composites as by decreasing stress range from a specific level (80 MPa for the present composites), the fatigue life does not increase. This unusual behavior can be the result of non-uniform distribution and agglomeration of the steel particles in the matrix, which facilitate crack initiation and decrease the mechanical strength of the composite.

Therefore, according to the above-mentioned results, it can be concluded that reinforcing copper matrix with the proper weight percent of steel particles improves not only the mechanical strength but also the elongation, ductility, and fatigue life of the copper.

References

[1] S. Fu et al., "Effect of aging process on the microstructure and properties of Cu–Cr–Ti alloy," Mater. Sci. Eng. A, vol. 802, 2021, p. 140598.

[2] X. Gao et al., "Mechanical properties and thermal conductivity of graphene reinforced copper matrix composites," Powder Technol., vol. 301, 2016, pp. 601–607.

[3] N. Somani, Y. K. Tyagi, P. Kumar, V. Srivastava, and H. Bhowmick, "Enhanced tribological properties of SiC reinforced copper metal matrix composites," Mater. Res. Express, vol. 6, no. 1, 2018, p. 016549.

[4] R. kumar L and A. K. S, "Corrosion and wear behaviour of nano Al2O3 reinforced copper metal matrix composites synthesized by high energy ball milling," Part. Sci. Technol., vol. 38, no. 2, 2020, pp. 228–235.

[5] K. K. Alaneme, E. A. Okotete, A. V. Fajemisin, and M. O. Bodunrin, "Applicability of metallic reinforcements for mechanical performance enhancement in metal matrix composites: a review," Arab J. Basic Appl. Sci., vol. 26, no. 1, 2019, pp. 311–330.

[6] A. Brendel, C. Popescu, H. Schurmann, and H. Bolt, "Interface modification of SiC-fibre/copper matrix composites by applying a titanium interlayer," Surf. Coatings Technol., vol. 200, no. 1-4, 2005, pp. 161–164.

[7]T. Köck, A. Brendel, and H. Bolt, "Interface reactions between silicon carbide and interlayers in silicon carbide-copper metal-matrix composites," J. Nucl. Mater., vol. 362, no. 2–3, 2007, pp. 197–201.

[8] M. Abolghasem, A. Rashidi, S. M. Abbasi, and M. Mihanpanah, "Manufacture and mechanical properties study of copper-matrix nanocomposites reinforced with carbon nanotubes by means of powder metallurgy," emergencias, vol. 6, 2013, pp. 22–27.

[9] G. Shao, P. Liu, K. Zhang, W. Li, X. Chen, and F. Ma, "Mechanical properties of graphene nanoplates reinforced copper matrix composites prepared by electrostatic self-assembly and spark plasma sintering," Mater. Sci. Eng. A, vol. 739, no. August 2018, 2019, pp. 329–334.

[10]C. Salvo, R. V. Mangalaraja, R. Udayabashkar, M. Lopez, and C. Aguilar, "Enhanced mechanical and electrical properties of novel graphene reinforced copper matrix composites," J. Alloys Compd., vol. 777, 2019, pp. 309–316.

[11] K. Zhang, G. Shao, W. Li, X. Chen, F. Ma, and P. Liu, "Wear and Corrosion Behavior of Graphene-Nanoplate-Reinforced Copper Matrix Composites Prepared Through Electrostatic Self-Assembly," J. Mater. Eng. Perform., vol. 28, no. 3, 2019, pp. 1650–1660.

[12] N. Vijay Ponraj, A. Azhagurajan, S. C. Vettivel, X. Sahaya Shajan, and P. Y. Nabhiraj, "Study of Processing and Microstructure of Copper Composite Reinforced with Graphene Nanosheet by Powder Metallurgy Technique," Powder Metall. Met. Ceram., vol. 56, no. 9–10, 2018, pp. 523–534.

[13] K. K. Alaneme and B. U. Odoni, "Mechanical properties, wear and corrosion behavior of copper matrix composites reinforced with steel machining chips," Eng. Sci. Technol. an Int. J., vol. 19, no. 3, 2016, pp. 1593–1599.

[14] S. Cardinal, J. M. Pelletier, G. Q. Xie, F. Mercier, and F. Dalmas, "Enhanced compressive plasticity in a Cu-Zr-Al – Based metallic glass composite," J. Alloys Compd., vol. 782, 2019, pp. 59–68.

[15] J. Chen et al., "Fabrication and mechanical properties of AlCoNiCrFe high-entropy alloy particle reinforced Cu matrix composites," J. Alloys Compd., vol. 649, 2015, pp. 630–634.

[16] V. Norouzifard, H. Naeinzadeh, and A. Talebi, "Fabrication and investigation of mechanical properties of copper matrix nanocomposite reinforced by steel particle," J. Alloys Compd., vol. 887, 2021, p. 161434.

[17] Annual Book of ASTM Standards. E 466, 2016.

[18] Annual Book of ASTM Standards. E8/E8M, 2016.

[19] G. H. A. Bagheri, "The effect of reinforcement percentages on properties of copper matrix composites reinforced with TiC particles," J. Alloys Compd., vol. 676, 2016, pp. 120–126.

[20] D. Hull, Fractography: Observing, Measuring

and Interpreting the Fracture Surface Topography. Cambridge: Cambridge University Press, 1999.
[21] H. ASM, Volume 12: fractography. ASM international, 1987.
[22] A. Echeverría and J. M. Rodriguez-Ibabe, "The role of grain size in brittle particle induced fracture of steels," Mater. Sci. Eng. A, vol. 346, no. 1–2, 2003, pp. 149–158.
[23] N. Chawla and K. K. Chawla, Metal Matrix Composites. Springer, 2006.

JMATPRO	Journal of Advanced Materials and Processing 10 (2): 29-38, Spring 2022 http://jmatpro.iaun.iau.ir 20.1001.1.2322388.2022.10.2.4.9

Research Paper

Influence of Withdrawal Rate on As-Cast Microstructure and Stress-Rupture Life of Directionally Solidified Rene80 Superalloy

Sobhan Rajabinejad, Masumeh Seifollahi*, Seyed Mahdi Abbasi, Seyed Mahdi Ghazi mirsaeed

Faculty of Materials and Manufacturing Technologies, Malek Ashtar University of Technology, Tehran, Iran.

ARTICLE INFO

Article history:

Received 11 January 2022
Accepted 26 March 2022
Available online 1 April 2022

Keywords:
Rene80
DS superaloy
Withdrawal rate
Dendritic structure
Microporosity
Stress-rupture

ABSTRACT

The purpose of this study is to investigate the effects of withdrawal rate on the dendrite microstructure and its formation mechanism, the porosity, and the interaction between them in Rene 80 superalloy. So, Rene 80 Ni-base superalloy was directionally solidified on a laboratory scale using the Bridgman method. The cylindrical rods were grown at withdrawal rates of 2, 4, 6, 8, and 10 $mm.min^{-1}$. Dendritic structure and solidification microporosities were evaluated in transverse and longitude sections. The results showed that when the withdrawal rate was increased, the primary and secondary dendritic arm spacing decreased. With an increasing withdrawal rate, which causes to decrease in the dendritic arms spacing, the volume fraction of inter-dendritic gamma prime was first decreased until the rate of 6 $mm.min^{-1}$, and after that, its volume fraction increased. This structure results from peritectic and eutectic transformations with checkerboard-like and fan-like morphology, respectively. Moreover, the volume fraction of microporosities was minimal at the rate of 6 $mm.min^{-1}$, while their average size decreased from 13.2 to 8.7 µm. The specimens were given a two-stage heat treatment followed by a stress rupture test at 191 MPa and 980˚C. It was shown that at R=6 $mm.min^{-1}$, directionally solidified rods with a less solidification microporosity and well-orientated dendritic structure give higher rupture life of 25.43 hrs.

Citation: Rajabinejad, S.; Seifollahi, M.; Abbasi, S.M.; Ghazi mirsaeed, S.M. (2022). Influence of Withdrawal Rate on As-Cast Microstructure and Stress-Rupture Life of Directionally Solidified Rene80 Superalloy, Journal of Advanced Materials and Processing, 10 (2), 29-38. Dor: 20.1001.1.2322388.2022.10.2.4.9

* **Corresponding Author**
E-mail Address: m_seifollahi@alumni.iust.ac.ir

1. Introduction

The high-temperature properties of nickel-base superalloys lead to their extensive application in jet engines and gas turbines [1]. Due to a good combination of tensile and stress rupture strength, long-term thermal stability, thermal fatigue, and hot corrosion resistance, the cast Rene80 Ni-base superalloy has been used extensively as the first and second stages of jet engine blades [2-6]. Work by Ohtomo et al. [3] demonstrated that tensile properties and rupture life of Rene 80 superalloy could be improved 10-15% and 2-3 times, respectively by directional solidification process. During the process of solidification, the porosities could form inevitably, which are difficult to be compensated by the interdendritic liquid flow. Undoubtedly, these porosities seriously deteriorate the high-temperature mechanical, especially fatigue properties of turbine blades [7-9]. Microporosities are classified into four groups: gas, solidification (S-type), heat treatment (H-type), and deformation (D-type). The gas porosity is generally spherical and has a very fine dimension compared to other porosities [9]. Anton [3] believed that the low solubility of a gas in Ni-based superalloys and the vacuum melting could minimize the formation of gas porosities. The S-type forms at the final stage of solidification in the interdendritic regions [9, 10]. The H-type grows during solution heat treatment and forms due to the diffusion of vacancies during homogenization. The D-type forms by creep deformation with the diffusion mechanism [11]. The S-type porosities are mainly located at the interdendritic areas, so there is a relationship between the dendrite arm spacing and porosity distribution. It is well known that the formation of porosity mainly depends on the thermal gradient, withdrawal rate, and shrinkage factor of the alloy. Actually, Bachalet [12] proposed that there might be an optimum withdrawal rate for a certain alloy and casting, which resulted in the closely spaced dendrite arms and a minimum level of porosity. For example, an optimum withdrawal rate of 3–6 $mm.min^{-1}$ was found in directional solidified columnar castings of Mar-M247 alloy [13]. For a third-generation Ni-based single crystal superalloy an optimized withdrawal rate was found as about 7.5 $mm.min^{-1}$.
Although a great deal of research has been done on the relation between withdrawal rate and dendritic microstructure of directional solidified and single crystal superalloys [14-17], but there were few studies on the influence of withdrawal rate on the solidification microstructures and stress rupture properties for the Rene 80 superalloy. Therefore, the purpose of this paper was to investigate the effects of the withdrawal rate on the dendrite microstructure, the porosity, and the interaction between them. Furthermore, the formation mechanism of the dendritic structure was also discussed, and the stress rupture life of the alloy was determined.

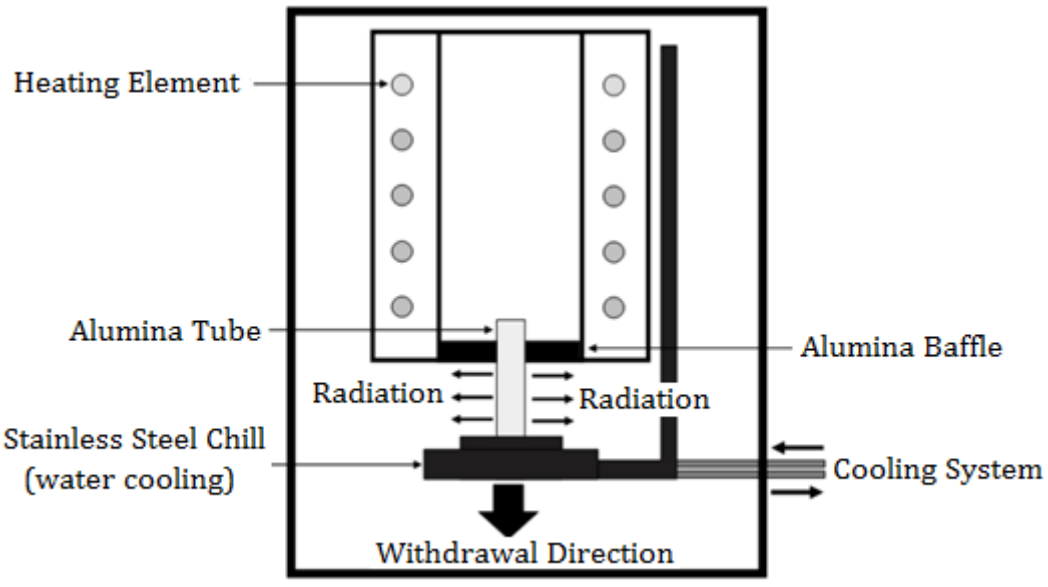

Fig. 1. Schematic representation of crystal growth system.

2. Experimental

Directionally solidified (DS) rods of Rene 80 superalloy with the standard composition 14Cr–9.5Co–5Ti–3Al–4W–4Mo–0.16C–0.015B–0.03Zr (wt.%) were prepared from 15 mm dia. cast ingots as a raw material. For this purpose, the raw material was melted and cast into five cylindrical ceramic tubes of 15 mm dia. and 140 mm height using vacuum induction melting (VIM) furnace. The furnace was evacuated to 10-3 Pa and purged with high-purity Argon. The temperature of the VIM furnace is controlled by adjusting the electric current and

power. The power of the furnace is 75 KW. These polycrystalline rods were directionally solidified in alumina tubes with the mentioned dimensions using a Bridgman crystal growth system with water-cooled steel chills. A schematic of the system is shown in Figure 1. The method involves heating polycrystalline above its melting point and slowly cooling it from one end where a steel-cooled chill crystal is located. The withdrawal rates of the directional solidification process were selected over a wide range, i.e., R=2, 4, 6, 8, and 10 mm.min^{-1}. The superheating temperature of the process was 1550˚C.

Metallographic sections were prepared using standard polishing procedures according to ASTM E3-01. The microstructure was revealed using a Marble solution. A VEGA TESCAN scanning electron microscope (SEM) with an energy dispersive spectroscopy (EDS) analyzer operating at 15KV and Olympus optical microscope (OM) were used to analyze the morphology and distribution of the phases. In addition, the Image J software was used to quantify and analyze the microstructure and measurement of primary dendritic arm spacing (PDAS) and secondary dendritic arm spacing (SDAS). The heat treatment schedule of Rene 80, according to the general procedure is consisted of 1024°C-2h (FC) + 1093°C-4h (FC) +1054°C-4h (FC), followed by aging at 873°C for16 h (AC). The cycles are drawn in Figure 2. The stress-rupture tests were carried out at 191 MPa and 980°C. The test was conducted according to ASTM E139. Schematic of the stress-rupture specimens is shown in Figure 2.

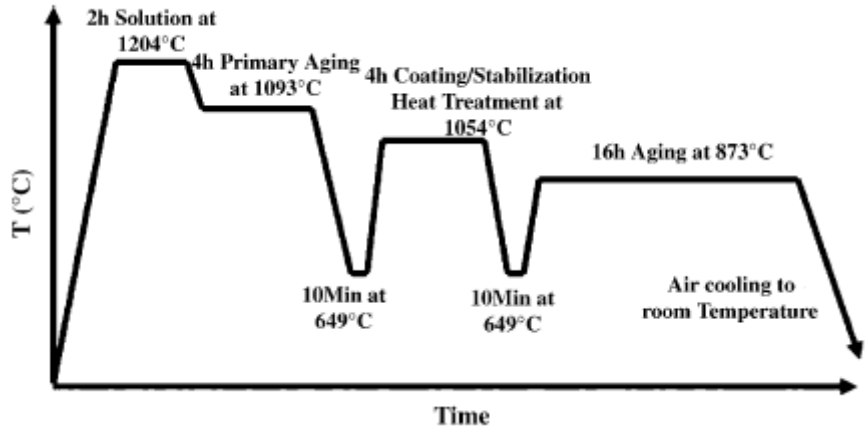

Fig. 2. Schematic of the heat treatment cycles of Rene 80 superalloy according to general electric standard.

3. Results and Discussion

3.1. Dendritic structure

Microstructural analysis of as-cast DS alloys under various withdrawal rates showed that up to the height of 20 mm from the chill plate, the melting was not completely achieved, and the alloy structure was not columnar (see Figure 3). This could be due to the high-temperature gradient in this zone as well as the inappropriate function of the baffle in this zone. As a result, the dendritic structure of the alloy was evaluated in three heights of 40, 60, and 80 mm of directionally solidified cylinder.

Based on the models presented for directionally solidified alloys growth including Hunt [18], Kurz-Fisher [19], and Trivedi [20], the relationship between PDAS and the growth rate of the solidification front (withdrawal rate) can be defined by Eq. 1. Kattamis and Flemings [21] also mentioned the relation between SDAS and growth rate as Eq. 2. The presented models deal with binary alloys. Therefore, due to the complexity of the chemical composition of DS superalloys, it is difficult to precisely predict the microstructure resulting from different solidification rates.

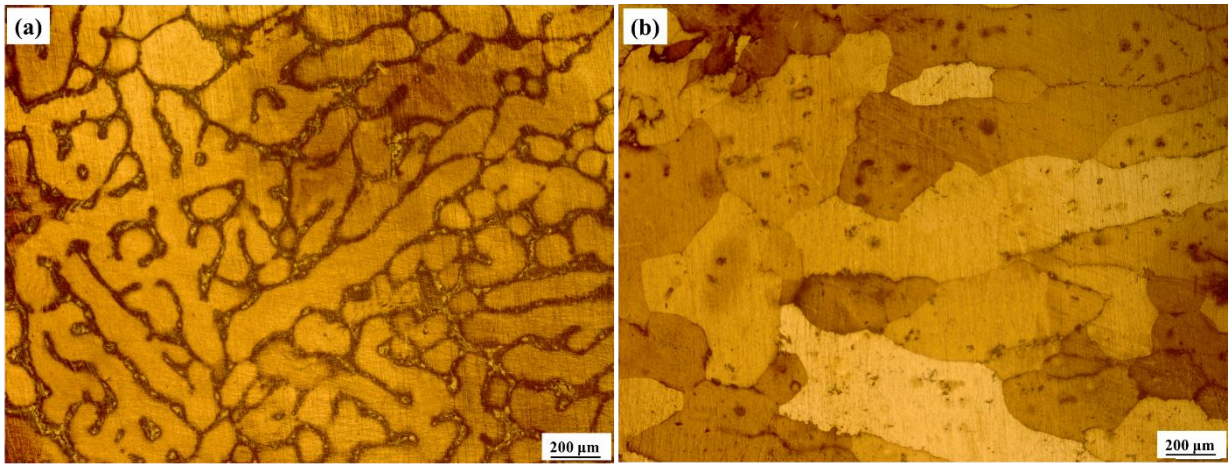

Fig. 3. Microstructure of the DS rods at the height 20 mm from the sill plate under withdrawal rates (a) 2 mm.min^{-1} and (b) 10 mm.min^{-1}.

(1) $\text{PDAS} \propto \text{R}^{-0.25}G^{-0.5}$ [18-20]

(2) $\text{SDAS} \propto \text{R}^{-\frac{1}{3}}$ [21]

Figures 4 and 5 show the longitude and transverse sections of dendritic structures of the directionally solidified specimens at the height of 60 mm. Moreover, the PDAS and SDAS as a function of withdrawal rate (R) and distance from the chill are depicted in Figure 6. As can be seen, an increase in withdrawal rate from 2 to 10 mm.min^{-1} resulted in a decrease of primary (PDAS) and secondary dendrite arm spacing (SDAS) from 293 and 89 m to 232 and 44 m, respectively. The results are compatible with Eq. 1 and 2, as with increasing withdrawal rate as well as increasing solidification rate, a finer dendritic structure was formed. Therefore, a reduction of PDAS and SDAS at high rates is expectable.

In all the specimens, by getting farther from the chill plate, PDAS showed an increase which may be attributed to temperature gradient loss in these zones [22]. An increase in the withdrawal rate caused to increase in the undercooling and which limits the growth of dendritic structure; hence, SDAS declined, similar to PDAS. Therefore, it is possible to change the solidification behavior of the alloys and hence alternate the slope of PDAS curve as a function of R. It seems that an increase in withdrawal rate will decrease the temperature gradient in the melted substance. Moreover, by getting farther from the chill plate, SDAS values increased, which may be attributed to the effect of temperature gradient decline in distances far away from the chill plate [22]. Therefore, the solidification time was increased, and primary and secondary dendrite arms will have a longer time for growth.

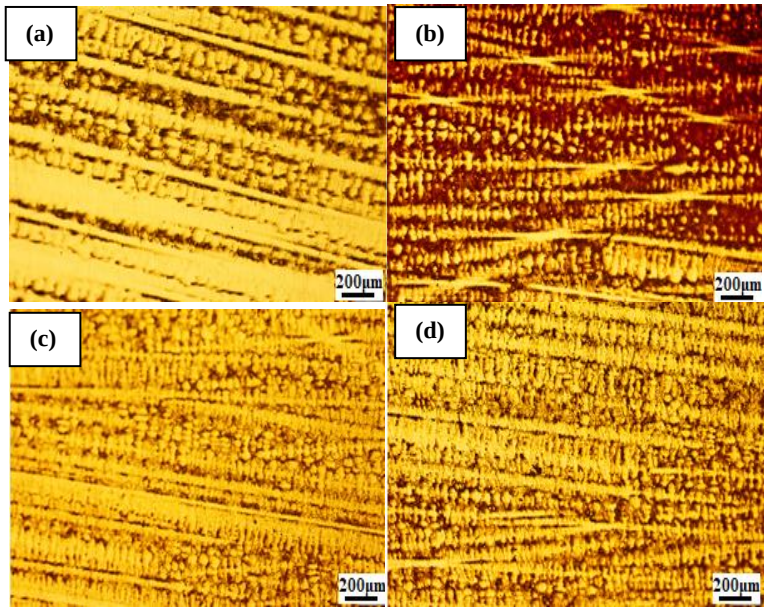

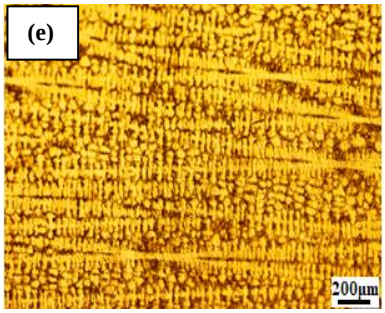

Fig. 4. Longitudinal sections of DS Rene80 rods at the height of 60 mm that directionally solidified under withdrawal rate of (a) 2; (b) 4; (c) 6; (d) 8 and (e) 10 mm.min^{-1}.

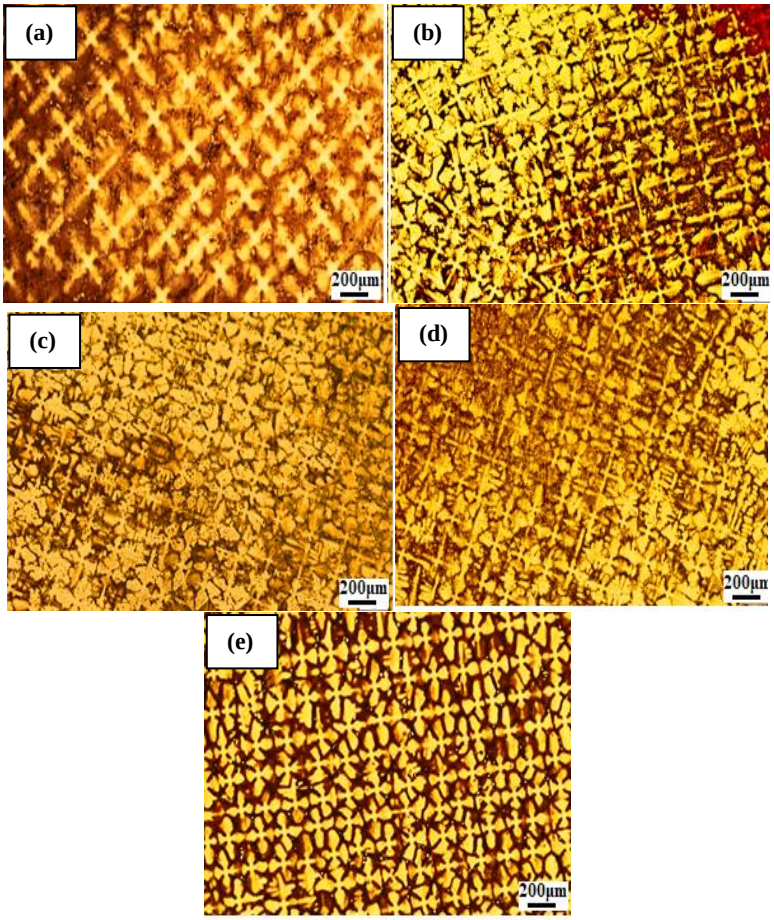

Fig. 5. Transverse sections of DS Rene80 rods at the height of 60 mm that directionally solidified under withdrawal rate of (a) 2; (b) 4; (c) 6; (d) 8 and (e) 10 mm.min^{-1}.

3.2. Microporosities

In the present study, microporosity refers to solidification porosity or S-type porosity formed as the result of the contraction of the final melt in interdendritic zones. Gas porosities are also possible. The probability of this type of porosity is low due to vacuum solidification. The distribution of the microporosities was evaluated by the graphs obtained at three heights of 40, 60, and 80 mm. Figure 7a and b represent the optical images of porosity distribution in DS specimens solidified at withdrawal rates of 2 and 10 mm.min^{-1}, respectively. One can see that, with an increasing solidification rate, a finer distribution of microporosities has been attained.

Figure 7c shows an S-type porosity in the vicinity of a eutectic island. It seems that the obtained porosity was formed in the last stage of solidification due to trapping and lack of melt feeding in this zone. Figure 8 illustrates the size, volume fraction, and number of porosities in terms of withdrawal rate. The porosities are quantified according to the E2109 ASTM standard. It was observed that an increase in withdrawal rate from 2 to 10 mm.min^{-1} decreased the size of microporosities from 13.2 to 8.7 µm.

Decreasing the dendritic arm spacing as a result of the withdrawal rate increasing causes to decrease in the pore's growth rate and hence declines their size. On the other hand, an increase of the withdrawal rate from 2 to 10 mm.min^{-1} increased the number of pores per section from 128 to 271. With the increase of the withdrawal rate and finer dendritic structure, the number of porosity germination sites increased. The major reason for the emergence of contraction microporosities is improper melt feeding in interdendritic regions. Therefore, when the dendritic structure gets finer, and the number of dendrites increases, the number of potential regions for contraction porosities formation will increase. On the other hand, enhancing the withdrawal rate from 2 to 6 mm.min^{-1} decreased the porosity from 0.26% to 0.15%. Further increase of withdrawal rate from 6 to 10 mm.min^{-1}, however increased the porosity percentage from 0.15% to 0.24%. Therefore, it can be said that the rate of 6 mm.min^{-1} is the optimum rate giving rise to the lowest porosity percentage in the as-cast structure. As it can be seen in Figure 9, there is a direct relationship between these parameters: finer dendritic structures will have smaller pores.

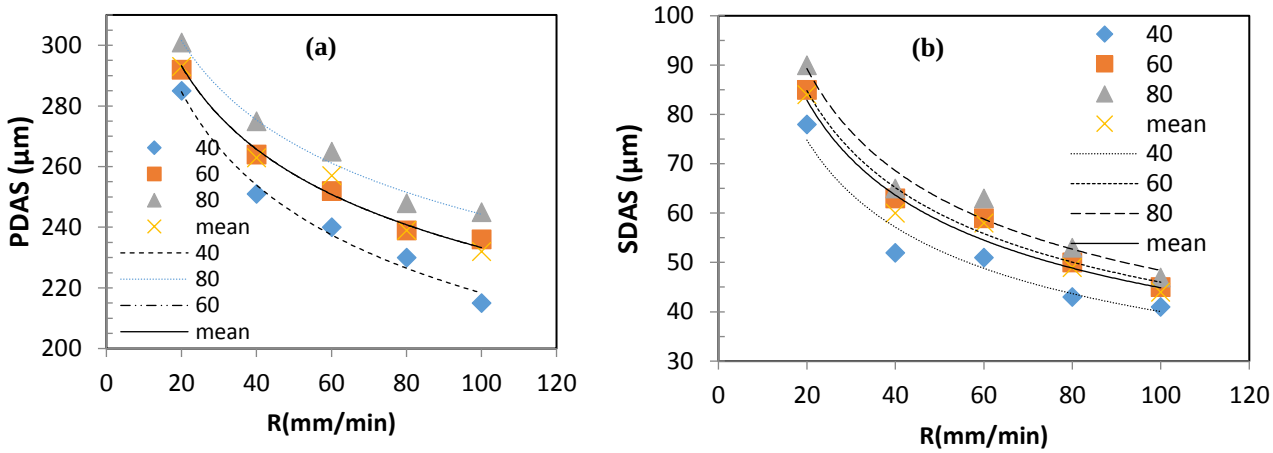

Fig. 6. (a) PDAS and (b) SDAS with withdrawal rate at different distances from the chill plate.

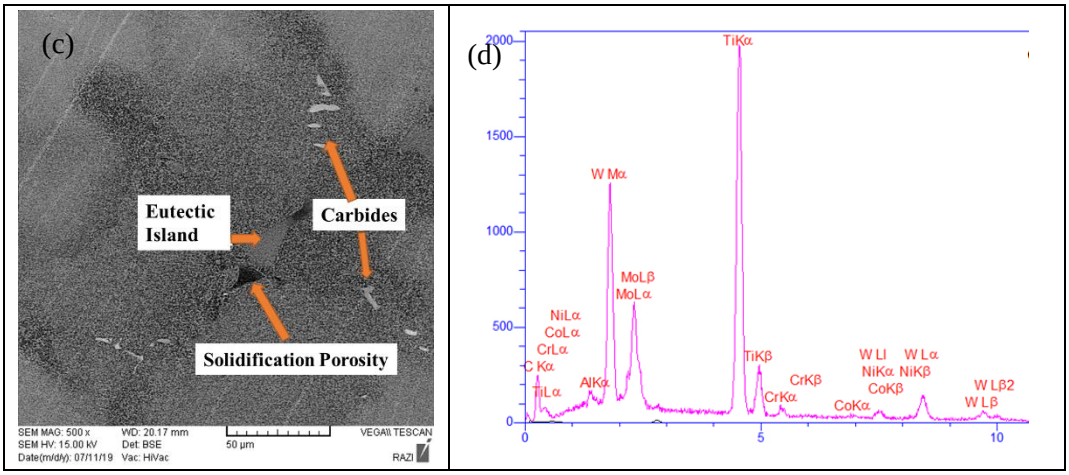

Fig. 7. Microporosities in DS Rene 80 rods that directionally solidified under withdrawal rates of (a) 2; (b) 10 mm.min^{-1}, and (c) the solidification microporosity at the adjacent of eutectic phase at 2 mm.min^{-1} and (d) EDS analysis of Carbide phase.

3.3. Eutectic Islands

Figure 9a and b show an optical image of eutectic islands in the specimens solidifies at 2 and 10 mm.min^{-1}, respectively. It can be seen that the eutectic structure is dependent on the dendritic structure. Due to the thermal gradient drop at 10 mm.min^{-1} growth rate, tertiary dendrite arms have been grown from the secondary ones. Therefore, a continuous network of the eutectic structure has been generated. As it is shown in Figure 10, with increasing withdrawal rate from 2 to 8 mm.min^{-1}, the eutectic volume percent has been decreased, while at 10 mm.min^{-1}, the eutectic volume percent has increased.

Figure 9c show the SEM image of a eutectic island in the specimen solidified at 8 mm.min^{-1}. This zone highly resembles the shape of a footprint; in a way that coarse γ' is like foot fingers, and fine ones along with γ' phase was also created while both sections are linked to a dendrite. Warnken [23] named them as

fan-like and checkerboard-like sections, respectively. There is a controversy on the formation of these structures. Early research proposed that fan-like structures were first formed, and then fine checkerboard-like structures were formed from the melt [24]. This is rarely possible as it requires ultrahigh supercooling and numerous nucleation sites in the final melt. Regarding the nature of γ ′nucleation in the solid phase, the hypothesis of the primary formation of checkerboard-like sections with high nucleation sites and then the emergence of fan-like regions from the final melt sounds more rational [25]. On the other hand, as one can see in Figure 9c, even in the checkerboard-like section (fine), eutectic islands with distinct boundaries were formed. Hence, it seems that the mechanism of checkerboard-like section formation is something between the formation of γ' precipitates in the solid phase (ordering) and melt-to-solid eutectic transformation.

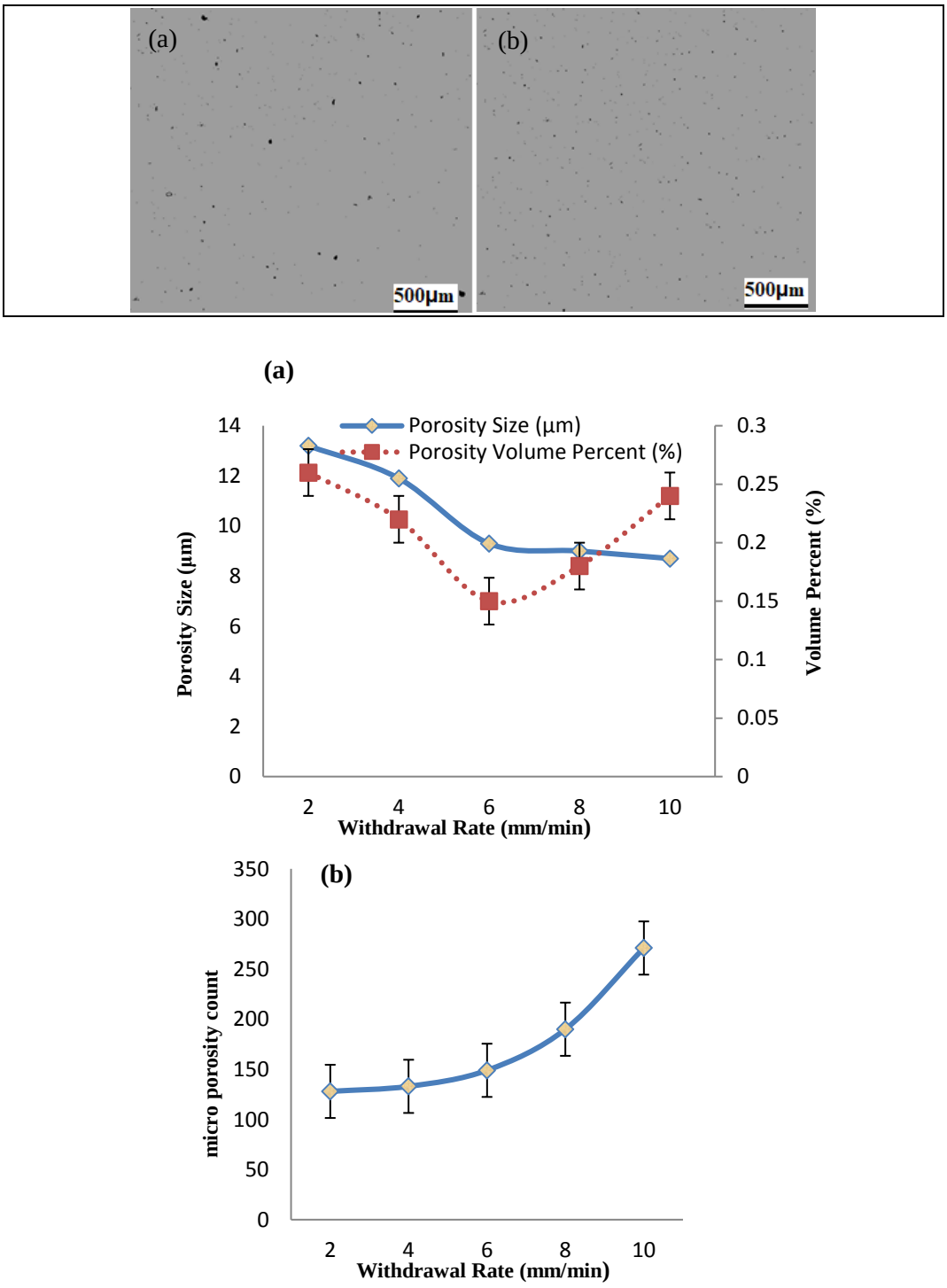

Fig. 8. (a) The size and volume percent of micro-porosities, and (b) micro-porosities number per section.

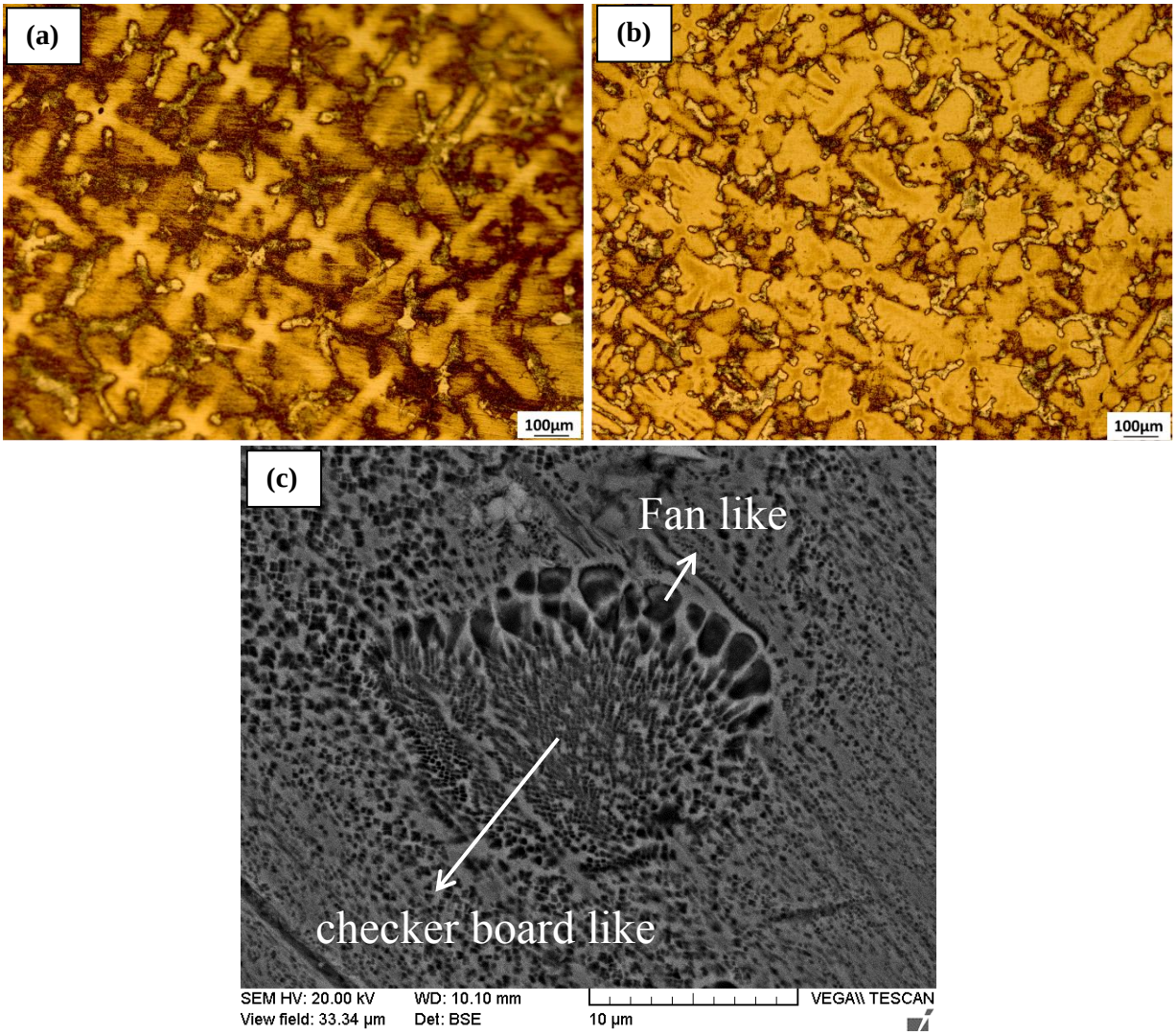

Fig. 9. Optical image of eutectic islands in the specimens solidified at (a) 2, (b) 10 mm.min^{-1}, and (c) SEM micrograph of the checkerboard-like and fan-like structure of eutectic phase for DS Rene 80 solidified at 8 mm.min^{-1} withdrawal rate.

Ordering, peritectic and eutectic transformations of Ni-based superalloys are expressed in equations 3 to 5.

$\gamma \rightarrow \gamma + \gamma'$ ordering (3) [26]

$L + \gamma \rightarrow \gamma'$ peritectic (4) [26]

$L \rightarrow \gamma + \gamma'$ eutectic (5) [26]

Ordering transformation completely occurs through solid-state diffusion, while peritectic transformation involves diffusion in both melted and solid phases. On the other hand, eutectic transformation only considers diffusion in the melt state [26]. Moreover, based on Eq. 6 [27], the melt diffusion coefficient (D_l) is far higher than its counterpart in the solid state (D_s). Therefore, it seems that the growth kinetics of eutectic transformation is higher than the peritectic one. So, it can be expressed that in the eutectic island, fine Checker Board-like sections are formed by peritectic transformation while the eutectic transition is responsible for the formation of fan-like structure in the last stage of solidification.

$D_l \gg D_s$ (6) [27]

3.4. Stress rupture strength

Stress-rupture tests were carried out at 191 MPa, and 980°C on the specimens, and the results are shown in Figure 11. The sample with less solidification microporosity and well-orientated dendritic structure, i.e., the one directionally solidified at 6 mm.min^{-1} gives higher rupture life of 25.43 hrs. Figure 8a shows that the samples solidified at the rate of 6 mm.min^{-1} has the least volume fraction of porosity, and also these porosities have the least size. At the withdrawal rate of 8 and 10 mm.min^{-1}, the rupture life decrease to 10 and 12 hrs, respectively. These two samples have the most volume fraction of microporosity that could reduce the rupture life. Nakagava et al. [28] tested the tensile and stress rupture properties of Rene 80, which directionally solidified at 3 and 6 mm.min^{-1}. They found that the best tensile strength at 870°C is for the withdrawal

rate of 3 mm.min^{-1}. They also reached the rupture life of 44.3 hrs at 190 MPa and 982°C for the sample, which directionally solidified at the withdrawal rate of 6 mm.min^{-1} [28]. For DD10 superalloy, the maximum rupture life of 79.8 hrs at 235 MPa and 1000°C was found at the withdrawal rate of 12 mm.min^{-1} [19]. Furthermore, these two samples have freckle defects that will be discussed in another paper.

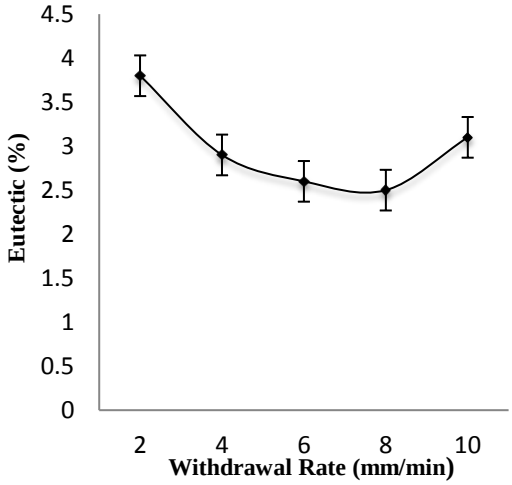

Fig. 10. The volume percent of eutectic with withdrawal rate.

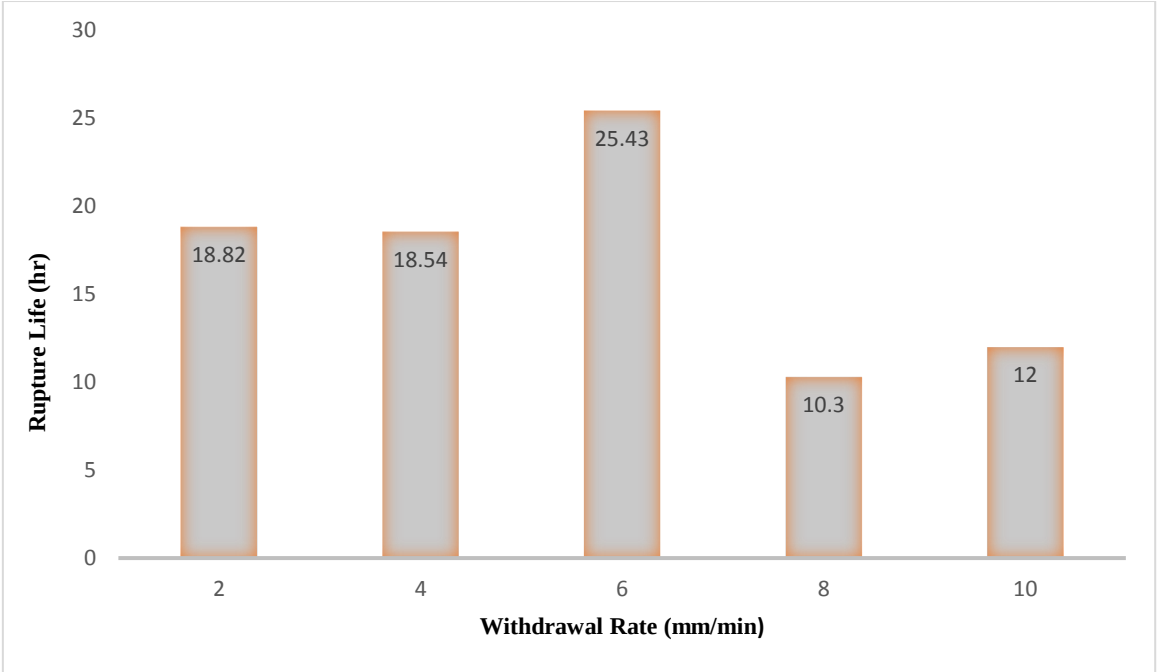

Fig. 11. Variation of stress rupture life as a function of withdrawal rate.

4. Conclusions

Based on the findings of the present study, the following conclusions are drawn:

(1) The relationships between withdrawal rate and dendrite arm spacings were investigated, and it was found that withdrawal rate has a direct effect on PDAS and SDAS.

(2) Increase of withdrawal rate from 2 to 10 mm.min^{-1} reduced the microporosity size from 13.2 to 8.7 µm. By increasing of withdrawal rate, the microporosity volume fraction decreased to 0.15 Vol% at 6 mm.min^{-1} and increased to 0.24 Vol% at 10 mm.min^{-1}. This is due to the increase of nucleation site of pores as the result of finer dendritic structure. Therefore, a withdrawal rate of 6 mm.min^{-1} is the optimal value to obtain a structure with minimum porosity and proper mechanical features.

(3) In the eutectic island, fine Checker Board-like sections are formed by peritectic transition, while the eutectic transition is responsible for the formation of a fan-like structure in the last stages of solidification.

(4) The sample directionally solidified at 6 mm.min^{-1} with less solidification microporosity and well-

orientated dendritic structure gives higher rupture life of 25.43 hrs.

References

[1] R. C. Reed. The superalloys: fundamentals and applications. Cambridge: Cambridge university press; 2008.
[2] C. Yang, Y. Xu, H. Nie, "Effects of heat treatments on the microstructure and mechanical properties of Rene 80", Mater. Des., Vol. 43, 2013, pp. 66–73.
[3] A. Ohtomo, Y. Saiga, "Directional solidification of Rene' 80", Jpn. Inst. Met. Trans., Vol 17, 1976, pp 323–329.
[4] H. Zhang, O. A. Ojo. J. Mater. Sci. "TEM analysis of Cr–Mo–W–B phase in a DS nickel based superalloy", Vol. 43, 2008, pp. 6024–6028.
[5] T. Goswami, H. Hänninen, "Dwell effects on high temperature fatigue behavior –. Part I.", Mater. Des., Vol.22, 2001, pp. 199–215.
[6] R. K. Sidhu, O. A. Ojo, M. C. Chaturvedi, "Sub-solidus melting of directionally solidified Rene 80 superalloy during solution heat treatment", J. Mater. Sci., Vol. 43, 2008, pp. 3612–3617.
[7] A. Szczotok, B. Chmiela, "Effect of Heat Treatment on Chemical Segregation in CMSX-4 Nickel-Base Superalloy", J. Mater. Eng. Perform., Vol. 23, 2014, pp. 2739–2747.
[8] L. Kunz, P. Lukáš, R. Konečná, "Casting defects and high temperature fatigue life of IN713LC superalloy", Int. J. Fatigue., Vol. 41, 2012, pp. 47–51.
[9] Q. Yue, L. Liu, W. Yang, "Influence of withdrawal rate on the porosity in a third generation Ni based superalloy", Prog. Nat. Sci.: Mater. Int., Vol. 61, 2017, pp. 236–243.
[10] B. S. Bokstein, A. I. Epishin, T. Link, "Model for the porosity growth in single crystal nickel base superalloys during homogenization", Scr. Mater., Vol. 57, 2007, pp. 801–804.
[11] T. Link, S. Zabler, A. Epishin , "Synchrotron tomography of porosity in single crystal nickel base superalloys", Mater. Sci. Eng., Vol. 425A, 2006, pp. 47–54.
[12] E. Bachelet, G. Lesoult, "Quality of castings of superalloys. In: High Temperature Alloys for Gas Turbines", Liege, Belgium, 1978, pp. 665-699.
[13] S. Roskosz, M. Staszewski, A. Cwajna. "A complex procedure for describing porosity in precision cast elements of aircraft engines made of MAR-M 247 and MAR-M 509 superalloys", J. Mater. charact., Vol. 56, 2006, pp.405–413.
[14] J. Zhang, J. Li, T. Jin, "Effect of solidification parameters on the microstructure and creep property of a single crystal Ni base superalloy", J. Mater., Vol. 26, 2010, pp. 889–895.
[15] G. Sifeng , L. Lin , X. Yiku , "Influence of processing parameters on microstructure during investment casting of nickel base single crystal superalloy DD3", China Foundry, Vol. 9, 2012, pp.159–164.
[16] M. M. Zou, J. Zhang, J. G. Li, "Effect of melt overheating history on the microstructure of Ni-Base single crystal superalloy", Adv. Mater. Res., Vol, 217, 2011, 692–696.
[17] G. Liu, L. Liu, C. Ai, "Influence of withdrawal rate on the microstructure of Ni-base single-crystal superalloys containing Re and Ru", J. Alloys Compd., Vol. 509, 2011, pp. 5866–5872.
[18] J. D. Hunt, "Cellular and primary dendrite spacing. In: Solidification and Casting of Metals", Sheffield, England, 1977, pp. 3-9.
[19] W. Kurz, D. J. Fisher, "Dendrite growth at the limit of stability", Acta Metall., Vol 29, 1981, pp. 11–20.
[20] R. Trivedi, "Interdendritic spacing: Part II. A comparison of theory and experiment", Metall. Mater. Trans., Vol. 15A, 1984, pp. 977–982.
[21] T. Z. Kattamis, M. C. Flemings, " Dendrite morphology, micro-segregation, and homogenization of low-alloy steel", Transactions of the Metallurgical Society of AIME, Vol 233,1965, pp. 992-999.
[22] L. G. Peterson, "Directional solidification of land based gas. In: ASME 1989 International Gas Turbine and Aeroengine Congress and Exposition" American Society of Mechanical Engineers. 1989, pp. 332-337.
[23] N. Warnken N, "Studies on the solidification path of single crystal superalloys", J. Phase Equilib. Diffus., Vol. 37, 2016, pp.100–107.
[24] N. D'souza, H. B., Dong, "Solidification path in third-generation Ni-based superalloys with an emphasis on last stage solidification", Scr. Mater., Vol 56, 2007, pp. 41–44.
[25] A. Heckl, R. Rettig, S. Cenanovic, "Investigation of the final stages of solidification and eutectic phase formation in Re and Ru containing nickel-base superalloys" J. Cryst. Growth., Vol. 312, 2010, pp.2137–2144.
[26] Porter DA, Easterling KE, Sherif M. "Phase Transformations in Metals and Alloys". United States: CRC press; 2009.
[27] P. Shewmon, "Diffusion in solids", Springer, 2016.
[28] Y. G. Nakagava, A. Ohtomo and Y. Saiga, "Directional solidification of Rene 80", Trans. Japan Institute Met., Vol. 17, pp. 323-329, 1976.

JMATPRO	Journal of Advanced Materials and Processing 10 (2): 39-46, Spring 2022 http://jmatpro.iaun.iau.ir 20.1001.1.2322388.2022.10.2.5.0

Research Paper

The Effects of Oxide Fluxes on the Penetration Depth of 316L and A516 Steels in A-TIG Welding: a Comparative Study

Mohammad Emami[1], Seyed Hossein Elahi[2*]

1 Assistant Professor, Department of Materials Science and Engineering, University of Bonab, Bonab, Iran.
2 Assistant Professor, Department of Mechanical engineering, Arak University of Technology, Arak, Iran.

ARTICLE INFO

Article history:

Received 3 February 2022
Accepted 17 March 2022
Available online 1 April 2022

Keywords:
A-TIG
Oxide flux
Viscosity
Surface tension
Reverse Marangoni

ABSTRACT

The present work evaluates the mechanisms that cause the weld geometry to change in activating flux TIG (A-TIG) welding. For this purpose, an austenitic 316 stainless steel and ferritic A516 steel in conventional TIG and A-TIG welding were compared and evaluated under the same process parameters. Al_2O_3, Fe_2O_3, MnO_2, SiO_2, and TiO_2 powders were used as activating fluxes. The depth of penetration and width of the beads were measured metallographically. In conventional TIG, the welds of carbon steel and stainless steel had a thickness of about 2.2 mm and 1.7 mm, respectively. A-TIG welding of 316 SS using TiO_2, MnO_2, and Fe_2O_3 led to a 75% increase in the weld depth. In the case of Al_2O_3 and SiO_2 the weld depth increased 50% and 9%, respectively. However, in A516 steel, less thermodynamically stable oxide fluxes such as MnO_2, and Fe_2O_3 had a smaller effect i.e., 9-22% increases. More stable oxides like Al_2O_3, SiO_2, and TiO_2 caused a decrease of about 30% in the weld depth compared to the conventional TIG weld. It was proposed that when the penetration increases, reverse Marangoni is dominant. This mechanism is mainly associated with viscosity and surface tension that vary by the dissolution of oxygen in the melt. Regarding penetration reduction, as in the case of more stable oxides like SiO_2, the energy dissipation by the flux through heating and dissociation of the oxide and barrier effect of the undissolved oxide dominate.

Citation: Emami, M.; Elahi, S.H. (2022). The Effects of Oxide Fluxes on the Penetration Depth of 316L and A516 Steels in A-TIG Welding: a Comparative Study, Journal of Advanced Materials and Processing, 10 (2), 39-46. Dor: 20.1001.1.2322388.2022.10.2.5.0

* **Corresponding Author**
E-mail Address: h.elahi@arakut.ac.ir

1. Introduction

TIG welding is a popular method for joining ferrous and non-ferrous alloys [1]. High-quality and clean welds, good surface finish, and inexpensive equipment are some of the advantages of this technique [1]. The low deposition rate and productivity of TIG welds have restricted the application of this method to thin sections, which is the reason for its slow growth rate in the industry [2]. Enhancing the penetration of TIG welding could compensate for the low deposition rate. A thin layer of oxide or fluoride fluxes could enhance the penetration depth of the welds. The process is known as active flux TIG, or A-TIG, and was introduced by Paton Electric Welding Institute in the 1960s [3, 4]. The flux increases the penetration by contracting the arc and reversing the Marangoni convection. Li et al. [5] investigated the effect of oxygen directly blown to the weld pool through a double-shielded TIG method on the shape of the weld pool. Oxygen caused a deeper weld pool compared to TIG welding [5]. Double-shielded (Ar + CO_2) TIG welding of carbon steel also confirmed that certain amounts of oxygen from decomposing of CO_2, could increase the penetration depth [6]. Small additions of SO2 in argon shielding gas improved joint penetration [7]. The addition of small amounts of sulfur and selenium, tolerable by the base metal, could enhance TIG penetration [8, 9]. The considerable effect of MWCNT-TiO_2 flux on the penetration depth of 6061 aluminum was confirmed by Muzamil et al. [2]. Ramkumar et al. [10] reported that both SiO_2 and Fe_2O_3 fluxes improved the weld depth in SS430 and made 5 mm-thick welds accessible in a single pass. The effects of Cu_2O, NiO, Cr_2O_3, SiO_2, and TiO_2 fluxes on the penetration depth of SS304 TIG welds were investigated by Lu et al. [11]. Yushchenko et al. [12] did experimental and mathematical investigations on the electromagnetic and hydrodynamic processes occurring in the weld pool of SS304 in TIG and A-TIG welding and found a good agreement between experimental and calculated results. The comparison of mono- and multi-component oxide fluxes on the TIG welding of stainless steels was reported in [1, 13, 14]. A mixture of MnO_2 and ZnO fluxes led to full penetration in 5 mm-thick SS304 sheets [15]. Several mechanisms were proposed for the higher penetration associated with activating fluxes, two of which are commonly accepted: reverse Marangoni and arc constriction [16-18]. The former is attributed to the reduction of the surface tension at the center of the weld pool under the influence of oxygen and the resulting convection from the periphery to the center of the pool. The latter refers to the reduction of the plasma arc diameter while moving from the bare to the flux-coated surface. The reduced arc diameter leads to an increased current density and, therefore, a narrower and deeper weld. Buoyancy forces, electromagnetic forces, and aerodynamic forces are less common mechanisms proposed in the literature [19].

A-TIG has principally been known to increase the penetration depth of the welds. Nonetheless, in some circumstances, fluxes could lower the weld penetration, which has been disregarded in the research works. Moreover, researchers disagree on a single depth-enhancing mechanism in A-TIG welding. Hence, in this paper, two objectives are pursued: first, to determine the dominant mechanisms responsible for increasing the penetration depth in A-TIG welding. Second, to explain factors that may render the A-TIG process less efficient. Hence, the effects of various oxide fluxes on the penetration depth of SS316 and A516 ferritic steel with different thermophysical properties were studied. The results were compared with the preceding works, and some mechanisms were proposed following a comprehensive discussion.

2. Experimental procedure

Plates of SS316L and A516 Grade 70 steel with dimensions of 80mm ×40mm ×8mm were used, and the chemical compositions are shown in Table 1. The chemical composition and trace elements, such as sulfur, can have a great impact on weld penetration [9]. In order for the chemical composition to be as constant as possible, all tests were performed on a small piece of steel. Bead-on-plate welding was performed to avoid any discrepancies caused by edge preparation and fitting of the sample. Five different oxide powders of Fe_2O_3, Al_2O_3, SiO_2, TiO_2, and MnO_2 with a purity of 99.5% were used. The oxide powder was added to the acetone and then mixed using a mechanical stirrer to obtain a homogeneous activating agent. A thin layer of the flux with a thickness of about 0.2 mm and a width of 20 mm was applied on the specimens using a paintbrush. To obtain a reliable flux thickness, oxides were weighed using a 0.01 g balance following the calculations shown in Table 2. After the acetone was evaporated, a dry layer of flux remained on the surface.

Table 1. Chemical composition of the SS316L and A516 steel (in wt.%)

	Fe	C	Mn	Si	P	S	Cr	Mo	Ni	N
SS316L	Bal.	0.02	1.51	0.42	0.017	0.002	16.8	2.15	10.1	0.0
A516	Bal.	0.16	1.17	0.33	0.009	0.003	0.02	0.006	0.01	-

Single-pass TIG welding using a non-consumable thoriated tungsten electrode (diameter of 2.4 mm) was performed by employing a DCEN polarity power source at the current of 100 A, constant speed of 2 mm/s under high purity argon shielding with a flowrate of 12 L/min. To perform welding at a constant travel speed, a mechanized welding process was used. The angle of the electrode was 30°, and its tip was at a distance of 2 mm from the surface. To observe the arc shape, a camera was placed in front of the weld at a secure distance from the welding assembly. After the welding, the cross-section of the samples was prepared for macro-examination following the conventional metallographic procedure. The geometry (depth and width) of the welds was measured by a non-contact measuring system at a magnification of 8X.

Table 2. The calculations to obtain the required oxide mass for a flux of 0.2 mm thickness

Flux	Width (cm)	Length (cm)	Thickness (cm)	Density (g/cm^3)	Mass (g)
TiO_2	2	15	0.02	4.23	2.54
SiO_2	2	15	0.02	2.65	1.59
Al_2O_3	2	15	0.02	3.95	2.37
Fe_2O_3	2	15	0.02	5.24	3.14
MnO_2	2	15	0.02	5.03	3.02

3. Results and Discussion

The macrographs of the cross-sections of A516 samples welded with and without activating fluxes could be seen in Fig. 1. The MnO_2 and Fe_2O_3 flux-assisted welds (Figs. 1c, d) had depths comparable to that of the conventionally welded sample (Fig. 1a). But the welds obtained using TiO_2, SiO_2, and Al_2O_3 (Figs. 1b, e, and f) were shallower than the TIG weld. This means a negative and/or negligible effect of fluxes on the penetration depth of the carbon steel welds. These results contradict those obtained by Mirzaei et al. [6] and de Azevedo et al. [20] on A-TIG welding of ferritic steels. A wide heat-affected zone (HAZ) observed in A516 steel could be attributed to the large thermal conductivity of carbon steels [18].

The macrographs of the cross-sections of the SS316 specimens welded using TIG and A-TIG processes are shown in Fig. 2. It is seen that TIG welding of SS316 caused a shallow and wide weld pool. According to Fig. 2(b-f), various fluxes enhanced the penetration depth and reduced the width of the bead. Nonetheless, SiO_2 and to a lesser extent Al_2O_3 were less effective. Comparing Fig. 2a and Fig. 1a shows that the penetration depth of the original weld of A516 was greater than that of SS316. However, when the same fluxes were employed the penetration depth was reversed.

Fig. 3a makes a quantitative comparison of the penetration depth of A516 and SS316 welds using different fluxes. Fig. 3a shows that in the case of SS316, TIG welding led to the shallowest weld with 1.7 mm depth. TiO_2, MnO_2, and Fe_2O_3 caused about a 75% increase in the penetration depth of SS316. Al_2O_3 by about 50% increase was a little less effective. The least effective flux was SiO_2 with merely a 9% of depth increase. The penetration depths in this study were smaller than those reported by Tseng et al. [21] and Liu et al. [22] because they performed welding at a higher current and/or a lower speed which provided greater heat for deeper weld.

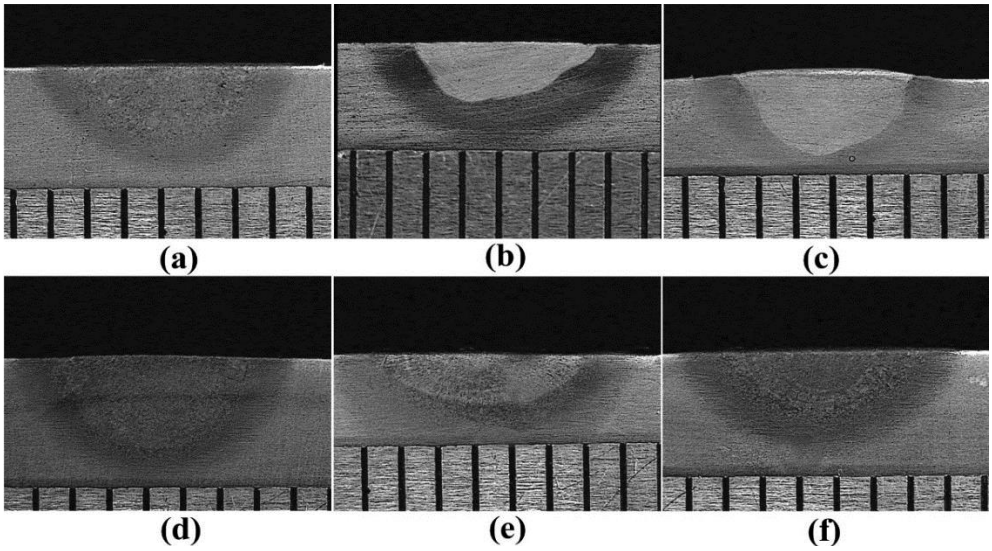

Fig. 1. Cross-sectional view of A516 welds welded a: without flux, b: with TiO_2 flux, c: with MnO_2 flux, d: with Fe_2O_3, e: with SiO_2 flux, and f: with Al_2O_3 flux.

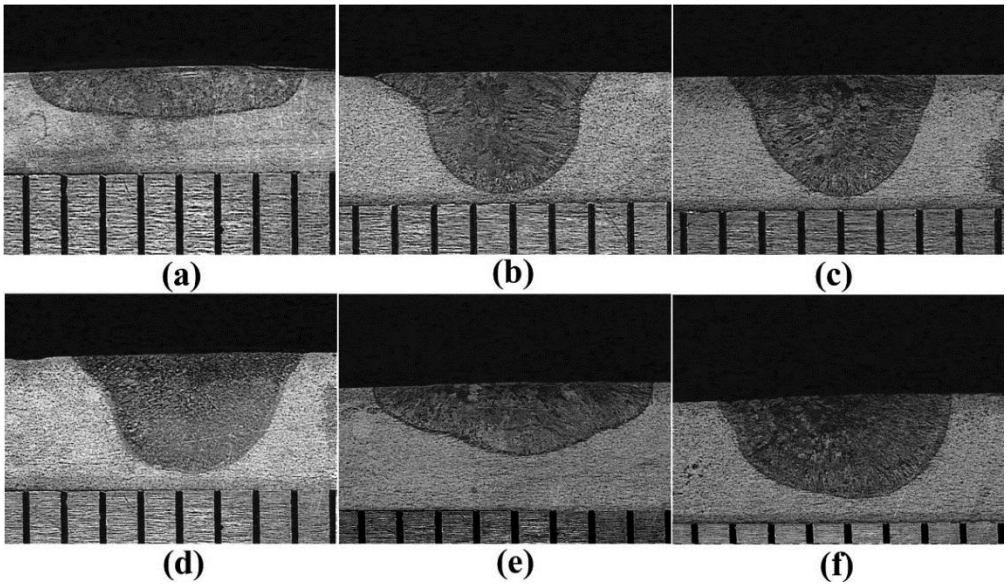

Fig. 2. Cross-sectional view of SS316 welds welded a: without flux, b: with TiO_2 flux, c: with MnO_2 flux, d: with Fe_2O_3 flux, e: with SiO_2 flux, and f: with Al_2O_3 flux.

In TIG welding of A516, a weld depth of 2.2 mm was obtained, about 30% higher than that of SS316. However, the depth of the flux-assisted welds decreased in the case of TiO_2, SiO_2, and Al_2O_3, and/or the increase was not significant when MnO_2 was employed. According to Fig. 1, the best result was attained when Fe_2O_3 was used. Similar results were obtained in studies of Tseng et al. [21] in A-TIG welding of SS316 and Dhandha and Badheka [23] in welding of P91 steel when stable oxides like Al_2O_3 and CaO were used. The effect of activating fluxes on the width of the bead of different specimens shown in Fig. 3b is quite straightforward. For both ferritic and austenitic steels, the weld bead narrowed down by applying fluxes, except SiO_2, which marginally got the weld widened.

Regarding TIG welding, a deeper weld was observed in A516 steel than in SS316 under the same welding parameters. The thermal conductivity and diffusivity of SS316 are lower than those of carbon steel. Thermal diffusivity is the thermal conductivity divided by density and specific heat capacity at constant pressure, suggesting that heat transfers slowly in a material with low thermal diffusivity. This may increase weld penetration by concentrating the arc energy. However, the viscosity of austenitic steels is lower than ferritic steels [24]. It was reported that an increase in the melt viscosity would result in a reduced weld penetration because high viscosity restricts the fluid flow [25, 26]. This means that in stainless steels, viscosity has a greater impact on weld penetration rather than thermal conductivity. It is noteworthy that, during heating, in stainless steel and carbon steel welds, the HAZ transforms to delta ferrite and austenite, respectively [27, 28]. This makes the heat transfer of these steels complicated. It was beyond the scope of this paper to measure the HAZ size of the welds, and no reliable data could be obtained from the macrographs shown in Figs. 1 and 2. However, it has been widely accepted and confirmed that under the same welding conditions, ferritic alloys show a wider HAZ than austenitic ones [29]. The bigger HAZ width in carbon steel indicates this alloy's higher conductivity. The other important point is the higher sulfur content of carbon steels in routine products, and sulfur could increase the weld penetration, which means the carbon steel with higher sulfur content already has an inherent active flux.

The results showed that SiO_2 and Al_2O_3 were less effective in enhancing the weld depth. A schematic representation in Fig. 4 compares the conventional TIG (Fig. 4a) with A-TIG in different conditions (Figs. 4b, c). According to Ellingham–Richardson diagram, SiO_2, TiO_2, and Al_2O_3 are the most stable oxides. To have a good penetration in the A-TIG process, the oxide flux should be dissociated and oxygen atoms should be dissolved in the melt. This happens more effectively in the less stable oxides. Moreover, the stoichiometry of the oxide may affect the amount of oxygen provided for the melt. Theoretically, oxides like MnO_2 and TiO_2 should be more effective than Al_2O_3. However, the weld penetration measurements showed an exception in the case of SiO_2. In more stable oxides, the arc temperature, especially at the colder peripheral zone, was insufficient to decompose the oxides. When the arc collides with stable oxides such as Al_2O_3 or SiO_2, the arc energy is not enough to decompose the flux, and the flux layer acts as a barrier against the arc. Thus, the arc is deviated from the straight path and spreads out toward the arc edges, which leads to an increased arc width. This mechanism can be schematically seen in Fig. 4c.

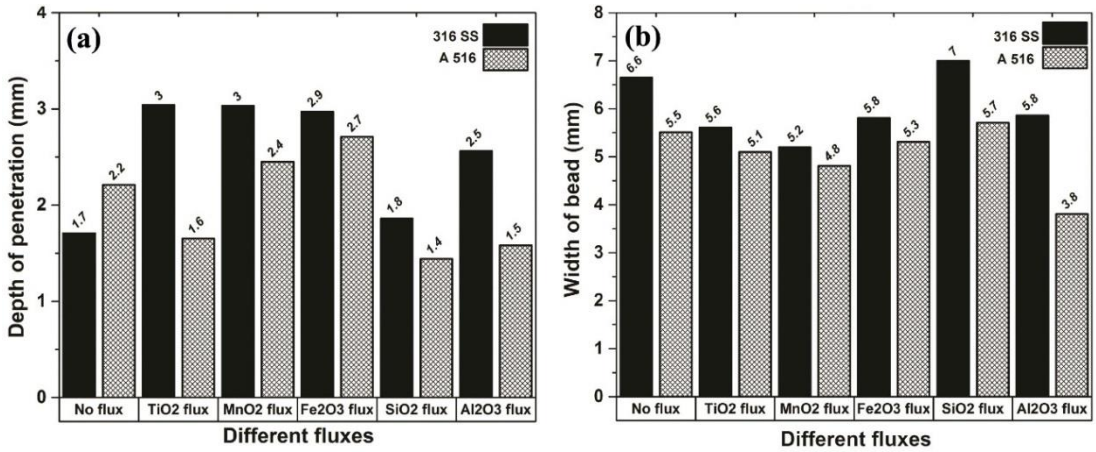

Fig. 3. a: Penetration depth of the welds with and without flux, b: width of the weld beads with and without flux.

In contrast, when the arc energy is able to overcome the flux layer, a small hole forms in the center of the flux due to a higher temperature in the middle of the arc. The metal underneath is directly exposed to the arc energy, and leads to increased metal evaporation, and the arc flare concentrates in the center of the weld pool [30, 31].

As stated earlier, the reverse effect of fluxes has been overlooked in the literature. When fluxes are used, the arc energy could be dissipated in some ways: consuming the arc energy by heating the fluxes, decomposition of the flux, and the barrier effect of the fluxes. Generally, the formation of an oxide layer on the surface of the weld pool reduces the weld penetration [6] and, more importantly, prevents the weld pool surface from moving freely and, therefore, inward Marangoni convection could be disturbed even if the oxide has a thickness lower than 50 μm [32] which is much thinner than the thickness of active fluxes. Also, when the heat input is insufficient to decompose the oxide flux, the fluid flow could get the oxide layer immersed in the melt pool as an inclusion. The formation of a dual-phase fluid (i.e., the melt and oxide inclusions), in turn, leads to a viscosity rise and a reduction in weld penetration [33, 34]. In brief, in A-TIG, two competing factors affect the weld penetration; the increase in the penetration by reversed Marangoni and arc constriction, and the reduction of the penetration by decreasing the arc force or dissipation of arc energy.

To verify the above arguments, MnO_2 as the most efficient flux was chosen for further study. A flux with a thickness of 0.5 mm (2.5 times thicker) was applied on SS316 and welding was performed using the same parameters. As shown in Fig. 5a, in the case of the thicker flux, in comparison with the conventional weld, the penetration of the weld decreased by about 22.3%, but the width of the weld increased by about 9.8%. This means that the flux acts as a barrier. The outward deviation of the weld was confirmed by the shape of the arc captured during welding (Fig. 5b). When the heat input increased by about 37 percent, a deep and narrow weld formed once again (Fig. 5c), even more than the thin flux. In this case, the shape of the arc was more focused (Fig. 5d), which agrees with the corresponding deeper weld. In higher heat input and flux thickness, perhaps a greater amount of the flux is decomposed, resulting in more oxygen entering the weld. Therefore, the enhancing mechanisms act more efficiently. Increasing heat input by the reduction in welding speed or increasing welding current leads to the higher efficiency of active fluxes [35].

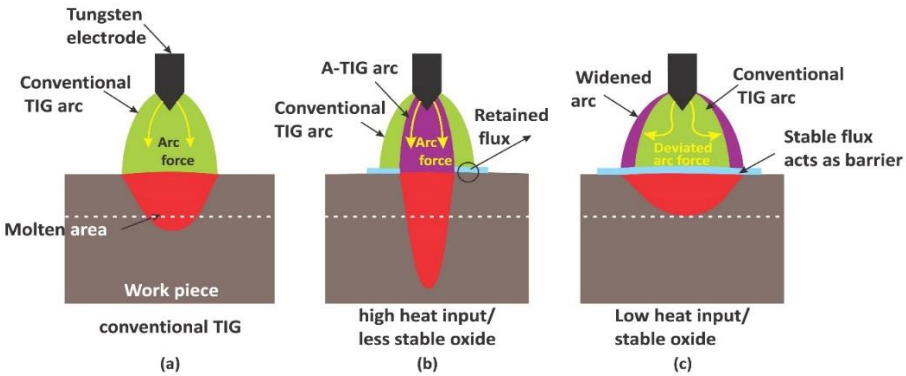

Fig. 4. Schematic representation of different mechanisms affecting penetration depth, a: conventional TIG, b: flux assisted TIG in high heat input process or less stable oxide fluxes, c: flux assisted TIG in low heat input process or stable oxide fluxes.

Comparing ferritic and austenitic steels with different thermo-physical properties helps to better understand the most contributing mechanisms in increasing weld penetration. Molten stainless steel has a higher viscosity than carbon steel [24]. The higher viscosity of austenitic steel was attributed to Ni alloying [36]. The surface tensions of austenitic and ferritic steels are almost the same [37]. Also, the melts of both alloys have nearly similar magnetic properties. Therefore, viscosity is the main difference between the melts of the two alloys in this study. However, this was not much discussed in the literature. A decrease in the melt viscosity would increase the weld penetration [25]. Moreover, dissolved oxygen could affect the viscosity and surface tension of the stainless steel considerably [26]. It could be argued that in the A-TIG process, if the weld penetration changes, especially in SS316, the mechanism in which the viscosity and surface tension are controlling parameters, i.e., the reversed Marangoni, could be the dominant mechanism. This disagrees with the works of Howse and Lucas [38] and Vasantharaja and Vasudevan [39] that propose arc constriction as the main penetration-enhancing mechanism.

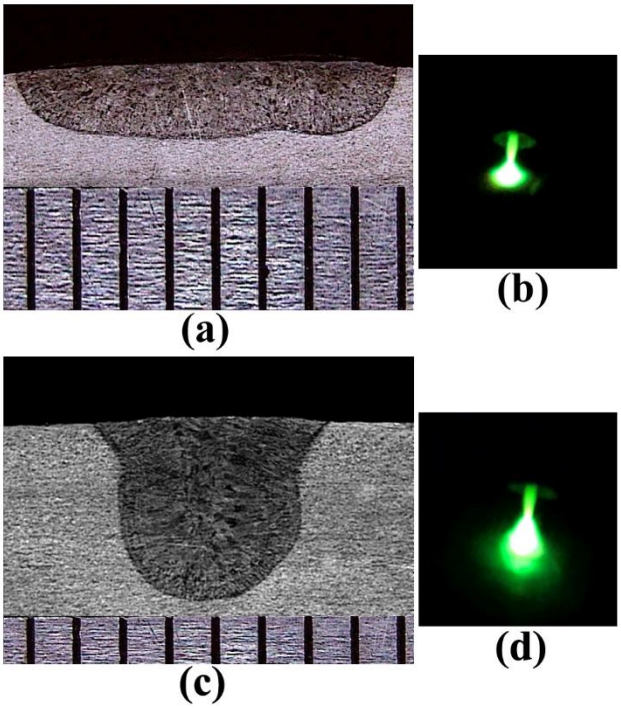

Fig. 5. Cross-sectional view and weld arc shape of the SS316 welds welded with a thick layer of MnO_2 flux a, b: low heat input (weld width: 7.6 mm, weld penetration 1.5 mm), c, d: high heat input (weld width: 4.7 mm, weld penetration 3.7 mm).

With regards to the smaller impact of oxide fluxes on A516 steel, it could be claimed that plain molten steel itself has low viscosity (less than 3.4 cP [40]), and the fluxes could not effectively reduce the surface tension of the weld in the welding temperature range [41]. Therefore, the mechanisms that increase penetration depth do not work effectively. This suggests that the decreasing mechanisms should act better, and finally, a reduction in the penetration takes place in the case of carbon steel. It is important to note that carbon steel has an inherent sulfur active agent, and oxide active fluxes could not activate or enhance the increasing mechanism. However, anyway, they could reduce the arc energy. In contrast, molten stainless steel has higher viscosity [42], and by adding oxygen, the increasing mechanism works more effectively, and finally, the penetration increases.

4. Conclusions

The present study was conducted to determine the dominant mechanism changing the geometry of the welds in the A-TIG welding of steels. The behaviors of ferritic and austenitic steel were evaluated using Al_2O_3, Fe_2O_3, MnO_2, SiO_2, and TiO_2 fluxes with different thermodynamical stabilities.

1- The oxide fluxes caused the penetration depth of the stainless steel welds to increase up to about 75 percent in the case of TiO_2, MnO_2 and Fe_2O_3. Al_2O_3 and SiO_2, with a respective 50 and 9 percent increase in the weld depth, were less effective.

2- In the case of carbon steel, the more stable oxides i.e., Al_2O_3 and SiO_2 had reversed effects and caused the depth of penetration to reduce by about 30 percent compared to that in conventional TIG welding. Oxides such as Fe_2O_3 could play a role in enhancing the penetration depth.

3- Based on the thermo-physical properties of carbon steel and stainless steel, it was decided that the penetration enhancement was mainly governed by the viscosity and surface tension, i.e., the reversed Marangoni rather than arc constriction was the dominating mechanism.
4- In active TIG, two mechanisms compete with each other: one increases the penetration, and the other one decreases the penetration. The former mechanism was well investigated in the literature, whereas the latter was completely ignored. The type and thickness of flux, i.e., the energy for flux decomposition and the barrier effect, are two parameters that consume and dissipate arc energy and reduce weld penetration.
5- When the heat input/arc energy is low, and a thick or stable flux exists, the second mechanism is dominant, and a reduction in the weld penetration results. But in high heat inputs and the presence of thin or less stable fluxes, the first mechanism dominates, and weld penetration increases. This has led researchers to obtain conflicting results in their investigations.
6- In alloys with higher viscosity and surface tension, like stainless steel, the first mechanism could be more effective. But contrariwise, in plain carbon steel with lower viscosity and surface tension, the enhancing mechanism's effect is insignificant, and the second mechanism could reduce the penetration and increase the weld width.

References

[1] G. Venkatesan, J. George, M. Sowmyasri, V. Muthupandi, "Effect of ternary fluxes on depth of penetration in A-TIG welding of aisi 409 ferritic stainless steel", Proc. Mat. Sci., Vol. 5, No. 2014, pp. 2402-2410.
[2] M. Muzamil, J. Wu, M. Akhtar, V. Patel, A. Majeed, J. Yang, "Multicomponent enabled MWCNTs-TiO2 nano-activating flux for controlling the geometrical behavior of modified TIG welding joint process", Diam. Relat. Mater., Vol. 97, No. 2019, pp. 107442.
[3] R. Vidyarthy, D.K. Dwivedi, "Activating flux tungsten inert gas welding for enhanced weld penetration", J. Manuf. Process., Vol. 22, No. 2016, pp. 211-228.
[4] D. Sharma, P.K. Ghosh, S. Kumar, S. Das, R. Anant, N. Kumar, "Surface hardening by in-situ grown composite layer on microalloyed steel employing TIG arcing process", Surf.Coat. Tech., Vol. 352, No. 2018, pp. 144-158.
[5] D. Li, S. Lu, W. Dong, D. Li, Y. Li, "Study of the law between the weld pool shape variations with the welding parameters under two TIG processes", J. Mater. Process. Tech., Vol. 212, No. 1, 2012, pp. 128-136.
[6] M. Mirzaei, A. Khodabandeh, H. Najafi, "Effect of active gas on weld shape and microstructure of highly efficient TIG welded A516 low carbon steel", T. Indian I. Metals, Vol. 69, No. 9, 2016, pp. 1723-1731.
[7] C. Heiple, P. Burgardt, "Effects of SO2 shielding gas additions on GTA weld shape", Weld. J., Vol. 64, No. 6, 1985, pp. 159-162.
[8] P. Burgardt, C. Heiple, "Interaction between impurities and welding variables in determining GTA weld shape", Weld. J., Vol. 65, No. 6, 1986, pp. 150.
[9] S. Pierce, P. Burgardt, D. Olson, "Thermocapillary and arc phenomena in stainless steel welding", Weld. J., Vol. 78, No. 1999, pp. 45-s.
[10] K.D. Ramkumar, A. Chandrasekhar, A.K. Singh, S. Ahuja, A. Agarwal, N. Arivazhagan, A.M. Rabel, "Comparative studies on the weldability, microstructure and tensile properties of autogeneous TIG welded AISI 430 ferritic stainless steel with and without flux", J. Manuf. Process., Vol. 20, No. 2015, pp. 54-69.
[11] S. Lu, H. Fujii, H. Sugiyama, M. Tanaka, K. Nogi, "Weld penetration and marangoni convection with oxide fluxes in GTA welding", Mater. Trans., Vol. 43, No. 11, 2002, pp. 2926-2931.
[12] K.A. Yushchenko, D.V. Kovalenko, I.V. Krivtsun, V.F. Demchenko, I.V. Kovalenko, A.B. Lesnoy, "Experimental studies and mathematical modelling of penetration in TIG and A-TIG stationary arc welding of stainless steel", Weld. World, Vol. 53, No. 9, 2009, pp. 253-263.
[13] G. Chandrasekar, C. Kailasanathan, D.K. Verma, K. Nandagopal, "Optimization of welding parameters, influence of activating flux and investigation on the mechanical and metallurgical properties of activated TIG weldments of AISI 316 L stainless steel", T. Indian I. Metals, Vol. 70, No. 3, 2017, pp. 671-684.
[14] G. Venkatesan, V. Muthupandi, J. Justine, "Activated TIG welding of AISI 304L using mono- and tri-component fluxes", Int. J. Adv. Manuf.Tech., Vol. 93, No. 1, 2017, pp. 329-336.
[15] H. Huang, S. Shyu, K. Tseng, C. Chou, "Evaluation of TIG flux welding on the characteristics of stainless steel", Sci. Technol. Weld. Join., Vol. 10, No. 5, 2005, pp. 566-573.
[16] S. Jayakrishnan, P. Chakravarthy, "Flux bounded tungsten inert gas welding for enhanced weld performance—a review", J. Manuf. Process., Vol. 28, No. 2017, pp. 116-130.
[17] A. Berthier, P. Paillard, M. Carin, F. Valensi, S. Pellerin, "TIG and A-TIG welding experimental investigations and comparison to simulation: Part 1: Identification of marangoni effect", Sci. Technol. Weld. Join., Vol. 17, No. 8, 2012, pp. 609-615.
[18] N.P. Patel, V.J. Badheka, J.J. Vora, G.H. Upadhyay, "Effect of oxide fluxes in activated TIG welding of stainless steel 316LN to low activation

ferritic/martensitic steel (LAFM) dissimilar combination", T. Indian I. Metals, Vol. 72, No. 10, 2019, pp. 2753-2761.
[19] J.J. Vora, V.J. Badheka, "Improved penetration with the use of oxide fluxes in activated TIG welding of low activation ferritic/martensitic steel", T. Indian I. Metals, Vol. 69, No. 9, 2016, pp. 1755-1764.
[20] A.G. Luciano de Azevedo, V.A. Ferraresi, J.P. Farias, "Ferritic stainless steel welding with the A-TIG process", Weld. Int., Vol. 24, No. 8, 2010, pp. 571-578.
[21] K.-H. Tseng, C.-Y. Hsu, "Performance of activated TIG process in austenitic stainless steel welds", J. Mater. Process. Tech., Vol. 211, No. 3, 2011, pp. 503-512.
[22] G.-h. Liu, M.-h. Liu, Y.-y. Yi, Y.-p. Zhang, Z.-y. Luo, L. Xu, "Activated flux tungsten inert gas welding of 8 mm-thick AISI 304 austenitic stainless steel", J. Cent. South Univ., Vol. 22, No. 3, 2015, pp. 800-805.
[23] K.H. Dhandha, V.J. Badheka, "Effect of activating fluxes on weld bead morphology of P91 steel bead-on-plate welds by flux assisted tungsten inert gas welding process", J. Manuf. Process., Vol. 17, No. 2015, pp. 48-57.
[24] J.J. Valencia, P.N. Quested, "Thermophysical properties", 2013.
[25] B. Pollard, "The effects of minor elements on the welding characteristics of stainless steel", Weld. J., Vol. 67, No. 9, 1988, pp. 202s-213s.
[26] D. Aidun, S. Martin, "Effect of sulfur and oxygen on weld penetration of high-purity austenitic stainless steels", J. Mater. Eng. Perform., Vol. 6, No. 4, 1997, pp. 496-502.
[27] P. Marashi, M. Pouranvari, S. Amirabdollahian, A. Abedi, M. Goodarzi, "Microstructure and failure behavior of dissimilar resistance spot welds between low carbon galvanized and austenitic stainless steels", Mater. Sci. Eng., Vol. 480, No. 2008, pp. 175-180.
[28] P. Kumar, A.N. Sinha, "Effect of pulse width in pulsed ND: YAG dissimilar laser welding of austenitic stainless steel (304 L) and carbon steel (st37)", Lasers Manuf. Mater., Vol. 5, No. 4, 2018, pp. 317-334.
[29] M.H. Bina, M. Jamali, M. Shamanian, H. Sabet, "Investigation on the resistance spot-welded austenitic/ferritic stainless steel", Int. J. Adv. Manuf.Tech., Vol. 75, No. 9, 2014, pp. 1371-1379.
[30] M. Abbaoui, B. Cheminat, P. Andanson, "Influence of the nature of the metal on the conductivity of an argon-metal plasma", J. Phys. D Appl. Phys., Vol. 18, No. 10, 1985, pp. L159.
[31] S. Mishra, T. Lienert, M. Johnson, T. DebRoy, "An experimental and theoretical study of gas tungsten arc welding of stainless steel plates with different sulfur concentrations", Acta Mater., Vol. 56, No. 9, 2008, pp. 2133-2146.
[32] S. Lu, H. Fujii, H. Sugiyama, M. Tanaka, K. Nogi, "Effects of oxygen additions to argon shielding gas on GTA weld shape", ISIJ int., Vol. 43, No. 10, 2003, pp. 1590-1595.
[33] S.H. Elahi, H. Abdi, H. Shahverdi, "Investigating viscosity variations of molten aluminum by calcium addition and stirring", Mater. Lett., Vol. 91, No. 2013, pp. 376-378.
[34] S.H. Elahi, H. Abdi, H. Shahverdi, "A new method for investigating oxidation behavior of liquid metals", Rev. Sci. Instrum., Vol. 85, No. 1, 2014, pp. 015115.
[35] H. Fujii, T. Sato, S. Lu, K. Nogi, "Development of an advanced A-TIG (AA-TIG) welding method by control of marangoni convection", Mater. Sci. Eng. A, Vol. 495, No. 1-2, 2008, pp. 296-303.
[36] L. Pilcher, "Welding dissimilar metals ", 2015.
[37] R. Brooks, P. Quested, "The surface tension of steels", J. Mater. Sci., Vol. 40, No. 9, 2005, pp. 2233-2238.
[38] D. Howse, W. Lucas, "Investigation into arc constriction by active fluxes for tungsten inert gas welding", Sci. Technol. Weld. Join., Vol. 5, No. 3, 2000, pp. 189-193.
[39] P. Vasantharaja, M. Vasudevan, "Studies on A-TIG welding of low activation ferritic/martensitic (LAFM) steel", J.Nucl. Mater., Vol. 421, No. 1-3, 2012, pp. 117-123.
[40] M. Rywotycki, Z. Malinowski, J. Giełżecki, A. Gołdasz, "Modelling liquid steel motion caused by electromagnetic stirring in continuous casting steel process", Arch. Metall. Mater., Vol. 59, No. 2, 2014, pp. 487--492.
[41] K. Morohoshi, M. Uchikoshi, M. Isshiki, H. Fukuyama, "Surface tension of liquid iron as functions of oxygen activity and temperature", ISIJ int., Vol. 51, No. 10, 2011, pp. 1580-1586.
[42] J. Zhou, H.-L. Tsai, T. Lehnhoff, "Investigation of transport phenomena and defect formation in pulsed laser keyhole welding of zinc-coated steels", J. Phys. D Appl. Phys., Vol. 39, No. 24, 2006, pp. 5338.

JMATPRO	Journal of Advanced Materials and Processing 10 (2): 47-58, Spring 2022 http://jmatpro.iaun.iau.ir 20.1001.1.2322388.2022.10.2.6.1

Research Paper

Using of Thermoplastic Polyurethane Granule (TPU) as a Reinforcing Phase and Self-Healing Agent in a Polymer Composite Resin Epoxy to Exhibit Mechanical Properties Recovery

Mostafa Hosseini[1,2], Aazam Ghassemi[1,2*]

1. Department of Mechanical Engineering, Najafabad Branch, Islamic Azad University, Najafabad, Iran

2. Modern Manufacturing Technologies Research Center, Najafabad Branch, Islamic Azad University, Najafabad, Iran

ARTICLE INFO

Article history:

Received 3 February 2022
Accepted 17 March 2022
Available online 1 April 2022

Keywords:
Self-healing
Polyurethane
Resin epoxy
Mechanical properties

ABSTRACT

In this study, for the first time, thermoplastic polyurethane granule (TPU) is used as a reinforcing phase and self-healing agent in a polymer composite epoxy resin (ER) to exhibit mechanical properties recovery. When the polymer composite is damaged or cracked, TPU granules are released at the site of damage and cause auto-repair of surfaces. Therefore, TPU granules with different composition percentages were mixed in silicon molds containing epoxy resin polymer composite. 4 samples with different TPU granules percentages were selected (A= 0 Wt.% TPU, B=10 Wt.% TPU, C=20 Wt.% TPU, and D=30Wt.% TPU). At first, making a deep cut in 4 polymer composite samples, the self-healing process and mechanical properties improvement are investigated by mechanical tests. In the self-repairing behavior of self-healing samples, it is observed that polymer composite samples with self-repairing agents of ER+20 Wt.% TPU granules had the highest self-healing efficiency (60.2%) compared to other specimens. A mechanical test shows that Sample C has a higher Young's modulus (4.837 MPa) and higher tensile strength (9.46 MPa). Also, the impact test illustrated Sample C has a higher impact energy of 7.1 (J/m). Therefore, sample C has the highest mechanical properties among self-healing samples.

Citation: Hosseini, M.; Ghasemi, A. (2022). Using of Thermoplastic Polyurethane Granule (TPU) as a Reinforcing Phase and Self-Healing Agent in a Polymer Composite Resin Epoxy to Exhibit Mechanical Properties Recovery, Journal of Advanced Materials and Processing, 10 (2), 47-58. Dor: 20.1001.1.2322388.2022.10.2.6.1

* * **Corresponding Author**
E-mail Address: aazam77@yahoo.com

1. Introduction

Recently, self-healing materials have become the most important research interest because of community awareness regarding the prolongation of the lifetime of materials, which can save natural resources. The self-healing of materials such as polymers, metals, and concrete was studied to improve the service life of these structures [1,2]. These materials can be divided into two distinct groups: intrinsic and extrinsic self-healing materials. In the first group, based on the action of an added phase or structure, intrinsic self-healing is a mechanism that is in the structure of the material [3-9]. Polymer composites are extensively used in a range of applications, and they have been noteworthy candidates to introduce the self-healing theory into up-to-date engineering materials [2,10]. Not only does this class of polymers improve the ability to heal damage autonomously, rehabilitate mechanical properties, and increase the lifetime of polymers, but also the utilization of highly sophisticated chemical and physical principles has entered the field of merchandise polymers [11, 12]. Self-healing of polymer composite materials can recover from damage without external stimuli and intervention. This sort of material is particularly suited for use in applications that are highly exposed to external impacts and fatigue loading [13,14]. Epoxy resins are kernel materials for self-healing because they can react with a diversity of curing agents or hardeners at various temperatures [15]. Furman et al. [16] introduced the synthesis and characterization of a new diamine curing agent (tetramethylated diaminodiphenylsulfone) for self-healing epoxy resins. Polyethylene-co-methacrylic acid (EMAA) [17,18] and Poly (ethylene-*co*-glycidyl methacrylate) (PEGMA) [19] are also used as healing agents in brittle epoxy polymer. Roy et al. [20] exploit mesoporous silica as an amine immobilizer to endow epoxy resin's healing functionality. Polyurethanes (PUs) are a versatile class of polymers used in both synthesis and applications, and they were extensively used in modern society [21-23] because they are widely used in fields such as aerospace, automotive industry, and architecture, self-healing Polyurethanes have recently become a major research issue [24,25]. Thermoplastic polyurethanes (TPUs), as block copolymers, are the most important class of polyurethanes [26,27] with many great properties such as prolonged mechanical strength, good flexibility in low temperature, prominent wear and abrasion resistance [28-31]. Luan et al. [32] investigated the mechanical and self-healing properties of thermoplastic polyurethane (TPU)-graphene composites. Park et al. [33] developed self-healing TPU at room temperature with robustness, stretchability, and durability surpassing those of current room-temperature self-healable materials. As seen in previous research, TPU granules have not been used as a self-healing in the Epoxy Resin. For the first time, the crack created in the Epoxy Resin (which reduces its mechanical properties) is supposed to be repaired by TPU granules.

In this work, a series of self-healing thermoplastic polyurethane and Epoxy Resin (TPU/ER) composites with different TPU contents were prepared. TPU granules with different composition percentages (0 Wt.%, 10 Wt.%, 20 Wt.%, and 30 Wt.%) were mixed in silicon molds containing epoxy resin polymer composite. When the polymer composite is damaged or cracked, TPU granules are released at the site of damage-causing auto-repair of surfaces by heating. For this purpose, a deep cut in polymer composite samples with different percentages of TPU granules was conducted. Then, all of the samples with different percentages of TPU were in the oven for heating. After that, the healing ability is understudied to study the effect on self-healing behavior. Moreover, the effect on mechanical properties is estimated by three tests: tensile test, impact test, and three-point flexural test.

2. Experimental

1.2. Materials and reagents

The materials used in Thermoplastic polyurethane/Epoxy resin (TPU/ER) composites included: Thermoplastic polyurethane granule (LARIPUR 7025, Coim Company, Italy), Epoxy resin liquid (EP411 Laminating & Casting, DSM Company, the Netherlands) and hardener Epoxy Resin EP411 from DSM Company, and silicon (RTV/2-4425) made in Canada.

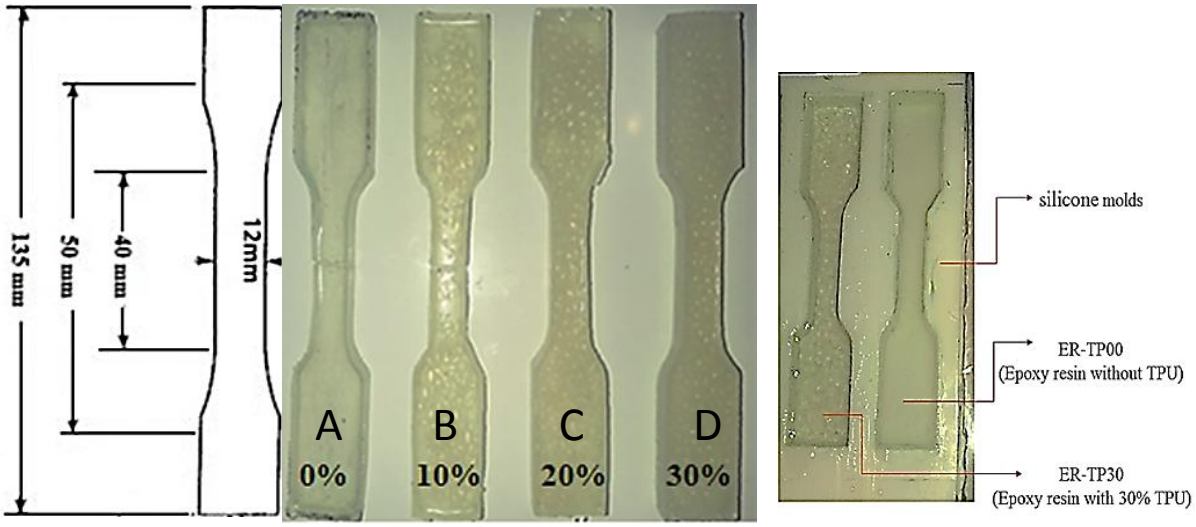

Fig. 1. Prepared samples of TPU/ER composites with different TPUs contents.

2.2. Method and fabrication of composites

At room temperature (20–25 °C), different ratios of epoxy resin (ER) and hardener (15:100) were mixed in a beaker with a mechanical stirrer for 2 minutes. TPUs were added to the mixture with different percentages. Fig. 1 shows that samples with different TPUs contents were named Sample- A, Sample B, Sample C, and Sample D, which correspond to TPU content of 0 Wt.%, 10 Wt.%, 20 Wt.%, and 30 Wt.%, respectively. The prepared liquid composites were cast into silicone molds already made for mechanical testing. Then, they were dried and rigid for two days at room temperature (20–25 °C). After two days, the specimens were taken out of the molds for mechanical tests. The test samples were also obtained by the same casting process mentioned above.

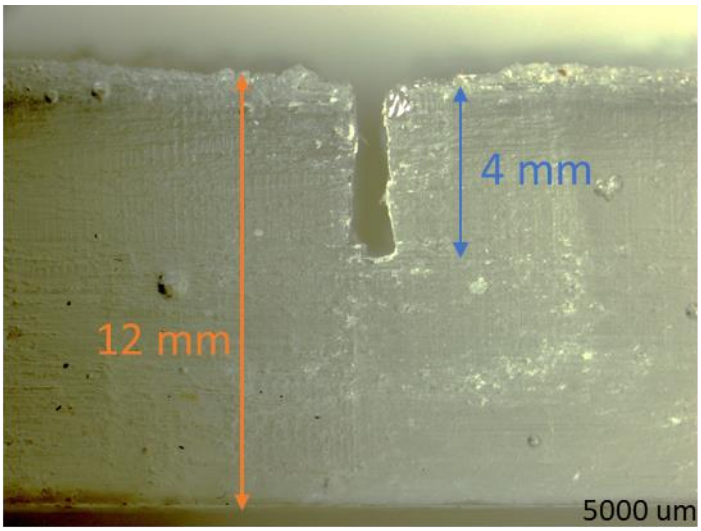

Fig. 2. Illustration of cut TPU/ER sample by the blade

2.3. Characterization of composites

For the healing test, samples of the composite were cut to a depth of 4 mm by using a razor blade in a frozen state to avoid any accidental deformation of the samples, as shown in Fig. 2. Care was taken to ensure that healing of the scratched or cut samples occurs mainly by heating. The temperature of healing was 150 °C by the oven (memmert–UNB40 made in Germany) for 80 min. After that, all the samples were extracted from the oven and froze at room temperature (20–25 °C) for 5 hours. The healed specimens were subjected to the mechanical test. The self-healing efficiencies were obtained on the recovery of tensile strength following Eq. (1),

$$\text{Healing of Efficiency (\%)} = \frac{Tensile\ Strength_{healed}}{Tensile\ Strength_{virginal}} \times 100 \quad (1)$$

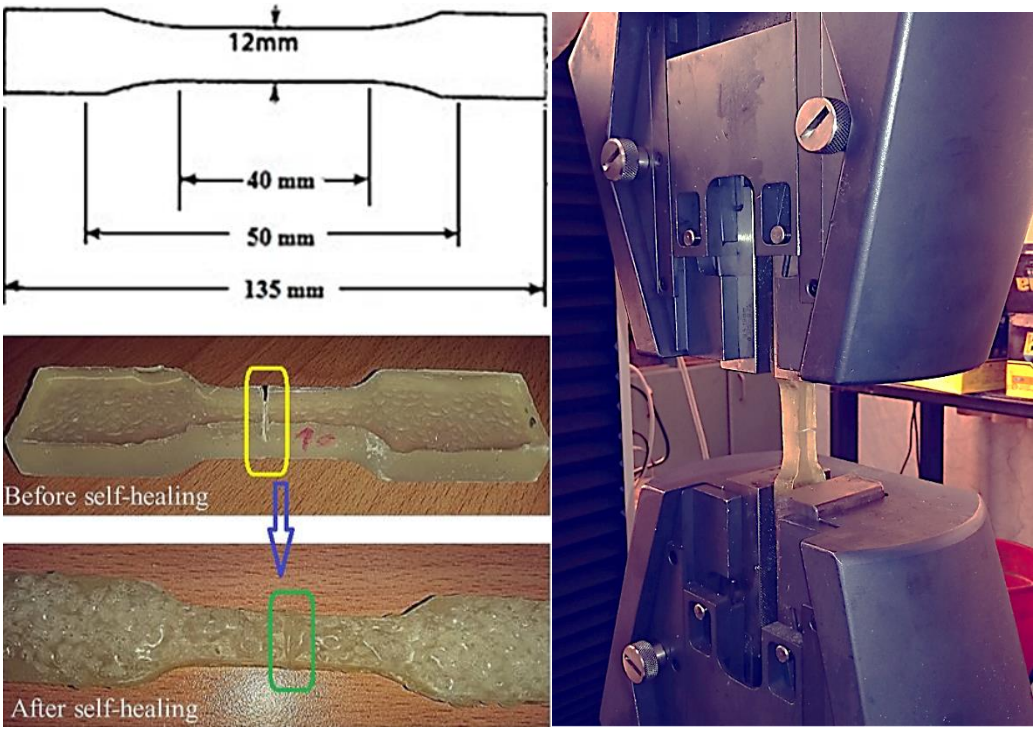

Fig. 3. Samples before and after self-healing, and their placement under tensile testing

Where tensile strength healed and tensile strength virginal are obtained in tensile test of healed and virgin materials for a given concentration of healing. The stress-strain relation, including tensile modulus of TPU/ER composites, is determined as a function of TPU content according to ASTM D3039/D3039M-17using an Instron-4486 made from Britain apparatus, as shown in Fig.3. A 2500 N load cell and an extensometer with a gauge length of 10 mm are used. A displacement control with a speed of 2.00 mm/s is applied. The tensile properties are measured for TPU/ER composites with 0, 10, 20, and 30 wt.% of TPUs.

The flexural test for self-healing is shown on the universal testing machine for three-point bending, as shown in Fig. 4. The equipped specimen is placed on rollers provided at the extreme ends. The specimen diameters are carried out according in proportion to the width of the specimen as specified by ASTM D790 on an MTS 810 Material Test System (MTS Systems Corp., Eden Prairie, MN) at a crosshead velocity of 2.00mm/min and a span of 50 mm. The load and deflection are shown on a computer. These samples are loaded until the first visual appearance of the crack.

The fracture behavior of the material at high strain rate levels was investigated by testing surfaces obtained after Charpy impact tests were performed according to ASTM D6110 standard, with digital pendulum impact indicator provided by SIT-50, the series of Santam Company, as shown in Fig. 5.

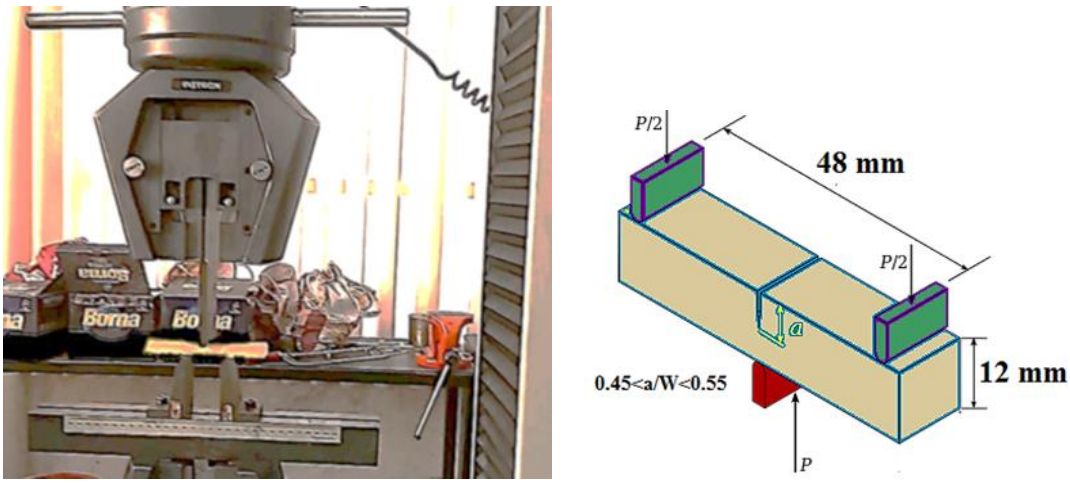

Fig. 4. Flexural test for self-healing and sample dimensional.

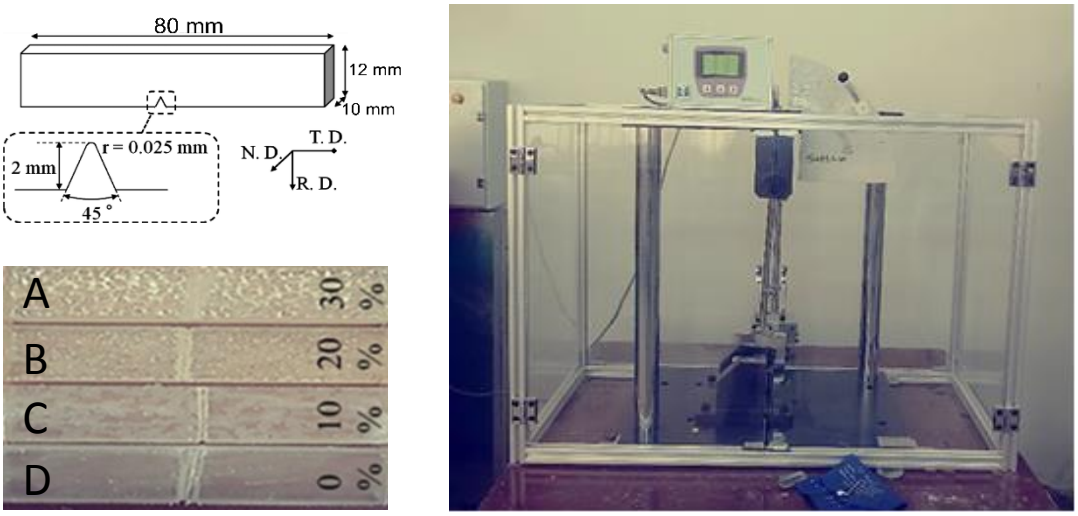

Fig. 5. Samples of Impact Test and Charpy impact test machine

The rectangular dimensions of the Charpy impact specimens with different TPU contents were 80 × 12 × 10 mm^3, as shown in Fig. 5. The speed of the impact test was 2.9 m/s with an incident energy of 5 J at room temperature and regular atmospheric conditions The XRD studies on the sample were carried out on an X-Ray Diffractometer, Phillips, Germany instrument. Fig. 6 represents the XRDs of the amorphous structure in the sample and that shows there is no crystal structure in it.

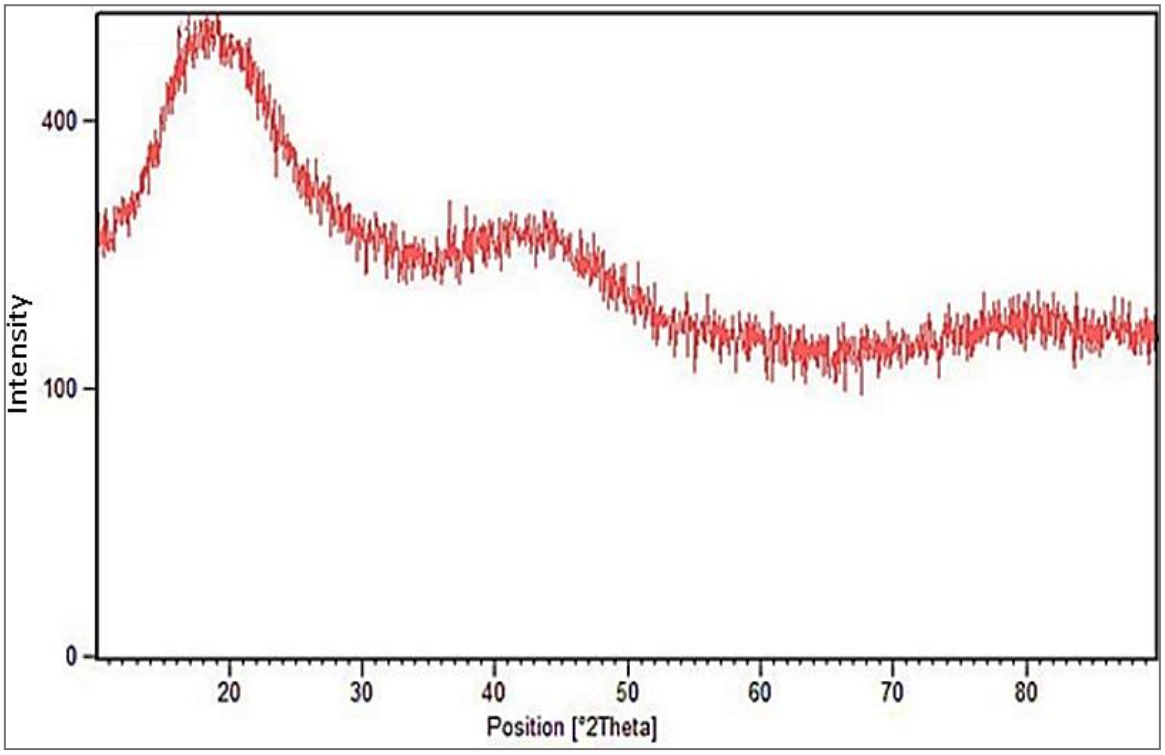

Fig. 6. XRD of TPU/ER

3. Results and discussion

3.1. Self-healing properties

The self-healing behavior of TPU/ER composites under thermal treatment was first investigated by observing the improvement of the cracks with the contents of different TPU granules. The healing test was conducted by heating the cut specimens to 150°C for 80 min while no external force was applied. Figs. 7-10 show the results of the surface analysis conducted by stereoscope (Olympus SZX16) before and after the healing process; then, qualitative observations were performed using image processing software. According to Figs. 7-10, with the removal of external force, gaps were sealed for all samples, and only trace lines were observed, indicating that the influence of introducing TPU on the self-healing of epoxy resin has been successful. Figs. 7-10 shows the evolution process of cracks in TPU/ER samples from various TPU values during heat treatment at 150°C.

It can be seen that the widths of all cracks are reduced with the extension of heat treatment time Fig. 7 shows that all TPU/ER samples except for Sample A have self-healing properties. The reason for this is that sample A was not used with TPU granules, as shown in Fig. 7. However, the crack in TPU/ER sample from Sample B does not disappear completely; rather, it only becomes part of the restored cracks, manifesting that the self-healing process has not finished, as illustrated in Fig. 8. The reason is that in Sample B, a little bit of granule has been used in comparison to the other two samples. By contrast, the healing degree is different for three specimens at the same heat treatment time. Cracks in TPU/ER samples from Sample C and Sample D completely disappeared when the percentage of the granules increased, as shown in Fig. 9 and Fig. 10. However, in the Sample C and Sample D specimens, recovery of a gap was better than that in Sample B and Sample A specimens. Although the cuts were closed, further tests were employed to evaluate the recovery of mechanical properties, which was mainly due to the different contents of polyurethane.

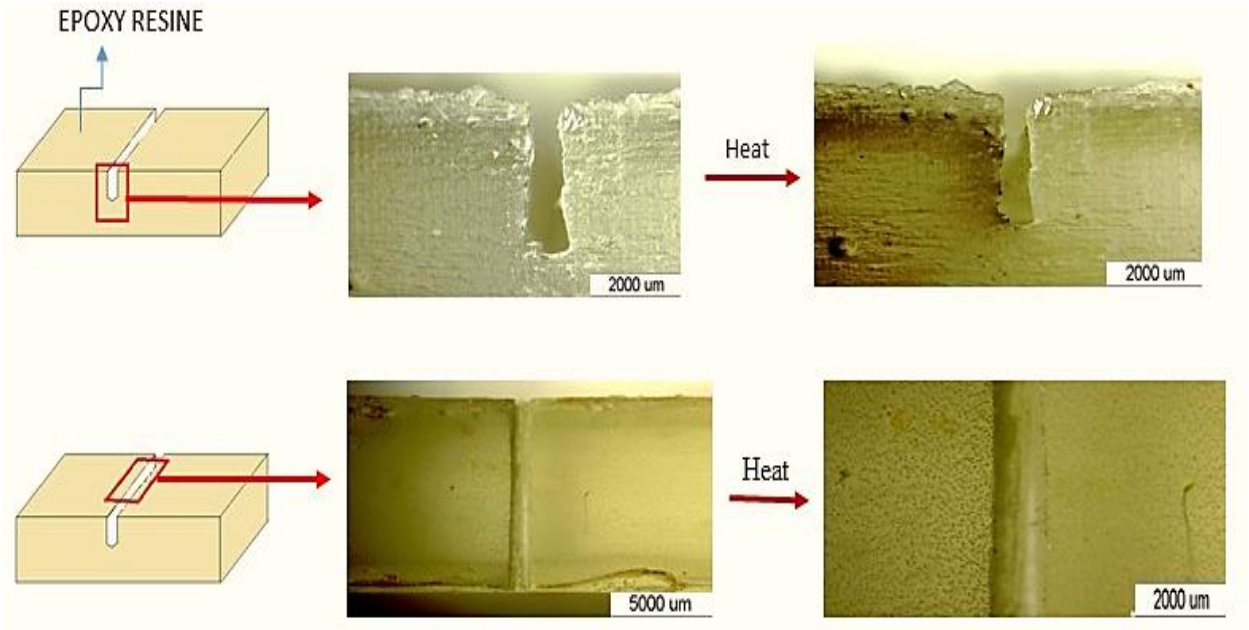

Fig. 7. Sample A shows no self-healing after a certain temperature and heating.

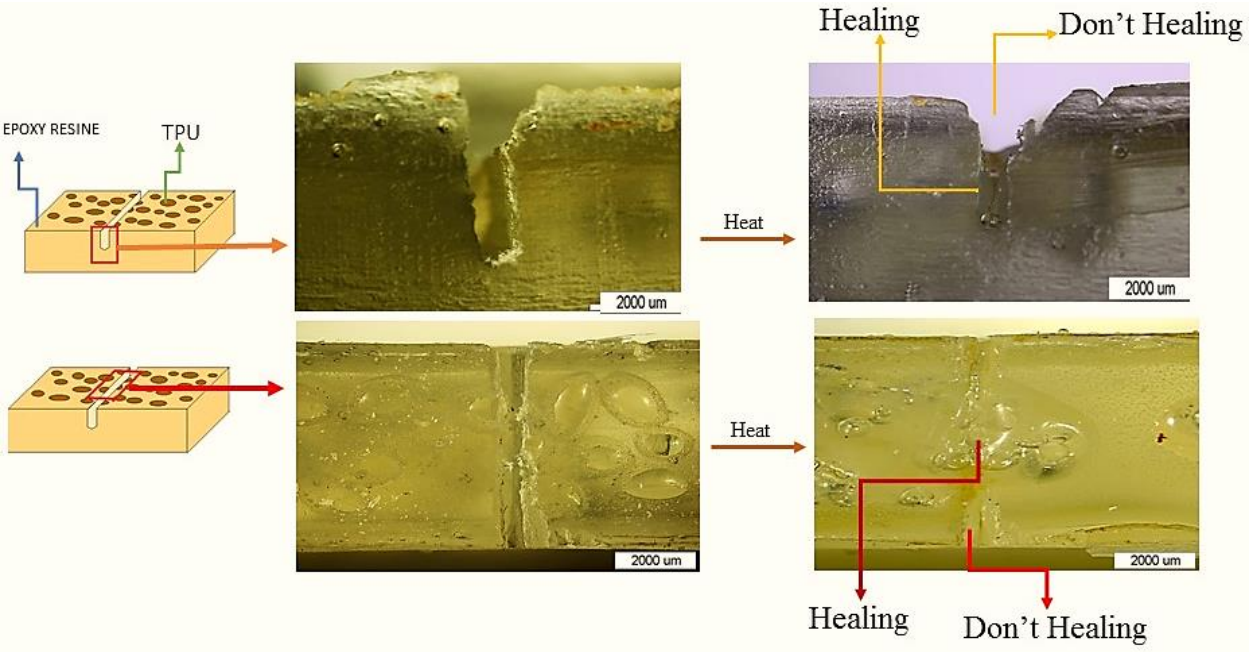

Fig. 8. Sample B shows healing after heating for a certain time, but healing is not complete

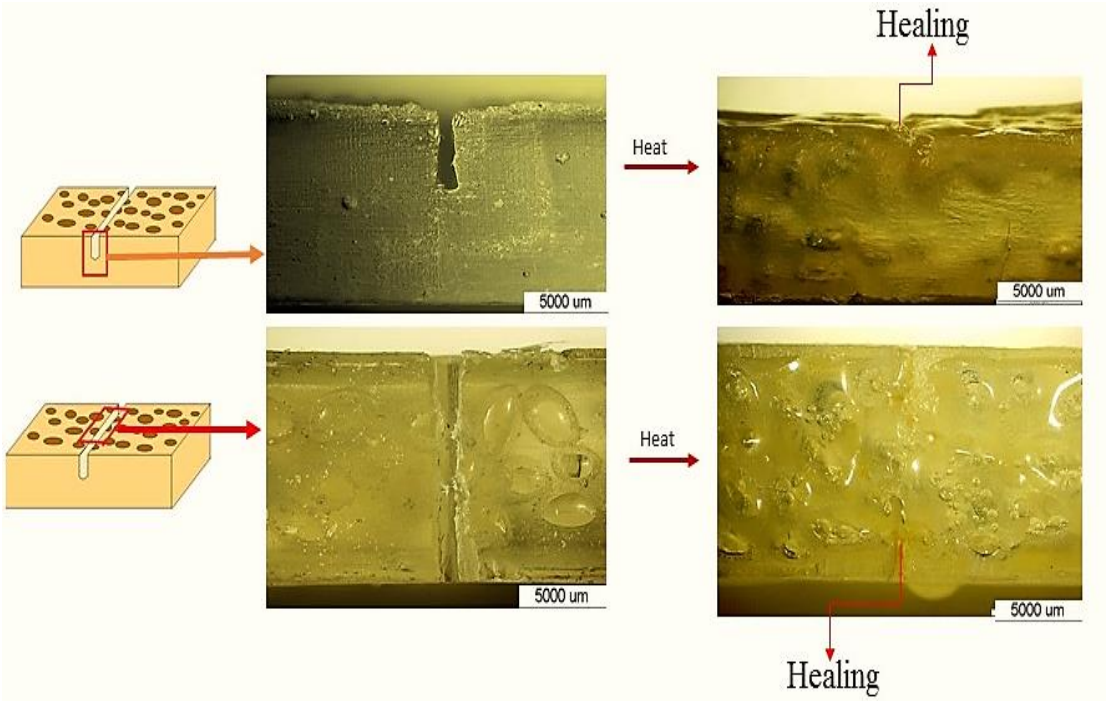

Fig. 9. Sample C illustrated that TPU was melted and self-healing after heating at a certain time was completed.

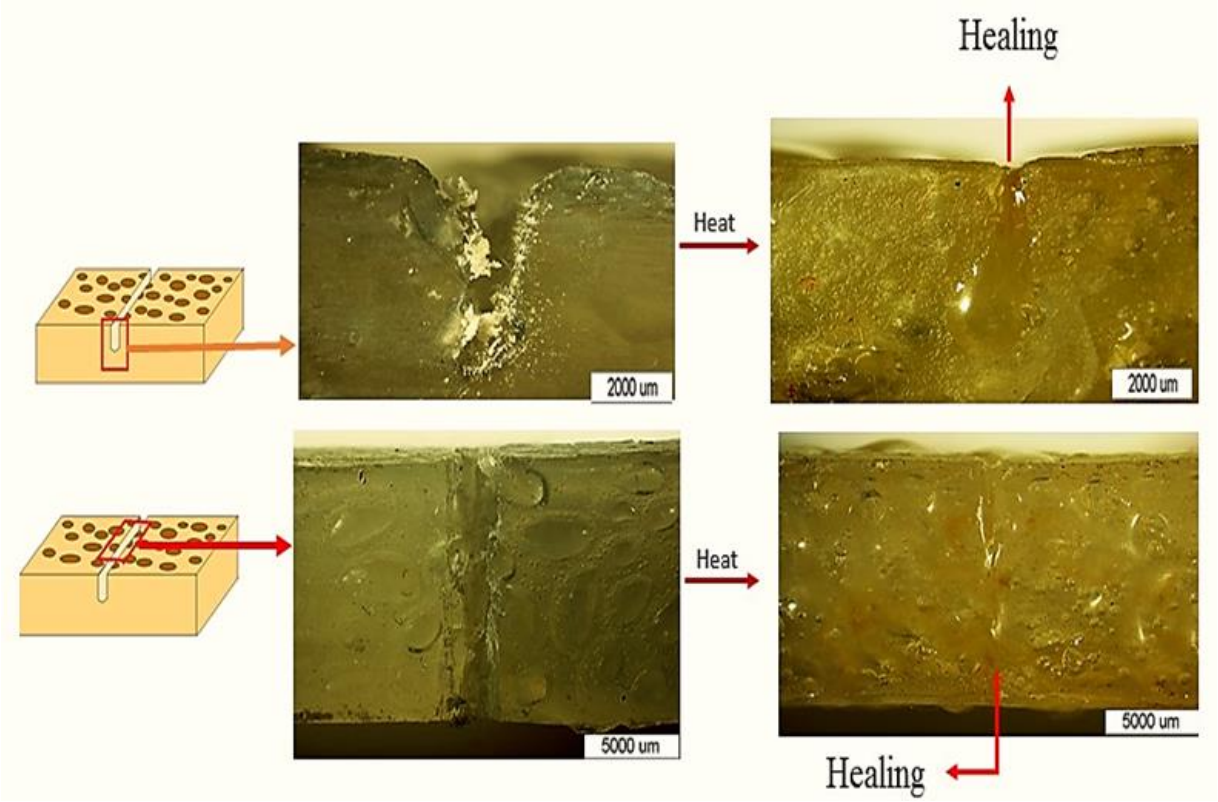

Fig. 10. Sample D shows that this sample like sample C was self-healed completely after heating in the same time (80 min, in150°C)

3.2. Flexural properties

The flexural properties of different self-healing groups (Sample A, Sample B, Sample C, and Sample D) are shown in Fig. 11. These data show that both the modulus and the strength of composites decrease with an increase in TPU content. The reason is that epoxy resin, used as a matrix in polymer composite specimens, has a brittle property. Furthermore, composite specimens have become more fragile by adding TPU granules to the epoxy resin matrix. Therefore, it should select the most suitable percentage of TPU granular composition by tensile test and impact test to obtain the highest mechanical properties.

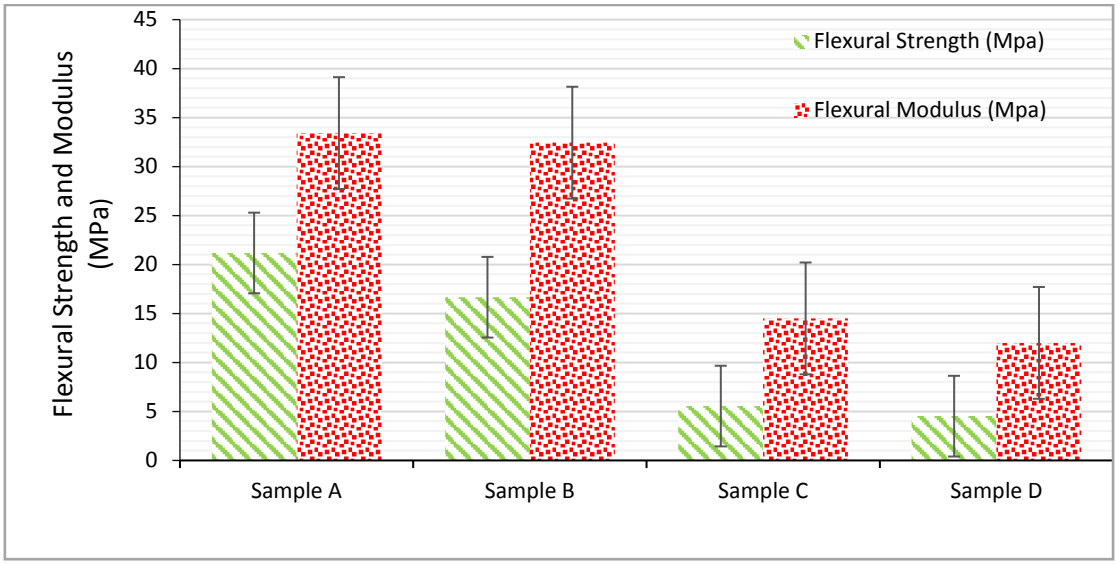

Fig. 11. Effect of processing on the flexural properties of TPU/ER composites

3.3. Healing efficiency properties

In this study, the stress at the first inflection point was used to calculate the healing efficiency of the epoxy resin. The experimental results for obtaining the ultimate tensile strengths of the healed specimens are illustrated in Fig. 12.

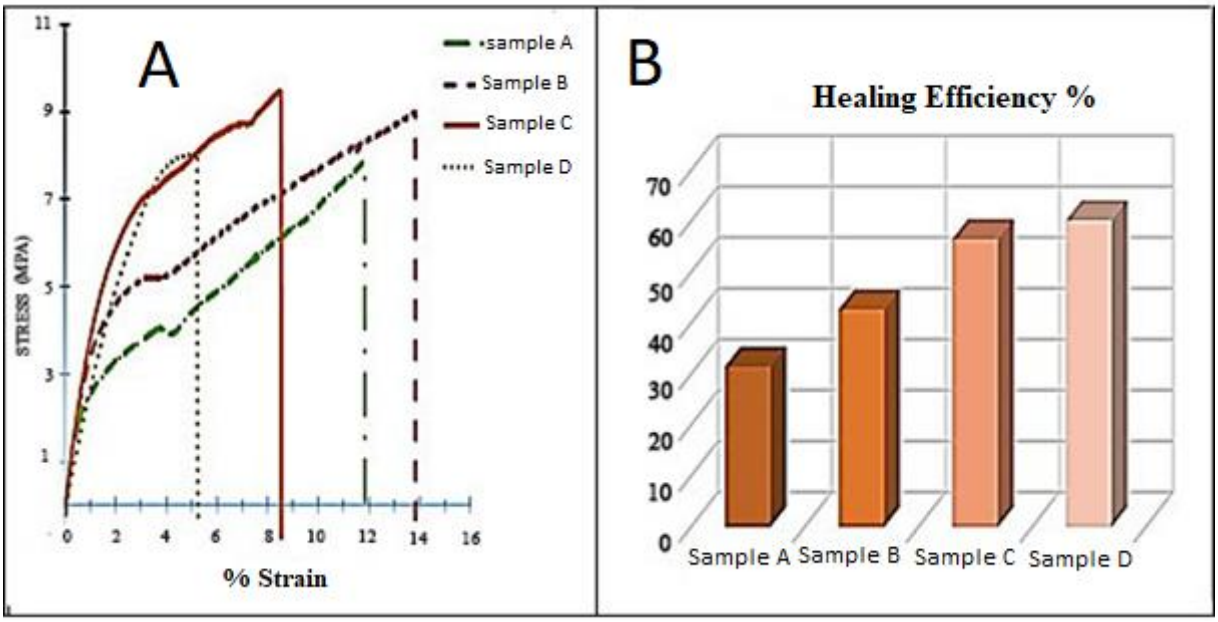

Fig. 12. A: Tensile strength of different TPU/ER structurally reinforced TPU composites of the healing specimens
B: The self-healing efficiencies were obtained on the recovery of tensile strength Eq. (1)

The experimental healing parameters for the four kinds of samples are listed in Table 1. As shown in Table 1, there is a clear difference in the ultimate tensile strength among the healed samples with variable healing conditions. By comparing Sample C and Sample A, and Sample B, we can see the higher ultimate tensile strength and Young's modulus. When comparing Sample C and Sample D, we can conclude that Sample C has the higher tensile strength, elongation at break, and Young's modulus. Moreover, the self-healing efficiency of the three samples is also different. Sample A exhibits quite a low healing efficiency of 31.6% because there are no TPU granules for sample repair. In contrast, Sample B from a lower TPU value exhibits excellent mobility because of the lower content of hard segments, which reduces the tensile strength and lead to sample shape deformation upon heat treatment. Thus, a relatively low healing efficiency of 42.7% is obtained. It is worth noting that a much higher self-healing efficiency than 56.5% and 60.2% is obtained for Sample C and Sample D. However, after the healing process, Sample C has a higher Young's modulus, tensile strength, and healing efficiency. Compared to other specimens, it indicates that a suitable TPU value has been selected for Sample C.

Table 1. Experimental Parameters for Four Specimens of Self-Healing Experiments

Sample	Healing Temperature (°C)	Healing Time (Min)	Ultimate Tensile strength (MPa)	Elongation at break (%)	Young's Modulus (MPa)	Healing Efficiency (%)
Sample A	150	80	7.84422	11.83687	3.948	31.5
Sample B	150	80	8.99474	13.83687	4.165	42.7
Sample C	150	80	9.465389	8.529687	4.837	56.5
Sample D	150	80	8.007692	5.22375	2.784	60.2

3.4. Tensile properties

The stress-strain relation for TPU/ER composites, obtained by tensile testing, as a function of the TPU content, is shown in Fig. 13. This figure represents stress-strain curves of virginal (as-prepared), cut (with a crack of 4 mm in depth), and healed (heat-treated at 150°C for 80 min) TPU/ER samples from different TPU values. Tensile test data and Young's Modulus of TPU/ER from different TPU values are listed in Table 2. It can be found from Fig. 13 and Table 2 that the tensile strength, elongation at break, and Young's modulus of each cut TPU/ER sample with a crack, will decrease as compared to those of the virginal specimen. On the contrary, the tensile strength and elongation at break of each healing TPU/ER sample with healing increase compared to those of cut specimen Young's modulus healing of Sample A and Sample D decrease compared to cut TPU/ER samples. However, all three mechanical properties of each healed TPU/ER samples are lower than those of virginal ones, indicating that all TPU/ER samples exhibit certain self-healing performances while cracks cannot be repaired completely.

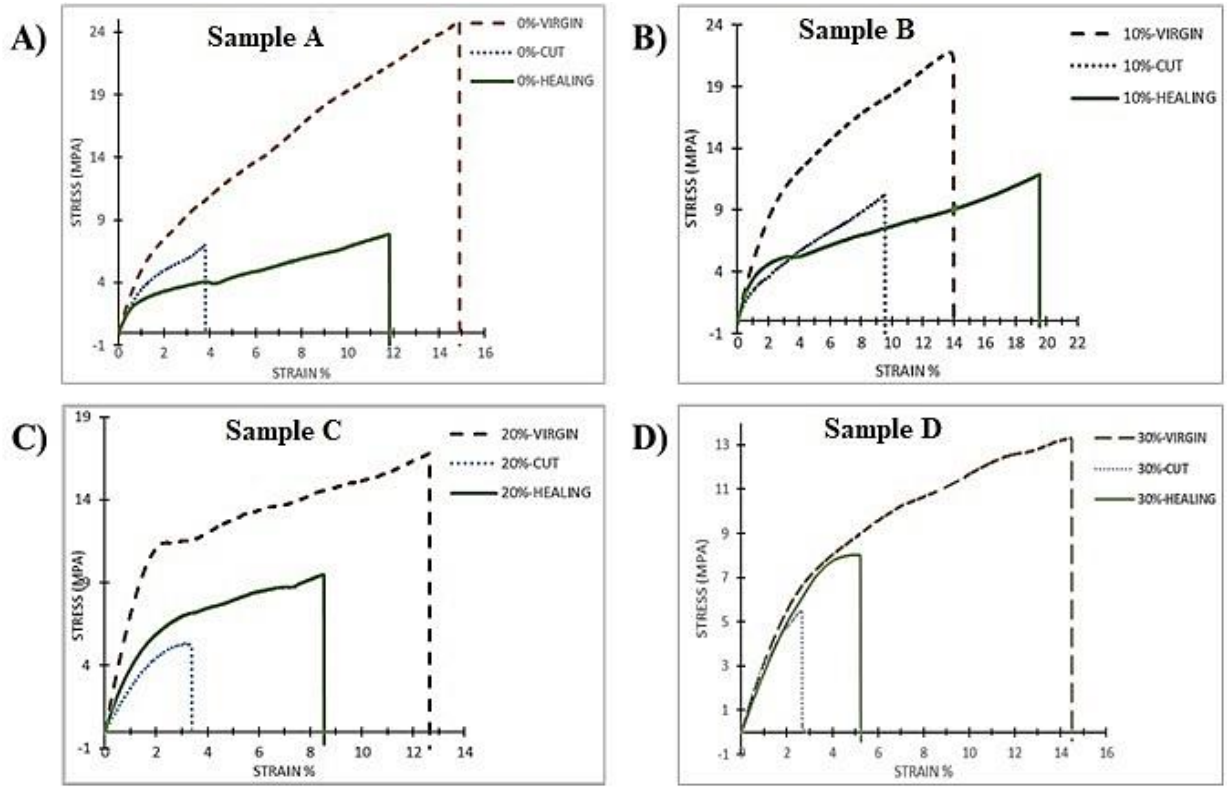

Fig. 13. Representative stress-strain curves of TPUER composites as a function of different TPU contents. A= stress-strain curves Sample A (with out TPU granules in epoxy resin), B = stress-strain curves Sample B (ER+10 Wt.% TPU granules), C= stress-strain curves Sample C (ER+20 Wt.%TPU granules), D= stress-strain curves Sample D (ER+30 Wt.% TPU granules)

Moreover, a comparison of mechanical properties of TPU/ER samples from different TPU values indicates that the tensile strength and Young's modulus of Sample B and Sample C are better than the other two samples in healing.

Table 2. Tensile test data and Young's Modulus of TPU/ER from different TPU values.

Sample from different TPU values	Condition	Tensile strength(MPa)	Elongation at break (%)	Young's Modulus (MPa)
	Virgin	24.89247	14.89375	5.583
TPU/ER (Sample A)	Cut	7.007532	3.805312	4.054
	Healing	7.84422	11.83687	3.948
	Virgin	21.0226	13.97219	5.693
TPU/ER (Sample B)	Cut	10.19753	9.544375	3.554
	Healing	8.99474	13.83687	4.165
	Virgin	16.78831	12.63875	7.311
TPU/ER (Sample C)	Cut	5.229481	3.377812	2.758
	Healing	9.465389	8.529687	4.837
	Virgin	13.28292	14.4875	3.373
TPU/ER (Sample D)	Cut	5.504717	2.66475	3.135
	Healing	8.007692	5.22375	2.784

3.5. Impact test

The experimental results concerning the impact properties of the tested samples for four self-healing TPU/ER samples are presented in Fig. 14. The Charpy impact test was carried out to evaluate the impact energy of the healing TPU/ER composites. The obtained results revealed that Sample C has higher impact energy than the other sample because not only is Sample C completely self-healing, but also the TPU content is appropriate in the Epoxy resin.

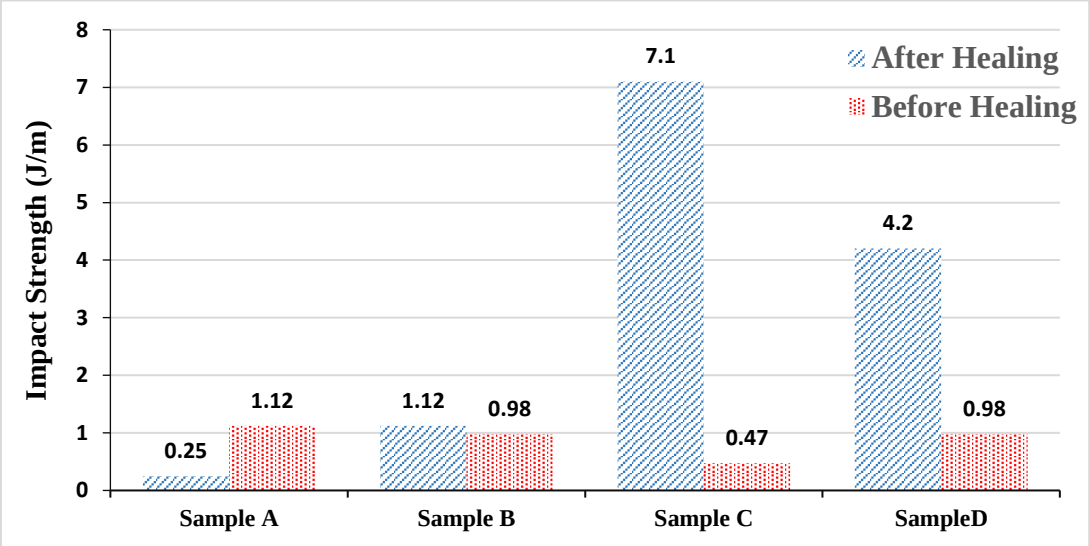

Fig. 14. Representative impact test of TPU/ER composites

4. Conclusions

The study of self-healing is of great significance for epoxy polymers. Epoxy polymers are applied in all aspects of life, including aerospace, automotive, and electronic fields. Epoxy polymers are also widely used in construction and transportation fields, such as, building materials and epoxy asphalt [34].

In the present paper, a series of self-healing TPU/ER composites were prepared. TPU/ER composites with a certain amount of TPU were successfully able to heal cracks automatically and improve structural function via a granule embedded in the matrix. Mechanical tests show the incorporation of an appropriate content of TPU in the matrix to reinforce and recover the mechanical properties of these samples after damage. Results of the tensile test and impact test revealed that incorporating 20Wt.% of TPU in Sample C would promote mechanical

properties in comparison with other samples. In the before research has shown to be capable of recovering between 50% and 70% of its pre-fracture strength after healing [35]. Stereoscope observation shows that cracks with 4 mm in depth in TPU/ER samples can be healed upon heat treatment of 150°C for 80 min, while the self-healing efficiency can reach as high as 60%. They further confirm that the excellent self-healing performance of TPU/ER is due to the combined actions of thermo-reversible TPU reaction and thermal movement of molecular chains. Consequently, our present understanding shows that the TPU bond and its thermal reversibility contribute much to the improvement of the mechanical property while the thermal movement efficacy of molecular chains acts as an auxiliary recovering force that speeds up the whole healing process.

References

[1] Li G and Zhang P 2013 A self-healing particulate composite reinforced with strain hardened short shape memory polymer fibers, Polymer, 54, 5075-5086.
[2] Altuna F I, Antonacci J, Arenas G F, Pettarin V, Hoppe C E, and Williams R J J 2016 Photothermal triggering of self-healing processes applied to the reparation of bio-based polymer networks, Mater. Res. Express, 3, 045003.
[3] Zainuddin S, Arefin T, Fahim A, Hosur M, Tyson J, Kumar A, Trovillion J, and Jeelani S 2014 Recovery and improvement in low-velocity impact properties of e-glass/epoxy composites through novel self-healing technique, Compos. Struct. 108, 277-286.
[4] Latif S, Amin S, Haroon S S, and Sajjad I A 2019 Self-healing materials for electronic applications: an overview, Mater. Res. Express, 6, 062001.
[5] Keller M W and Crall M D, 2018, 6.15 Self-Healing Composite Materials Comprehensive Composite, Materials II 6 431-453.
[6] Thakur V K and Kessler M R, 2015, Self-healing polymer nanocomposite materials: A review, Polymer, 69, 369-383.
[7] Das R, Melchior C, and Karumbaiah K, 2016, Self-healing composites for aerospace applications, In Advanced composite materials for aerospace engineering, 333-364.
[8] Zhang P and Li G, 2015, Healing-on-demand composites based on polymer artificial muscle, Polymer 64, 29-38.
[9] Pramanik N B, Nando G B, and Singha N K, 2015, Self-healing polymeric gel via RAFT polymerization and Diels–Alder click chemistry, Polymer, 69, 349-356.
[10] Yao L, Yuan Y C, Rong M Z, and Zhang M Q, 2011, Self-healing linear polymers based on RAFT polymerization, Polymer, 52, 3137-3145.
[11] Michael P, Doehler D, and Binder W H, 2015, Improving autonomous self-healing via combined chemical/physical principles, Polymer, 69, 216-227.
[12] Zhang G, Pei J, Li R, Li P, and Zhou B J, 2018, The preparation and characterization of a novel self-healing based on the dynamic translocation of disulfide bonds, Mater. Res. Express 5, 105301.
[13] Jones A and Dutta H, 2010, Fatigue life modeling of self-healing polymer systems, Mech. Mater. 42, 481-490.
[14] Jones A, Watkins C, White S, and Sottos N, 2015, Self-healing thermoplastic-toughened epoxy, Polymer, 74, 254-261.
[15] Ollier R P, Penoff M E, and Alvarez V A, 2016, Microencapsulation of epoxy resins: Optimization of synthesis conditions, Colloids. Surf. A Physicochem. Eng. Asp. 511, 27-38.
[16] Raimondo M, Guadagno L, Naddeo C, Longo P, Mariconda A, and Agovino A 2017 New structure of diamine curing agent for epoxy resins with self-restoration ability: Synthesis and spectroscopy characterization, J. Mol. Struct. 1130, 400-407.
[17] Meure S, Wu D-Y, and Furman S A, 2010, FTIR study of bonding between a thermoplastic healing agent and a mendable epoxy resin, Vib. Spectrosc. 52, 10-15.
[18] Pingkarawat K, Dell'Olio C, Varley R, and Mouritz A, 2016, Poly (ethylene-co-methacrylic acid) (EMAA) as an efficient healing agent for high performance epoxy networks using diglycidyl ether of bisphenol A (DGEBA), Polymer 92, 153-163.
[19] Pingkarawat K, Bhat T, Craze D, Wang C, Varley R J, and Mouritz A, 2013, Healing of carbon fibre–epoxy composites using thermoplastic additives, Polym. Chem. 4 5007-5015.
[20] Tripathi M, Kumar D, and Roy P K, 2017, Mesoporous silica as amine immobiliser for endowing healing functionality to epoxy resin Compos. Commun. 4, 20-23.
[21] Ling J, Rong M Z, and Zhang M Q, 2012, Photo-stimulated self-healing polyurethane containing dihydroxyl coumarin derivatives, Polymer 53, 2691-2698.
[22] Abdoluosefi H E and Honarasa G, 2017, Fabrication of polyurethane and thermoplastic polyurethane nanofiber by controlling the electrospinning parameters, Mater. Res. Express 4, 105308.
[23] Yuan C e, Rong M Z, and Zhang M Q, 2014, Self-healing polyurethane elastomer with thermally reversible alkoxyamines as crosslinkages, Polymer 55, 1782-1791.
[24] Feng L, Yu Z, Bian Y, Lu J, Shi X, and Chai C, 2017, Self-healing behavior of polyurethanes based on dual actions of thermo-reversible Diels-Alder reaction and thermal movement of molecular chains, Polymer, 124, 48-59.

[25] Xu Y and Chen D, 2017, Self-healing polyurethane/attapulgite nanocomposites based on disulfide bonds and shape memory effect, Mater. Chem. Phys. 195, 40-48.
[26] Bera M and Maji P K, 2017, Effect of structural disparity of graphene-based materials on thermo-mechanical and surface properties of thermoplastic polyurethane nanocomposites, Polymer, 119, 118-133.
[27] Mishra A K, Chattopadhyay S, Rajamohanan P, and Nando G B 2011 Effect of tethering on the structure-property relationship of TPU-dual modified Laponite clay nanocomposites prepared by ex-situ and in-situ techniques, Polymer, 52, 1071-1083.
[28] Li H, Ning N, Zhang L, Wang Y, Liang W, Tian M, and Chan T W 2015 Effect of content of organophosphorus on flame retardancy mode of thermoplastic polyurethane, Polymer, 67, 1-11.
[29] Pedrazzoli D and Manas-Zloczower I 2016 Understanding phase separation and morphology in thermoplastic polyurethanes nanocomposites, Polymer, 90, 256-263.
[30] Choi J, Jang J U, Yin W B, Lee B, and Lee K J, 2017, Synthesis of highly functionalized thermoplastic polyurethanes and their potential applications, Polymer, 116, 287-294.
[31] Liu R-C, Liu K, Du Y, Xu X-W, and Jia R-P, 2019, Microphase separation and properties of TPU/Nd2O3 nanocomposites, Materials Research Express 6, 055321.
[32] Li Y, Gao F, Xue Z, Luan Y, Yan X, Guo Z, and Wang Z, 2018, Synergistic effect of different graphene-CNT heterostructures on mechanical and self-healing properties of thermoplastic polyurethane composites, Mater. Des. 137, 438-445.
[33] Kim S M, Jeon H, Shin S H, Park S A, Jegal J, Hwang S Y, Oh D X, and Park J, 2018, Superior Toughness and Fast Self-Healing at Room Temperature Engineered by Transparent Elastomers, Adv. Mater. 30, 1705145.
[34] Fenglei Zhang, Lei Zhang, Muhammad Yaseen and Kai Huang, 2020, A review on the self-healing ability of epoxy polymers, J. Appl. Polym. Sci.
[35] Hayes S A, Jones F R, Marshiya K, Zhang W, 2007, A self-healing thermosetting composite material Composites Part A: Applied Science and Manufacturing. 38, 1116-1120